University of Glasgow

Bassiri, Riccardo (2011) *The atomic structure and properties of mirror coatings for use in gravitational wave detectors.* PhD thesis.

http://theses.gla.ac.uk/2701/

The Atomic Structure and Properties of Mirror Coatings for use in Gravitational Wave Detectors

VIA VERITAS VITA

Riccardo Bassiri

School of Physics and Astronomy

College of Science and Engineering

University of Glasgow

Presented as a Thesis for The Degree of

Doctor of Philosophy

Supervised by Dr. Ian MacLaren and Prof. Sheila Rowan

June 2011

Contents

List of Figures

List of Tables

Acknowledgements

It has been a honour and privilege to work with truly inspirational, supportive and talented people during my Ph.D. studies and this thesis is a testament to them.

Firstly, I would like to offer my most sincere gratitude to my supervisors, Dr. Ian MacLaren and Prof. Sheila Rowan, for their extensive help and guidance over the course of my Ph.D. studies. Their leadership, time and energy and provision of countless opportunities, ensured that my research was at its best. I would like to thank Prof. Jim Hough for being a great source of enthusiasm and inspiration for all my research activities. I would also like to thank Prof. Alan Craven for his advice throughout the course of my studies. Thanks also to the EPSRC funding council for providing my doctoral training grant, which enabled me to carry out the research presented in this thesis.

I am very grateful to the late Prof. David Cockayne and his research team, Konstantin Borisenko, Yixin Chen and Guoqiang Lee at the University of Oxford for allowing me to learn their processes of studying amorphous materials and collaborate with them.

I would like to thank Iain Martin for the time he has spent working with me, our many discussions were a great help, and resulted in many of the ideas for the coatings research presented in this thesis. A particular thank you to Ronny Nawrodt, for teaching me a great deal in the lab and being a pleasure to work with. A special thank you to Keith Evans for his help analysing data, generating atomic models, and for the many spirited conversations about our research. I would also like to thank Alan Cumming, Paolo Longo, Peter

Murray, Stuart Reid and Mariëlle Van Veggel for their help and support with various aspects of my research.

My research could not have been successfully carried out, without the pleasure of working with many technicians. I therefore wish to sincerely thank Sam McFadzean and Colin How for their help and support in the Transmission Electron Microscope (TEM); Jamie Scott for helping me out with my initial TEM work and solving the numerous IT issues since; Colin Craig, Stephen Craig and Steven O'Shea for helping solve a multitude of technical issues in the mechanical loss labs. I am very grateful to Brian Miller for helping produce most of the TEM samples studied, and our interesting conversations. Also, a special thanks to Jean Greig who organised all my travel and put up with my many random queries.

Thanks to current and previous office and research mates Matt Abernathy, Mohammed Basith, Eleonora Bellini, Nicola Beveridge, Chris Bell, Paul Campsie, Eleanor Chalkley, Michael Finnie, Alastair Heptonstall, Duc Quang Hoang, Rahul Kumar, Kerry O'Shea, Rumyana Petrova and Liqiu Wang for making my Ph.D. a very enjoyable experience. I would especially like to thank Karen Haughian for her friendship and support, countless laughs and generally putting up with my quirky ways. Thanks also to Matt Edgar for the exchange of many great ideas and for our continuing entrepreneurial ventures. I would also like to thank all the members of the Institute for Gravitational Research and Solid State Physics Group for providing an enjoyable and supportive place to work.

On a more personal note, I would like to thank my parents and my sister for their unconditional love and support and for giving me a great life full of opportunity. Finally, I would like to thank my extended family and friends for enriching my life with their love.

Preface

This thesis is an account of the research carried out in the Institute for Gravitational Research and Solid State Physics Group at the University of Glasgow between October 2007 and May 2011, which involved the study of the atomic structure and properties of mirror coatings for use in gravitational wave detectors.

In Chapter 1 the nature and origin of gravitational waves is discussed along with techniques for their detection and the status of current and future gravitational wave detectors.

In Chapter 2 the current understanding of thermal noise from the optical coatings in gravitational wave detectors is discussed. Then the experimental techniques which are used in this thesis to study the material properties of the mirror coatings, including the theory behind transmission electron microscopy, are described in detail.

In Chapter 3 an investigation into the effect of heat-treatment on Ta_2O_5 mirror coatings is presented. For the $400\,°C$ heat-treated coating, the work involving the process of calculating the Reduced Density Function (RDF) was carried out in collaboration with Prof. D. J. H. Cockayne and Dr. K. B. Borisenko at the University of Oxford. Data collection on the Transmission Electron Microscope (TEM) was carried out by the author in Glasgow and analysis was carried out in collaboration with Prof. D. J. H. Cockayne and Dr. K. B. Borisenko. The remaining $300\,°C$ and $600\,°C$ heat-treated coatings were analysed by the author in collaboration with Mr. K. Evans. The cryogenic loss measurements for the ATF low water content Ta_2O_5 coatings was carried

out by the author in collaboration with Dr. I. W. Martin. The author also computed and analysed RDF measurements for the low water content coatings in collaboration with Mr. K. Evans. RDF measurements and analysis for the MLD Ta_2O_5 coatings was carried out by the author in collaboration Mr. K. Evans. At all stages, the analysis was carried out with input from Dr. I. MacLaren and Prof. S. Rowan.

In Chapter 4 an investigation into the effects of TiO_2 doping the Ta_2O_5 coatings as a way of reducing the mechanical loss is presented. These measurements were carried out at the suggestion of Dr. I. MacLaren and Prof. S. Rowan. The TEM diffraction data required for the RDFs was collected by the author and analysed in collaboration with Mr. K. Evans. The atomic models where created by the author in collaboration with Mr. K. Evans and analysed by the author.

In Chapter 5 studies into the material properties of HfO_2 and SiO_2 coatings are presented. These measurements were carried out following discussions between the author, Dr. I. MacLaren and Prof. S. Rowan. The room temperature mechanical loss measurements were carried out by the author in collaboration with Dr. R. Nawrodt. The results were analysed by the author in collaboration with Dr. P. Murray. The TEM diffraction data required for the RDFs was collected by the author and analysed in collaborating with Mr. K. Evans.

Summary

The Atomic Structure and Properties of Mirror Coatings for use in Gravitational Wave Detectors

Gravitational waves are a prediction of Einstein's General Theory of Relativity. They can be regarded as perturbations, or ripples, in the curvature of space-time that travel at the speed of light. Detectable gravitational waves are the result of the asymmetric acceleration of mass that occurs during massive astronomical events, such as coalescing compact binary systems and supernovae. The nature and detection of gravitational waves is the focus of Chapter 1.

A direct detection of gravitational waves is still to be made, however, there is strong indirect evidence of their existence through the work Hulse and Taylor. They observed a binary pulsar system over a number of years and found it to have a decaying orbit that followed a decay rate consistent with a model in which energy is lost due to the production of gravitational waves.

The most promising method for gravitational wave detection is through the use of long-baseline interferometric gravitational wave detectors, such as LIGO located in the US, GEO 600 in Germany and Virgo in Italy. There are planned upgrades to current long-baseline interferometric gravitational wave detectors. These second generation of detectors will aim to improve sensitivity by a factor of around ten, allowing a much greater chance of detecting gravitational waves, particularly from sources such as coalescing compact binary systems. However, the sensitivity of these detectors will still be limited by noise sources, such as photon-shot, seismic and thermal noise, which could be further reduced by the development of new technologies.

Chapter 2 discusses the current understanding of thermal noise arising from the mirror coatings in the detector test-masses. This will identify thermal noise as a particularly important noise source, limiting the sensitivity of detectors between the frequency range from a few tens Hertz to several hundred Hertz.

There is an international network of scientists working on developing new technologies for future generations of interferometric gravitational wave detectors, which have the aim of increasing detector sensitivity and further reducing the effect of detector noise sources. The research presented in this thesis focuses on investigating the mechanical loss, which is directly related to the thermal noise, of the mirror coatings. In particular the first attempts at correlating changes in atomic structure of the coatings to the mechanical loss where various properties, such as heat-treatment and doping, of the coatings have been systematically changed will be presented.

Chapter 3 will focus on the effect of heat-treatment of pure Ta_2O_5 coatings. The process of heat treating Ta_2O_5 coatings has observable effects on mechanical loss measured at low temperature, where loss peaks arise in the region of 10s of K and develop as the heat-treatment temperature rises. Heat-treatment also produces subtle changes to the averaged local atomic structure of the coatings where it can be seen that as the heat-treatment temperature is increased, the coatings became more ordered, moving towards crystallisation between heat-treatment at 300-600 °C coatings before fully crystallising at 800 °C. Atomic models show Ta_2O_2 ring fragments which are present in the crystalline phases of similar materials. In general it is observed that as heat-treatment temperature is increased there is an increase in the presence of the Ta_2O_2 ring fragments and a decrease in the presence of Ta-Ta bonds in the atomic structures. Changing the manufacturing deposition process for the Ta_2O_5 coatings also creates significant changes in the mechanical loss at low temperatures, where a 'low water content' manufacturing processes gives rise to changes in the positions and shapes of the low temperature loss peaks.

Preliminary investigations into the local atomic structure at different areas of a heat-treated coating shows that increasing heat-treatment temperature causes more ordered coating material nearer the substrate, compared with areas nearer the surface of the coating.

Chapter 4 presents studies on the effect of doping Ta_2O_5 coatings with TiO_2 with doping concentrations of 0, 8.3, 20.4, 25.7, 28.3, 53.8 % (cation) TiO_2. Mechanical loss measurements of multi-layer SiO_2 and Ta_2O_5 doped with TiO_2 coatings show that changing the TiO_2 doping concentration reduces the mechanical loss of the coating by up to 40%. It is also shown that changing the TiO_2 doping concentration can significantly change the local atomic structure of these coatings. Atomic models created for 20.4% and 53.8% Ti coatings indicate similar inter-atomic bond distances between the 20.4% and 53.8% Ti coatings. The models show that the distributions of Ta-Ti and Ti-O bonds in the atomic structure of the coatings as TiO_2 doping is increased. There are also considerable contributions from Ta_2O_2 ring fragments that are seen in the pure Ta_2O_5 coatings, with the addition of $TaTiO_2$ ring fragments. Further analysis of the atomic structures of these coatings revealed some preliminary correlations between the atomic structure and mechanical loss, were it is observed that 28.3% Ti coating is the most ordered atomic state out of all the Ti doped coatings and had the lowest measured mechanical loss. This suggests that there may be a link between slightly increased ordering in the atomic structures and a lower measurable mechanical loss. The amount of oxygen in a coating may play a key role important in the level of mechanical loss, as it is observed that the coating with the least oxygen deficiency coating is the coating with the lowest measured mechanical loss.

Finally, Chapter 5 explores the material properties and atomic structures of HfO_2 coatings, SiO_2 coatings and substrates and HfO_2 doped with SiO_2 coatings. Pure HfO_2 are studied as possible alternatives to Ta_2O_5 coatings. It appears that coatings subject to heat during the manufacturing process of

just 100 °C or above appear part crystallised. Preliminary studies of a HfO$_2$ coating doped with 30% (cation) SiO$_2$ and heat-treated to 600 °C show that it is a promising coating for future study as it remains amorphous, with a room temperature mechanical loss value comparable to pure HfO$_2$ coatings and therefore Ta$_2$O$_5$ coatings. SiO$_2$ coatings deposited on SiO$_2$ substrates are also studied and they show only subtle changes between them, which appear to lessen as the sample are heat-treated. Changes in the atomic structure of these coatings indicate an increase in order of the structure as heat-treatment temperature is increased, similar to the observed changes in the heat-treated Ta$_2$O$_5$ coatings.

Chapter 1

Detecting Gravitational Waves

1.1 Introduction

One of the most intriguing and challenging areas of experimental physics encompasses the efforts made to detect gravitational waves from astrophysical sources. Gravitational waves are one of the predictions of Einstein's General Theory of Relativity, where asymmetrically accelerated mass emits ripples of gravitational radiation, gravitational waves [1]. For nearly a century they have remained elusive, but a new generation of ground-based interferometric detectors are reaching sensitivities where a first detection could be made. Detection of gravitational waves would open up an entirely new window on the Universe, allowing us to further understand its relativistic properties and initiate an entirely new area of astronomy.

Although there has been as yet no direct detection of gravitational waves, there is strong indirect evidence of their existence. In 1975 Hulse and Taylor discovered the binary pulsar PSR 1913 + 16 [2]. This binary pulsar system was observed over a number of years and was found to have a decaying orbit that followed a decay rate consistent with a model in which energy is lost due to gravitational radiation [3–5]. This discovery won Hulse and Taylor the Nobel Prize for Physics in 1993 and further strengthened the international effort to directly detect gravitational waves.

There is an international effort linking detector projects in an effort to make the first direct detection of gravitational waves. Currently, the most promising method of detection is focussed on the use of long-baseline interferometers such as LIGO in the US [6], GEO600 in Germany [7], Virgo in Italy [8] and TAMA in Japan [9]. These detectors are some of the most sensitive displacement measurement instruments ever to be constructed [10]. Upgrades are planned in the near future to several of these detectors, which should see their sensitivities increase significantly [11]. In general, detectors have sensitivities limited by a range of noise sources such as photo-electron shot noise [12], seismic noise [13] and thermal noise [14]. Finding ways to reduce these noise sources is a very active area of research, with the goal of developing new technologies and materials to enable the design and development of future generations of more sensitive detectors.

This chapter will give a brief introduction to the nature of gravitational waves and their sources. The second part of this chapter will then focus on the detectors, and the noise sources which limit their sensitivity with an emphasis on thermal noise.

1.2   Gravitational waves

1.2.1   The nature of gravitational waves

The General Theory of Relativity published by Albert Einstein in 1916 predicts the existence of gravitational waves travelling at the speed of light, produced when mass is accelerated asymmetrically [1]. These gravitational waves can be considered as having the effect of waves or ripples in space-time.

Following the description of gravitational waves in relativity given by Saulson [15], one of the central concepts to relativity is that the space-time interval, ds, between two points, where each point represents the position (t, x, y, z), say from point (x^0, x^1, x^2, x^3) to point $(x^0 + dx^0, x^1 + dx^1, x^2 + dx^2, x^3 + dx^3)$, can

be described mathematically by,

$$ds^2 = -c^2 dt^2 + dx^2 + dy^2 + dz^2. \tag{1.1}$$

When considering the curvature of space-time, Equation 1.1 can also take the more general form,

$$ds^2 = g_{\mu\nu} dx^\mu dx^\nu, \tag{1.2}$$

where $g_{\mu\nu}$ is known as the metric tensor and describes the local curvature of space-time and μ, ν can be $(0, 1, 2, 3)$ to represent (t, x, y, z) respectively. $g_{\mu\nu}$ is better described as,

$$g_{\mu\nu} = \eta_{\mu\nu} + h_{\mu\nu}, \tag{1.3}$$

where $\eta_{\mu\nu}$ is known as the Minkowski tensor and describes flat space, and and $h_{\mu\nu}$ describes the small perturbations in the curvature of space-time. The complicated mathematical expressions that describe Einstein's gravitational field equation can be simplified when a suitable form of $h_{\mu\nu}$ is chosen. This choice lies in the *transverse traceless gauge* or TT gauge, and allows the field equation to be represented as a wave equation,

$$\left(\nabla^2 - \frac{1}{c^2} \frac{\partial^2}{\partial t^2} \right) h_{\mu\nu} = 0. \tag{1.4}$$

The TT form of $h_{\mu\nu}$ when a wave is moving out along the z-axis is

$$h_{\mu\nu} = \begin{pmatrix} 0 & 0 & 0 & 0 \\ 0 & h_{xx} & h_{xy} & 0 \\ 0 & h_{yx} & h_{yy} & 0 \\ 0 & 0 & 0 & 0 \end{pmatrix}. \tag{1.5}$$

where $h_{xx} = -h_{yy}$ and $h_{xy} = h_{yx}$. This gives rise to two polarisations of gravitational radiation, h_{xx} and h_{xy}, that shall be denoted at h_+ and $h_\times$ respectively at $45\,^\circ$ to one another. An example of how gravitational radiation distorts a ring of test particles from these two polarisations is shown in Figure 1.1.
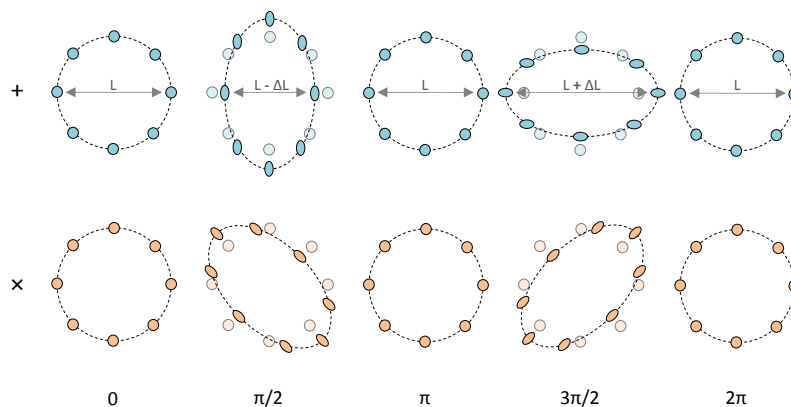
Figure 1.1: *The effect of a gravitational wave with (a) the h_+ and (b) $h_\times$ polarisation, incident normal to the page, on a ring of test particles.*

It is possible to quantify this distortion by considering the displacement of test particles caused by the incident wave. A ring of particles of radius L is stretched in one direction by ΔL and compressed in the orthogonal direction by the same amount, as shown in Figure 1.1. The resultant amplitude of the strain produced is defined as,

$$h = \frac{2\Delta L}{L}. \tag{1.6}$$

This property forms the basis of the operational principles of gravitational wave detectors. Further description of these detectors will follow in Section 1.3.

1.2.2 Sources of gravitational waves

Gravitational waves are extremely weak in nature due to gravity being the weakest of the forces of nature. Thus, only naturally occurring astronomical events that involve very large masses and accelerations produce gravitational waves large enough to detect. It is worth noting that even from these massive astronomical events, a detectable strain of just $h \sim 10^{-21}$ is expected [16].

Astrophysical sources of gravitational waves are often classified into three main types: burst sources, continuous sources and a stochastic background, and these will be discussed in turn.

Burst sources

Certain source classes produce short bursts of gravitational waves which occur over timescales from milliseconds to minutes. These sources include, for example, coalescing compact binary systems and supernovae. Compact binary systems may be formed, for example, by two black holes, two neutron stars or a combination of a black hole and a neutron star. As a binary system inspirals, it emits gravitational waves. Schutz estimated the strain in space-time to be [17],

$$h \approx 1 \times 10^{-23} m_T^{\frac{2}{3}} \mu \left(\frac{f}{100 \text{Hz}} \right)^{\frac{2}{3}} \left(\frac{100 \text{Mpc}}{r} \right), \qquad (1.7)$$

where $m_T = m_1 + m_2$, $\mu = m_1 m_2 / (m_1 + m_2)$ which is the reduced mass of the system, f is the radiation frequency emitted from the system and r is the distance from a detector. Supernovae, the violent explosions that marks the end of stars lives, produce strains estimated to be $h \sim 1 \times 10^{-21}$ at a distance of 10 kpc from the source [18].

Continuous sources

Example of continuous sources of gravitational radiation include pulsars and X-ray binaries. Pulsars are highly magnetised, spinning neutron stars, that have jets of particles ejecting from their magnetic poles. Pulsars, and neutron stars in general, are the result of the gravitational collapse that occurs during supernovae explosions of massive stars. Gravitational waves emitted from these are believed to produce strains of [19],

$$h \approx 6 \times 10^{-25} \left(\frac{f_{rot}}{500 \text{Hz}} \right)^2 \left(\frac{1 \text{kpc}}{r} \right) \left(\frac{\epsilon}{10^{-6}} \right), \qquad (1.8)$$

where T_{obs} is the total time the pulsar is observed over and ϵ is the equatorial ellipticity. Recent studies have given an upper limit of the strain signal from these sources set at $h \sim 10^{-24}$ [20]. There is another particular system that includes a neutron star with the addition of a normal companion star, known

as low-mass X-ray binaries. These systems have deforming spinning neutron stars that produce gravitational waves as the neutron star is torqued by the accretion from the companion star.

The stochastic background

The stochastic background is not a source in itself, rather it can be regarded as similar to the cosmic microwave background in that it is the background noise of which individual sources cannot be resolved. The expected strain signal of the stochastic background is [6],

$$h \approx 4 \times 10^{-22} \sqrt{\Omega_{\text{gw}}} \left(\frac{f}{100\text{Hz}} \right)^{-\frac{3}{2}} \text{Hz}^{\frac{1}{2}} \tag{1.9}$$

where Ω_{gw} is the energy density required for a closed Universe. Observations from the stochastic background will provide information on the structure of the early Universe and is one of the major ambitons for gravitational wave astronomy.

1.3 Gravitational wave detectors

Gravitational wave detectors have been in development for over 50 years [15]. In the 1960s, Weber pioneered the design of the first gravitational wave detectors [21]. Weber's attempts to detect gravitational waves included monitoring of resonant modes of aluminium bars, which would be excited by a passing gravitational wave of sufficient amplitude [22]. Weber published several claims of direct detection of gravitational waves from bar detectors [23, 24], however subsequent bar detectors set up around the world failed to verify Weber's results [25–28]. Bar detectors have the disadvantage of only being able to operate over narrow bandwidths that are centered on the resonant modes of the bar.

In 1962 Gartsenshtein and Pustovit [29] first proposed laser interferometry as a way to precisely measure the differential motion of test masses. Such

differential motion may be the result of a passing gravitational wave, which would cause strains or fractional changes in length in space. Therefore, laser interferometry provided the possibility of detecting gravitational waves. It was also a very attractive technology as it had the ability to provide high sensitivity over a broad range of frequencies [30], and has subsequently become the technology of choice for detecting gravitational waves [31].

1.3.1 Laser interferometry

The use of laser interferometry for gravitational wave detection focusses on variants of the Michelson interferometer. In this type of interferometer, a laser beam is split into two components which then travel at right angles to one another. The two separate beams travel along 'arms' and then retroreflect at the end test mass mirrors and recombine at the photodetector where they interfere, as shown in Figure (1.2).
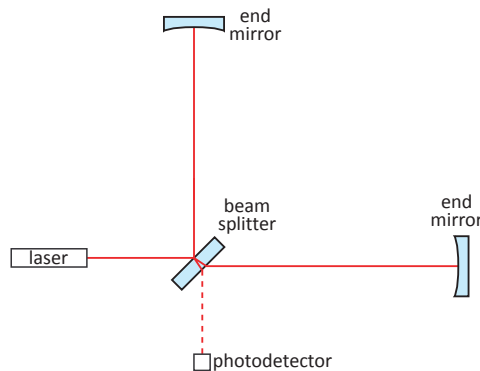
Figure 1.2: *Schematic of a Michelson interferometer consisting of one beam splitter and two end mirrors.*

The first use of laser interferometry goal of detecting gravitational waves was by Forward [32] and Weiss [30]. The effect of a passing gravitational wave will lengthen one arm and compress the other causing a variation in the intensity of light sensed at the photodetector. The observed change in arm length is described by Equation 1.6, which also indicates having long armlengths will increase the measured change in arm length, and therefore increase

the variation of light sensed at the photodetector, when a gravitational wave passes.

Modern interferometric gravitational wave detectors have long baselines or arm lengths. As these are ground-based, practical arm lengths are restricted to several kilometers, mainly due to cost and the curvature of the Earth affecting the requirement for straight beamlines. Of the interferometers currently constructed, the LIGO detectors are the largest and have 4km arms, Virgo, GEO600 and TAMA have 3 km, 600 m and 300 m arms, respectively.

A range of technologies have been developed and employed to maximise gravitational wave sensitivities, forming extensions of the simple Michelson interferometer.

Delay-line interferometry

Increasing the effective arm length of the interferometer can be accomplished by increasing the optical path length of the arms. In 1972 Weiss proposed the use of an optical delay-line interferometer whereby the interferometer uses either a folded optical path, as shown in Figure 1.3(a), or where mirrors close to the beam splitter have an aperture that allows light to enter the arm and bounce back an forth several times before exiting, as shown in Figure 1.3(b) [30, 33]. The GEO600 detector employs a folded delay-line configuration [34].

Fabry-Perot interferometry

There is also a further method, that was adapted for use in gravitational wave detectors in Glasgow [35], for increasing the optical path length using Fabry-Perot resonator cavities, as shown in Figure 1.4. Here, the inner mirrors situated close to the beam-splitter are partially transmitting and the end mirrors are highly reflective. The cavities are held at resonance during operation and the light is effectively stored in the cavities, travelling multiple times to and from the inner and outer mirrors, before essentially 'leaking' out back to the
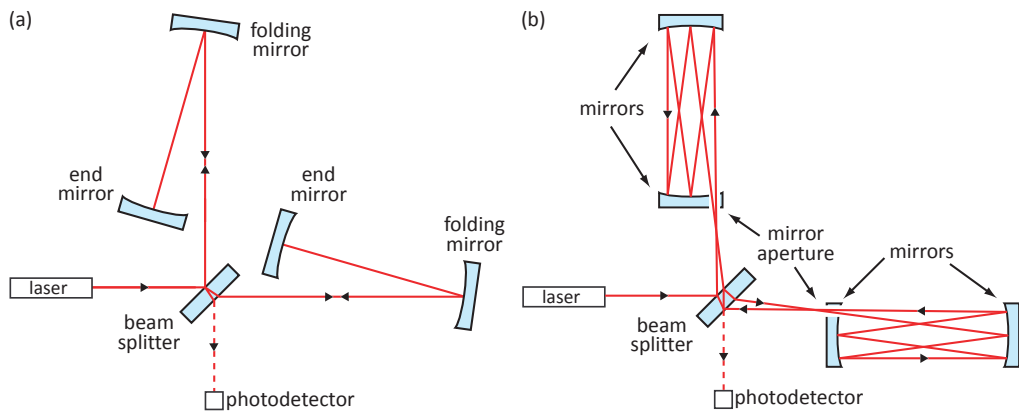
Figure 1.3: *Schematic of an interferometer in a delay-line configuration where the optical path length is extended by a folded optical path using (a) separate mirrors or (b) by an input mirror with an aperture for the input and output laser beams.*

beam splitter and to the photo-detector. This method is currently employed in the LIGO, VIRGO and TAMA detectors [36].
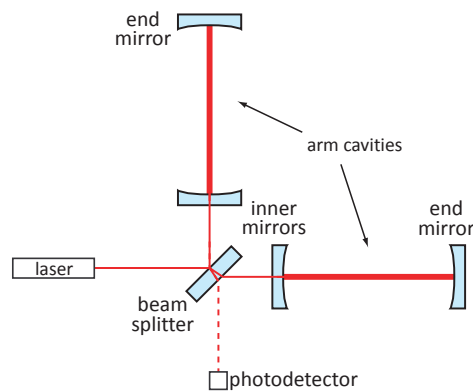
Figure 1.4: *Schematic of an interferometer implementing Fabry-Perot resonator cavities, effectively increasing the arm length of the interferometer.*

Power and signal recycling

Techniques have also been developed to enhance the output signal of the detectors. Power recycling focuses on 'recycling' the light coming out of the interferometer arms [37]. As the light travels back from the interferometer arms to the beam splitter, some of this light is transmitted back along the

laser input path. Putting an additional mirror in the input line, as shown in Figure 1.5 (a), allows the light coming back out of the arms to be recycled by creating a cavity with the interferometer.

In signal recycling a partially transmitting mirror is placed between the beam-splitter and the photo-detector, as shown in Figure 1.5 (b), allowing light to be recycled back into the detector in a similar way to power recycling, but specifically for light at the frequency of the sidebands produced by the effects of passing gravitational waves [38] [39]. The detectors essentially work by producing destructive interference at the photo-detector, it is therefore possible to enhance the sensitivity at certain frequencies of interest by accurately positioning of the signal recycling mirror.
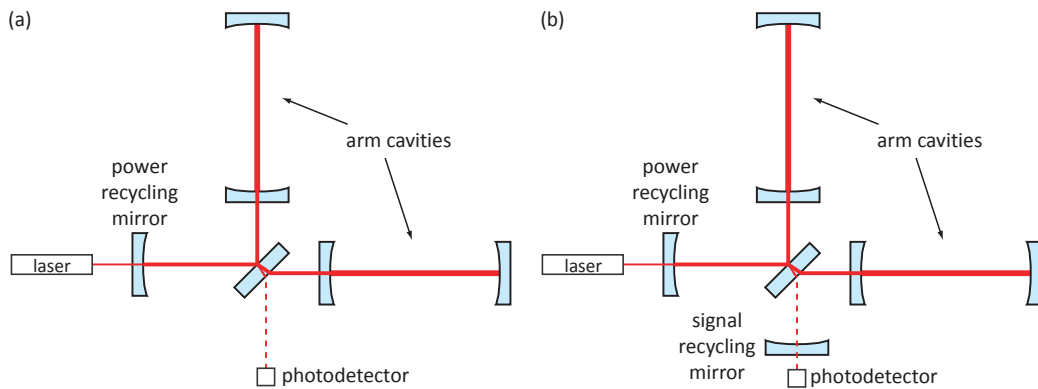
Figure 1.5: *Schematic of an interferometer with (a) a power recycling mirror at the input line from the laser, forming a further optical cavity with the interferometer and (b) the addition of a signal recycling mirror in the output beam line.*

In both power and signal recycling cases the amount of light stored in the detector effectively increases. Therefore this increases the detector sensitivity to differential displacements in the arm lengths that may be caused by passing gravitational waves.

1.4   Detector noise sources

Three of the most significant sources of noise in the current ground-based interferometric detectors are photon noise, seismic noise and thermal noise [15]. Photon noise is a result of statistical fluctuations in the detection of light by the photodetector at the interferometer output. Seismic noise is caused by vibrations of the ground and can be reduced by suspending the test masses and optical equipment as pendulums. Thermal noise is a result of the thermally excited motion of the test masses, their mirrors and suspensions and is an important fundamental limit to detector sensitivity at the most sensitive frequency range of these detectors. These noise sources are discussed further in the following subsections.

1.4.1   Photon noise

Photon shot noise

Photon shot noise describes the statistical fluctuations of the packets of photons detected from the output signal of a gravitational wave detector at the photodetector. In Poisson statistics, N photons reaching the photodiode would have $\sqrt{N}$ error associated with this signal. This gives rise to a limit to detector sensitivity.

The effect of photon shot noise can quantified in terms of its effect on the strain sensitivity for a simple Michelson interferometer, previously defined in Equation 1.6, as a function of frequency, $h_{\text{shot}}(f)$, in the following way [40],

$$h_{\text{shot}}(f) = \left(\frac{\pi \hbar \lambda}{2 P_{\text{in}} \varepsilon c} \right)^{\frac{1}{2}} \frac{f}{\sin(\pi f \tau)}, \tag{1.10}$$

where $\hbar$ is the reduced Planck's constant, P_{in} is the input power of the laser with a wavelength λ, ε is the quantum efficiency of the photodiode, c is the speed of light, f is the gravitational wave frequency and τ is the time that light is stored in the detector. From inspection of this relationship it can be seen

that it is possible to reduce the effect of photon shot noise by increasing the power of the laser used. It can also be further reduced by setting $\tau = 1/(2f)$, where the length of storage time is set to half the period of a gravitational wave. Thus high power lasers are used in these detectors and methods of power and signal recyclying (see section 1.3.1) are adopted [38, 39].

Radiation pressure noise

Increasing the laser power in a detector has an associated noise effect, that of radiation pressure noise. This effect results from the fact as the photons hit the suspended mirrors, momentum is transferred from the photons to the test masses, causing them to move. For a simple Michelson interferometer the effect on strain sensitivity from radiation pressure noise, h_{rp}, can be described by [15],

$$h_{\mathrm{rp}} = \frac{N}{mf^2L}\sqrt{\frac{2\hbar P_{\mathrm{in}}}{\pi^3\lambda c}}, \tag{1.11}$$

where N is the number of times the light in the interferometers travels a distance of $2L$, L being the length of the interferometer arms, and m being the mass of the mirrors. From this it can be seen that radiation pressure noise reduces with increasing frequency and increases as P_{in} increases.

The standard quantum limit

From Equations 1.10 and 1.11 it can be seen that an optimum value for P_{in} exists for any given frequency such that $h_{\mathrm{shot}} = h_{\mathrm{rp}}$. This arises as discussed above, since when the laser power is increased the effects of photon shot noise are decreased and the radiation pressure is increased, and vice versa. This therefore must set a limit to detector sensitivity, where $h_{\mathrm{shot}} = h_{\mathrm{rp}}$, and is known as the Standard Quantum Limit (SQL). Current detectors all have noise floors higher than that set by the SQL. As detector sensitivity is increased, designs are being tested which should reach the SQL and may overcome it by correlating the photon shot noise and radiation pressure noise through the use

of 'optical springs' and signal recycling [41]. Discussion of these methods lie outwith the scope of this thesis, and further information can be found in the literature [41–44].

1.4.2   Seismic noise

Indirect coupling of seismic noise

Current interferometric gravitational wave detectors are based on Earth, although plans exist for space-based detectors (see Section 1.5 for further details). The terrestrial environment presents another source of noise - seismic noise. There are many, often unpredictable, sources of seismic noise that can take various forms, from earthquakes to human activity such as road traffic. Thus it is important to isolate the detector test masses from these noise sources as far as possible [15]. To that effect, vibration isolation stacks [15, 45] and multi-stage pendulums [46] have been used in order to effectively filter out seismic noise to a level where it does not limit detector sensitivity.

Isolation in the vertical direction can be achieved effectively through a stacked set of springs or cantilever springs. Horizontal isolation can be achieved through the use of pendulums. The transfer function of a pendulum between the displacements of the pendulum's clamping point x_{clamp} and mass x_{mass} is given by [15],

$$\frac{x_{\mathrm{mass}}}{x_{\mathrm{clamp}}} = \frac{f_{\mathrm{r}}^2}{f_{\mathrm{r}}^2 - f^2},$$

(1.12)

where f_{r} is the resonant frequency of the pendulum and f is the frequency of the ground motion. For the case where N pendulums are stacked on top of each other, for a $f \gg f_r$, the attenuation of the test-masses can be described by

$$\frac{x_{\mathrm{mass}}}{x_{\mathrm{clamp}}} \approx \left(\frac{f_{\mathrm{r}}^2}{f^2}\right)^N.$$

(1.13)

Multi-stage suspension systems have been used effectively in the GEO600 [46] and Virgo [47] detectors and will be part of the planned upgrade to LIGO [48], see Section 1.5 for further details.

Directly coupling seismic noise

A fundamental limit to ground based interferometric detector sensitivity results from seismic motions that are directly coupled to the detector test masses through gravitational effects [49]. This noise source arises from local changes to the gravitational field, referred to as gravitational gradient noise [13]. There is no easy way of isolating this noise source and it currently sets a lower limit to the operational frequency range of planned detectors, limiting sensitivity in the range of around 10 Hz or less. However proposals are being put forward to build underground detectors, such as the Einstein Telescope [50] and LCGT [51], where the effect of local distortions to the gravitational field can be reduced. Isolation from this noise source would also be achieved by the proposed space based detectors (see Section 1.5).

1.4.3   Thermal noise

Thermal noise is a major limit to detector sensitivity in the frequency range of a few tens Hz to several 100 Hz [52] where detectors are most sensitive. It arises from the thermally excited motion of the atoms and molecules in the materials used in the interferometers, particularly from the test masses, their mirror coatings and suspensions. There are two forms of thermal noise in detector optics, one from internal friction, due to localised sources of mechanical loss such as defects in the structure of the material, and the other from effects due to statistical fluctuations in temperature [53]. Thermal noise from mechanical loss, or 'Brownian noise', can be described in terms of the thermal energy associated with each resonant mode of the material, which equates to $\frac{1}{2}k_\mathrm{B}T$ per degree of freedom. Statistical temperature fluctuations in a material can couple to properties such as local expansion and changes in refractive index, collectively giving rise to a noise source referred to as 'thermo-optic' noise [53].

To reduce Brownian thermal noise it is therefore preferable to use materials for the test-masses and their suspensions with low mechanical loss, such as

ultra-pure fused silica [54, 55], to reduce its effect. A particularly significant source of thermal noise is that arising from mechanical loss of the mirror coatings applied to the test masses. Thus, a considerable amount of research is being carried out to understand, and find ways of reducing coating mechanical loss [52]. Further discussion of both aspects of thermal noise in the coatings will be given in Chapter 2.

1.4.4 Direct impact of noise sources on gravitational wave detectors

The combined effect of the noise sources mentioned in this section on detector sensitivity can be seen in Figure 1.6. Here the theoretical noise sources for Advanced LIGO (see Section 1.5) are shown [56].

There is an additional noise source not mentioned in the previous sections from the effect of residual gas. The detectors are operated in an ultra high vacuum environment. However it is impossible to produce a perfect vacuum and there will be a small amount of residual gas and that will in turn scatter some of the laser beam [57].

1.5 Current and future interferometric gravitational wave detectors

Current generation of detectors

As stated previously, there is an international network of ground-based long-baseline interferometric gravitational wave detectors. The largest of these are part of the Laser Interferometer Gravitational-wave Observatory (LIGO) project in the US [6]. There are three LIGO interferometers, a 4 km and 2 km arm length detector near Hanford in Washington State and another 4 km arm length instrument near Livingston in Louisiana [54]. Other gravitational wave detectors include the GEO600 interferometer located near Hanover in
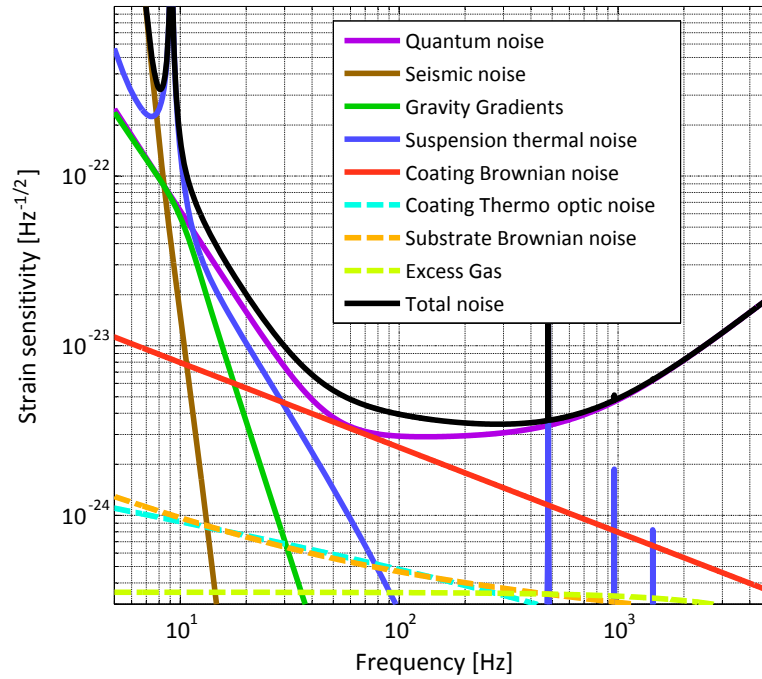
Figure 1.6: *Plot showing the noise budget for Advanced LIGO (see Section 1.5) where the different noise sources are combined to produce the total noise and subsequent sensitivity plot for the detector [56].*

Germany [7], the Virgo interferometer located near Pisa [8] and the TAMA interferometer located in Tokyo [9]. They all compare results by working together, when they are all operational, to rule out local anomalies such as earthquakes, weather conditions and disturbances from other sources such as aircraft. They will also be able to use triangulation to determine the origin of the detected gravitational waves in space. Figure 1.7 shows images of one of the LIGO detectors, Virgo and GEO600.

Figure 1.8 shows some of the most recent sensitivity curves from recent observing periods from the 4km LIGO, GEO600 and Virgo detectors.

Second generation of detectors

There are upgrades planned for the GEO600, LIGO and Virgo detectors with the aim of improving detector sensitivities. GEO-HF will see the original GEO600 detector optimised to improve sensitivity in the high frequency ranges,

Figure 1.7: *Images showing three of the major international long-baseline interferometric gravitational wave detectors, with (a) the LIGO detector in Louisiana (US) [58], (b) the Virgo detector near Cascina (Italy) [59] and (c) the GEO600 detector near Hanover (Germany) [60].*
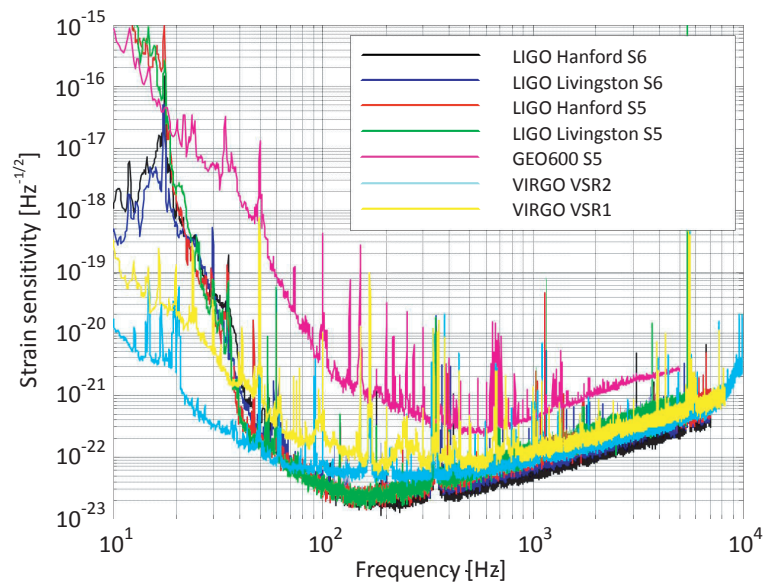
Figure 1.8: *Sensitivity plots for the LIGO science run 6 (S6) [61], GEO600 S5 [62] and VIRGO science run (VSR1 and 2) [63] from recent observation periods.*

mainly by decreasing photon-shot noise with a more powerful stable laser. It will also have the option of switching to being optimised for lower-frequency observations.

The two 4 km LIGO detectors have recently finished their final observation period before their upgrade to form an 'Advanced LIGO', which aims to achieve an improvement in detector sensitivity by a factor of at least 10 [64]. Increasing sensitivity, effectively increases the volume of the Universe from which grav-

itational waves may be observed, making a detection more likely. Advanced LIGO will increase the volume of the Universe initial LIGO is sensitive to by as much as 1000 times [65]. Technologies developed in GEO600 including silica fibre suspensions developed in Glasgow will be part of the upgrade [66].

The upgrade of Virgo to Advanced Virgo will also aim to improve detector sensitivities to a level that is essentially that of Advanced LIGO and will also implement the use of silica suspensions [67]. Upgrading to Advanced Virgo is expected to start in 2011.

In Japan, there are plans for an underground detector with 3 km arm-lengths to be built, the Large-scale Cryogenic Gravitational wave Telescope (LCGT), and has recently had its funding approved [51]. The Cryogenic Laser Interferometer Observatory (CLIO) is a prototype 100 m arm-length detector testing the technologies, particularly the cryongenics, that will be used in LCGT [51].

Both GEO600 and some bar detectors will have the important task of continuing observations during the more demanding upgrades required for Advanced LIGO and Advanced Virgo.

Third generation of detectors

The second generation of detectors will almost certainly make the first direct detection of gravitational waves [66]. However, the detection rate of these detectors is expected to be around 40 events per year, in the case of coalescing compact binary systems [68], making it unlikely for them to give the ability to perform precise astronomical studies of gravitational wave sources [50]. Therefore the international gravitational wave community is in the early stages of investigating possible third generation detectors, which will see considerable further improvements to sensitivity [50]. There are options being considered for future US detectors, including an upgrade to Advanced LIGO. In Europe, a design study for the Einstein Telescope (ET) is underway with ambitious targets for reducing several noise sources; including reducing seismic noise by

building it underground and cryogenic cooling for the optics to reduce thermal noise [50, 69]. These detectors will aim to make frequent detections of gravitational waves at high signal to noise ratios, giving rise to a new era of routine gravitational wave astronomy [50].

Space based detectors

There are currently plans for two space-based detectors, the Laser Interferometer Space Antenna (LISA) scheduled for launch in 2020 [70] and the DECihertz Interferometer Gravitational wave Observatory (DECIGO) scheduled for launch in 2024 [71]. Both of these detectors will operate in space, isolating them from the seismic noise sources relevant for ground-based detectors, allowing the frequency bandwidth they are sensitive in to be significantly lower than their ground-based counterparts. LISA's operating frequency bandwidth will allow it to observe the formation of massive black holes of the order of $10^3 - 10^6 \ M_\odot$ from frequencies of around $10^{-4} - 10^{-1}$ Hz. DECIGO will operate in the frequency range between LISA and ground-based detectors searching for inspiral sources producing gravitational emission that has moved out of the detectable frequency range of LISA and before they move up into the detectable frequency range of ground-based detectors. The sensitivity to lower frequencies of both LISA and DECIGO could possibly give them the opportunity to study the stochastic background, allowing the study of gravitational radiation from the early Universe [72, 73]. LISA and DECIGO will have arm lengths of 5×10^6 km and 1000 km, respectively, also giving them increased sensitivity, which is achievable because they are space based. They will consist of three drag-free space craft each allowing them to triangulate the origin of any detections, and trail the Earths orbit around the Sun, as illustrated in Figure 1.9. There is also a preliminary mission planned called LISA Pathfinder which is a space probe scheduled for launch as early as 2013 that will test some of the key components that will be eventually be used in the LISA detector.
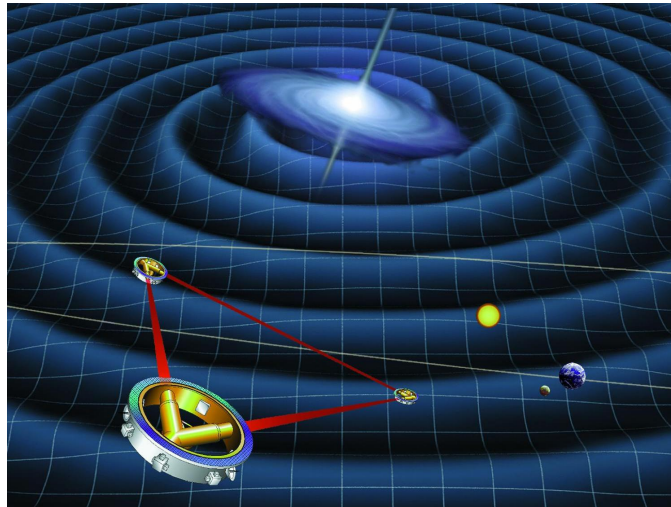
Figure 1.9: *An artists interpretation of the LISA space-based gravitational waves detectors trailing the Earth's orbit around the Sun, showning gravitational waves being emitted from a massive black hole binary system [74].*

1.6 Conclusions

The detection of gravitational waves will create an entirely new window to the Universe, giving birth to a new era in Astronomy. Astronomical events that are of interest tend to involve compact objects, for example, the collapse of a star, in an event known as a supernova, to a black hole or neutron star producing a burst of gravitational waves. Coalescing compact binaries produce gravitational waves as the system inspirals. Gravitational wave interactions from the early Universe may allow us to peer significantly further back in time than is currently possible. However gravitational waves emitted from the strongest source are anticipated to produce detectable strains of just $h \approx 10^{-21}$.

Long-baseline interferometric detectors currently provide the most promising way to make a detection, and there is an international network of detectors and scientific research observing and developing the most sensitive displacement measurement instruments ever to be created. These detectors are now sensitive enough to make a detection but are still limited by noise sources that include photon, seismic and thermal noise. Innovative methods and technolo-

gies are being developed for future generations of detectors to reduce noise sources and thus increase detector sensitivity, therefore increasing the volume of the Universe observable and increasing the chances of detecting the first gravitational wave.

The research presented in this thesis focuses on the development of low mechanical loss and hence low thermal noise coatings, which currently limits the most sensitive frequency ranges of current detectors. Understanding what is causing the thermal noise in these coatings is an area of intense research, in an attempt to produce coatings that reduce its effect. The following chapters will outline the techniques used to probe the material properties of the coatings, and for the first time gain a detailed understanding of their atomic structures.

Chapter 2

Methods for investigating the material properties of mirror coatings

2.1 Introduction

Thermal noise from the mirror coatings applied to the test masses of interferometric gravitational wave detectors is an important limiting factor to detector sensitivity over the central portion (tens Hz to several 100 Hz [65, 75]) of its operational bandwidth, due mainly to the mechanical dissipation of the coating material [52]. It is therefore important to understand the nature of coating thermal noise by accurately quantifying its effect and identifying its causes, in an effort to design future coatings of lower thermal noise.

Ta_2O_5 has been widely used in the optical industry as a high quality dielectric coating material that has low optical loss [76]. Dielectric mirror coatings used in gravitational wave detectors consist of alternating layers of materials that have varying refractive index to give high reflectivity. Currently all operational interferometric gravitational wave detectors employ coatings formed from multi-layers of SiO_2 (silica) and Ta_2O_5 (tantala) [77].

This chapter introduces the current understanding of the thermal noise properties of the coatings and the way it can be measured. Then, in order to

gain a full representation of the thermal noise, studies have been carried out to look at the atomistic properties of the coatings, with the goal of identifying possible changes in the atomic structure that produce changes in the measured thermal noise properties. Therefore the theory behind transmission electron microscopy is discussed, and the techniques used in order to probe the atomic structure and chemistry of these coatings are described.

2.2 Aspects of thermal noise

2.2.1 Brownian motion and the fluctuation dissipation theorem

The test masses and suspensions will experience random Brownian motion of their atoms and molecules due to being at some finite temperature. This appears as thermally driven motion of the resonant modes of the system. There is a link between this thermal motion and the mechanical loss (or internal friction) of the materials making up the test masses and their suspensions as described by the fluctuation-dissipation theorem [78, 79].

The fluctuation-dissipation theorem can be used to relate the power spectral density of the thermal displacement, $S_x(\omega)$ at some frequency ω, to the real part of the mechanical impedance, $Z(\omega)$ such that,

$$S_x(\omega) = \frac{4k_\mathrm{B}T}{\omega^2}\Re\left[\frac{1}{Z(\omega)}\right].$$

(2.1)

When an external force is applied to the test mass, the test mass material responds, but not instantaneously. Instead there is a lag in the strain response. When the internal stress in a material changes, internal properties of the material such as defects, shifting grain boundaries and thermal currents take time to respond [57].

It is possible to model the vibrational modes of each test mass as a lightly damped harmonic oscillator [57],

$$F(\omega) = -kx\left(1 + i\phi(\omega)\right),$$

(2.2)

where k is the spring constant and $\phi(\omega)$ is the loss factor, which represents the phase lag of the response of the system, x, to the restoring force, $F(\omega)$. Taking into account the combined effects of internal friction, it is possible to express Equation 2.2, in terms of velocity, v, such that,

$$F(\omega) = i\omega m v - i\frac{k}{\omega}\left(1 + i\phi(\omega)\right)v, \qquad (2.3)$$

where m is the mass of the test mass. The impedance, $Z(\omega)$, can be obtained by dividing Equation 2.3 by the velocity, v and then substituting it into the fluctuation dissipation theorem, Equation 2.1, such that [57],

$$S_x(\omega) = \frac{4k_{\mathrm{B}}T}{\omega^2}\frac{\omega_0^2\phi(\omega)}{m\left(\omega_0^4\phi^2(\omega) + (\omega_0^2 - \omega^2)^2\right)} \ \text{ per Hz.} \qquad (2.4)$$

From this it can be seen that, at frequencies far from the resonant frequency, ω_0, using materials for the test mass with low loss will give lower mechanical dissipation, and therefore lower thermal noise.

2.2.2 Brownian and thermoelastic noise of the mirror coatings

Brownian thermal noise The thermal noise associated with the test-mass mirrors can be calculated by applying the fluctuation dissipation theorem to the interferometer readout position of the test-mass face, and was first carried out by Levin [80].

The thermal noise can be calculated from the power dissipated in the test-mass mirror, when assuming the application of pressure identical to the spatial profile of the laser beam to the front face of the test-mass mirror. The fluctuation dissipation theorem can then be used to calculate the power spectral density , $S_x(f)$, of the thermal displacement so that [80],

$$S_x(f) = \frac{2k_{\mathrm{B}}T}{\pi^2 f^2}\frac{W_{\mathrm{diss}}}{F_0^2}, \qquad (2.5)$$

where W_{diss} is the power dissipated in the mirror and F_0 is the peak amplitude of the notional oscillatory force. The dissipated power, W_{diss}, can be written as,

$$W_{\mathrm{diss}} = 2\pi f U_{\mathrm{max}}\phi(f), \qquad (2.6)$$

where U_{max} is the total energy associated with the peak elastic deformation of the test mass.

Bondu [81], Liu and Thorne [82] subsequently showed that the test mass can be modelled as a half infinite structure if the laser beam radius is considerably smaller than the test-mass radius. For this case, the thermal noise power spectral density of the half infinite test mass, $S_x^{\text{ITM}}(f)$, can be shown to be [81],

$$S_x^{\text{ITM}}(f) = \frac{2k_{\text{B}}T}{\pi^{3/2}f}\frac{1-\sigma^2}{Yw_0}\phi_{\text{substrate}}(f), \tag{2.7}$$

where $\phi_{\text{substrate}}(f)$ is the mechanical loss associated with the test-mass material, σ is the Poisson's ratio, Y is the Young's modulus of the material, respectively, and w_0 is the radius of the laser beam, where the amplitude of the electric field has fallen to $1/e$ of its maximum intensity.

Equations 2.5 and 2.6 demonstrate that thermal noise in the test-mass mirror is directly related to the power dissipated through the test-mass when an oscillating pressure is applied to the surface. In particular this highlighted that mirror coatings, deposited on the surface of the test-mass mirrors where deformation from the oscillating pressure is at its maximum, could be a significant source of thermal noise [80].

Nakagawa et al [83] derived an expression for the total power spectral density of the thermal noise associated with a multi-layer mirror coating following Levin's method, where the coating was expressed as a thin surface layer, d, with mechanical loss, ϕ_{coating}, such that [83],

$$S_x(f) = \frac{2k_{\text{B}}T}{\pi^{3/2}f}\frac{1-\sigma^2}{w_0Y}\left(\phi_{\text{substrate}} + \frac{2}{\sqrt{\pi}}\frac{(1-2\sigma)}{(1-\sigma)}\frac{d}{w_0}\phi_{\text{coating}}\right), \tag{2.8}$$

A further expression that incorporated the layer structure of the mirror coating, as well as allowing for the differing properties of the coating and the substrate, was derived by Harry *et. al.* [75]. In addition, the coating mechanical loss factor was separated into two components, $\phi_{\perp}$ and $\phi_{\parallel}$, from the associated parallel and perpendicular strains to the coating surface, respectively. The

derived expression by Harry *et. al.* for the thermal noise power spectral density of such a mirror coating can be shown to be [75],

$$
\begin{aligned}
S_x(f) \quad = \quad & \frac{2k_{\mathrm{B}}T}{\pi^{3/2}f}\frac{1-\sigma^2}{w_0 Y}\left\{\phi_{\mathrm{substrate}} + \frac{1}{\sqrt{\pi}}\frac{d}{w_0}\frac{1}{YY'(1-\sigma'2)(1-\sigma^2)}\right. \\
& \times [Y'^2(1+\sigma)^2(1-2\sigma)^2\phi_{\parallel} \\
& + YY'\sigma'(1+\sigma)(1+\sigma')(1-2\sigma)(\phi_{\parallel}-\phi_{\perp}) \\
& \left. + Y^2(1+\sigma')^2(1-2\sigma')^2\phi_{\perp}]\right\},
\end{aligned}
\tag{2.9}
$$

where Y and σ are the Young's modulus and Poisson's ratio of the substrate, respectively, Y' and σ' are the Young's modulus and Poisson's ratio of coating, respectively, and d is the thickness of the coating.

For coatings of alternating layers of SiO_2 and Ta_2O_5 deposited on fused SiO_2 substrates, the Poisson's ratio becomes small enough so that $\sigma' = \sigma = 0$. Thus Equation 2.9 can be approximated to within 30% to give an expression for the thermal noise power spectral density of a coated test mass [75]:

$$
S_x(f) = \frac{2k_{\mathrm{B}}T}{\pi^{3/2}f}\frac{1}{w_0 Y}\left\{\phi_{substrate} + \frac{1}{\sqrt{\pi}}\frac{d}{w_0}\left(\frac{Y'}{Y}\phi_{\parallel} + \frac{Y}{Y'}\phi_{\perp}\right)\right\}.
\tag{2.10}
$$

Thermoelastic thermal noise   The varying thermo-mechanical properties of the different materials used for the substrate and in the multi-layer coatings give rise to another source of noise called thermoelastic noise, which defines an important limit to detector sensitivity. Thermal expansion, described by the thermal expansion coefficient, α, of the coating material gives rise to displacements in the front mirror surfaces when small temperature variations are present. Braginsky [84] and Fejer [85] have calculated the spectral density of thermoelastic thermal noise arising from a dielectric coating of thickness d to be,

$$
S_x(f) \approx \frac{8k_{\mathrm{B}}T^2}{\pi\sqrt{2\pi f}}\frac{d^2}{w^2}(1+\sigma_{\mathrm{s}})^2\frac{C_{\mathrm{avg}}^2}{C_{\mathrm{s}}^2}\frac{\alpha_{\mathrm{s}}^2}{\sqrt{\kappa_{\mathrm{s}}C_{\mathrm{s}}}}\tilde{\Delta}^2,
\tag{2.11}
$$

where the subscript s denotes a substrate property, C is the specific heat

capacity, κ is the thermal conductivity, σ is Poisson's ratio and,

$$\tilde{\Delta}^2 \equiv \left\{ \frac{C_s}{2\alpha_s C_{\text{avg}}} \left[\frac{\alpha}{1-\sigma} \left(\frac{1+\sigma}{1+\sigma_s} + (1-2\sigma_s)\frac{Y}{Y_s} \right) \right]_{\text{avg}} - 1 \right\}^2, \qquad (2.12)$$

which takes into account varying thicknesses of the different coating material layers.

Equations 2.10 and 2.11 describe key contributions to our understanding of the current model for levels of coating thermal noise. In order to gain a full understanding of coating thermal noise and reduce its effects, we first need to measure the mechanical loss of coatings of interest and quantify the coating material properties. This will allow us that to choose materials with low mechanical loss that perform well in new detector designs, which may include operating at cryogenic temperatures.

2.3 Measuring the mechanical loss

2.3.1 Mechanical loss at resonant modes

The levels of mechanical dissipation (or mechanical loss) of the test masses and their suspensions are typically small, making them difficult to measure directly at all frequencies. Instead it is convenient to measure the loss at the resonant frequencies of the test masses and suspensions. The mechanical loss of the resonant mode system at an angular resonant frequency of, ω_0, is defined as [86],

$$\phi(\omega_0) = \frac{E_{\text{dissipation}}}{2\pi E_{\text{stored}}}, \qquad (2.13)$$

where $E_{\text{dissipation}}$ is the energy dissipated or lost within each oscillation and E_{stored} is the total energy stored in the vibrating system.

In studies of the mechanical loss of systems, the amplitude of the motion of a system is excited at a resonant frequency and then allowed to decay. The decay of the amplitude, A, of the motion of a freely decaying resonant mode

of angular resonant frequency, ω_0, can be shown to decay from some initial amplitude, A_0, as,

$$A = A_0 e^{-\frac{\phi(\omega_0)\omega_0 t}{2}}. \tag{2.14}$$

Thus the mechanical loss, ϕ can be found from measurements of A as a function of time.

2.3.2 Coating mechanical loss

When the mechanical loss of a coated sample, $\phi(\omega_0)_{\text{coated}}$, is measured, it is a combination of the loss of the substrate, $\phi(\omega_0)_{\text{substrate}}$, and the loss of the coating, $\phi(\omega_0)_{\text{coating}}$, and can be described in the following way [87],

$$\phi(\omega_0)_{\text{coated}} = \phi(\omega_0)_{\text{substrate}} + \frac{E_c}{E_s}\phi(\omega_0)_{\text{coating}}, \tag{2.15}$$

where the energy ratio E_c/E_s is the ratio of the energy stored in the coating to the energy stored in the substrate. In order to calculate the energy ratio, in a simple case of a bending bar, consider a bar of length L, width w and thickness a with a thin coating layer of thickness t. When the bar is bent into an arc as shown in Figure 2.1, the coating is stretched by ΔL and the energy stored in the coating layer is given by,

$$E_c = \frac{1}{2}k(\Delta L)^2 = \frac{1}{2}\frac{Y_c A}{L}(\Delta L)^2 \tag{2.16}$$

$$= \frac{1}{2}\frac{Y_c tw}{L}(\Delta L)^2 \tag{2.17}$$

$$= \frac{Y_c t a^2 w \theta^2}{8L}, \tag{2.18}$$

where k is the spring constant, Y_c is the Young's modulus of the coating, $A = tw$ is the cross section of the coating material and $\Delta L = a\theta/2$.

The energy stored in the bar can be calculated by firstly considering the energy stored in a thin section of the bar, where the dE is analogous to the
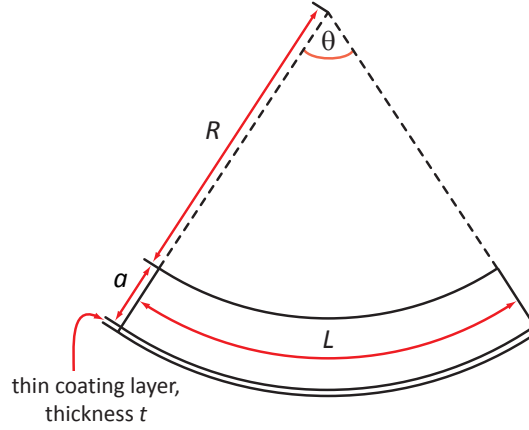
Figure 2.1: *Diagram of a bar bent into the arc of a circle*

coating energy, E_c, such that,

$$dE = \frac{1}{2}\frac{Y_\mathrm{s}w\Delta L^2}{L}dr, \tag{2.19}$$

where Y_s is the Young's modulus of the substrate and in this case $\Delta L = (r - R_0)\theta$. We will assume that the energy stored under tension in the section of the bar from R_0 to $R_0 + \frac{a}{2}$ is equal to the energy stored under compression in the section of the bar from R_0 to $R_0 - \frac{a}{2}$. Therefore the total energy stored in the bar is double the integral of dr from R_0 to $R_0 + \frac{a}{2}$,

$$E_\mathrm{s} = 2\frac{Y_\mathrm{s}w\theta^2}{2L}\int_R^{R+\frac{a}{2}}(r - R_0)^2 dr = \frac{Y_\mathrm{s}w\theta^2 a^3}{24L}. \tag{2.20}$$

Using Equations 2.18 and 2.20 give the energy ratio,

$$\frac{E_\mathrm{c}}{E_\mathrm{s}} = \frac{3Y_\mathrm{c}t}{Y_\mathrm{s}a}. \tag{2.21}$$

Finally substituting this expression for the energy ratio into Equation 2.15 and rearranging for the coating loss gives,

$$\phi(\omega_0)_\mathrm{coating} = \frac{3Y_\mathrm{c}t}{Y_\mathrm{s}a}\left(\phi(\omega_0)_\mathrm{coated} - \phi(\omega_0)_\mathrm{substrate}\right). \tag{2.22}$$

Although this is the case for a bending bar which can be directly compared to a thin coating on a cantilever, it has also been shown to be equivalent

for coated discs (or cylinders) when considering the energy dissipated in the cylinder's 'drum' mode [88].

For more complicated systems the energy ratios can also be calculated using finite element analysis, using software such as ANSYS [89]. The advantage of this is the ability to perform complex analysis when multi-layer coatings are present. In this case ANSYS treats the multi-layer coating as a composite material. This method has been previously used successfully to compute energy ratios [88, 90], and further details of this process can be found in the literature [91].

2.3.3 Mechanical loss measurements at room temperatures

The experimental setup used here to measure the mechanical loss of the coated cylinders is shown in Figure 2.2. The suspension system is contained in a vacuum tank and the mirror itself is suspended using a silk thread, to isolate the motion of the mass from its surroundings. The vacuum pressure maintained at approximately 10^{-5} mbar to eliminate gas damping [88]. The speaker and piezo are used to compensate for low and high frequency motions of the suspended mass respectively to allow the interferometer to be locked to one fringe.

The system uses a variant of a Michelson interferometer where one arm of the interferometer lies between the beam splitter and the suspended test mass, and the other is folded, being formed by the path from the beam splitter via the mirror with the piezo attached to it. The laser source used is a 5 mW helium neon (HeNe) laser. The system is designed to measure the displacement of the flat front surface of the test mass, where resonant modes of the mass are excited by use of an electrostatic actuator placed near the back face of the test mass. The excitation signal is then turned off and the 'ring down' of the resonance motion monitored using the interferometer.

Finding the expected resonant frequencies can be achieved using the finite
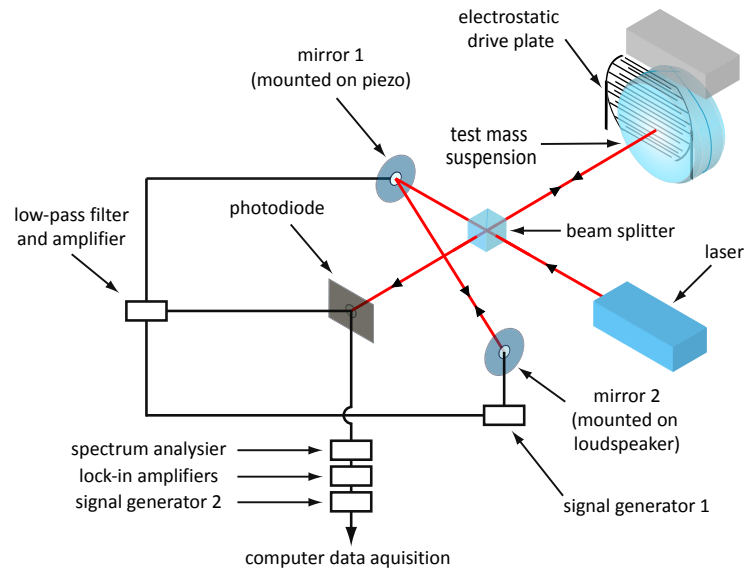
Figure 2.2: *Schematic diagram of the room temperature mechanical loss measurement experimental system, showing the optical path of the laser and relevant components, including the test mass suspended using silk thread.*
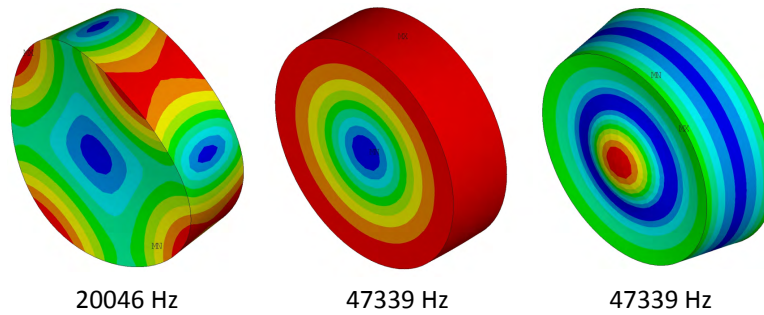
Figure 2.3: *Diagram showing a subset of the mode shapes generated by ANSYS for a 3" diameter × 1" thick silica disc, where the colour indicates the relative displacements, $U = \sqrt{x^2 + y^2 + z^2}$ when plotted in normalised, dimensionless units where the blue end of the spectrum indicates $U \doteq 0$ and red end of the spectrum indicates $U = 1$.*

element analysis software ANSYS, where models of the test masses are created and the resonant modes are calculated based on the material dimensions and properties. This is used to gain the expected resonant frequencies of the test mass, and also gives a model of the distribution of strain energy in each resonant mode. In Figure 2.3, the red areas of the test mass model show the

portions of the surface that are most deformed for a particular resonant frequency. The laser light is then targeted at this location on the test mass in order to generate the maximum output signal.
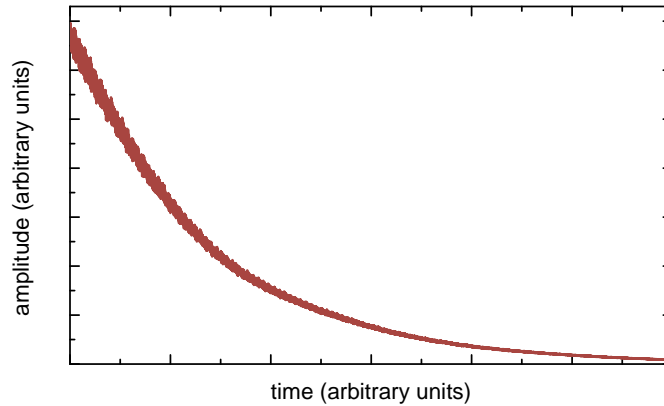
Figure 2.4: *Graph of an example 'ring down' from a sample excited at a resonant mode and then left to de-excite.*

An example of a ring down is shown in Figure 2.4. From this is it possible to produce an exponential decay fit such that it satisfies Equation 2.14 allowing the mechanical loss to be calculated, and then coating loss can be extracted using Equation 2.22. The required substrate loss, $\phi_{\text{substrate}}$, is calculated by measuring the mechanical loss of a 'control' sample, where the substrate has similar properties to the coated sample with the absence of a coating.

2.3.4 Mechanical loss measurements at cryogenic temperature

The temperature dependence of the mechanical loss of mirror coatings is also studied using samples mounted in a cryostat where losses can be measured in the temperature range from roughly 12 K to room temperature. The samples measured for this thesis were cantilevers consisting of single layer coatings applied to silicon substrates. A schematic diagram of the experimental setup in shown in Figure 2.5.
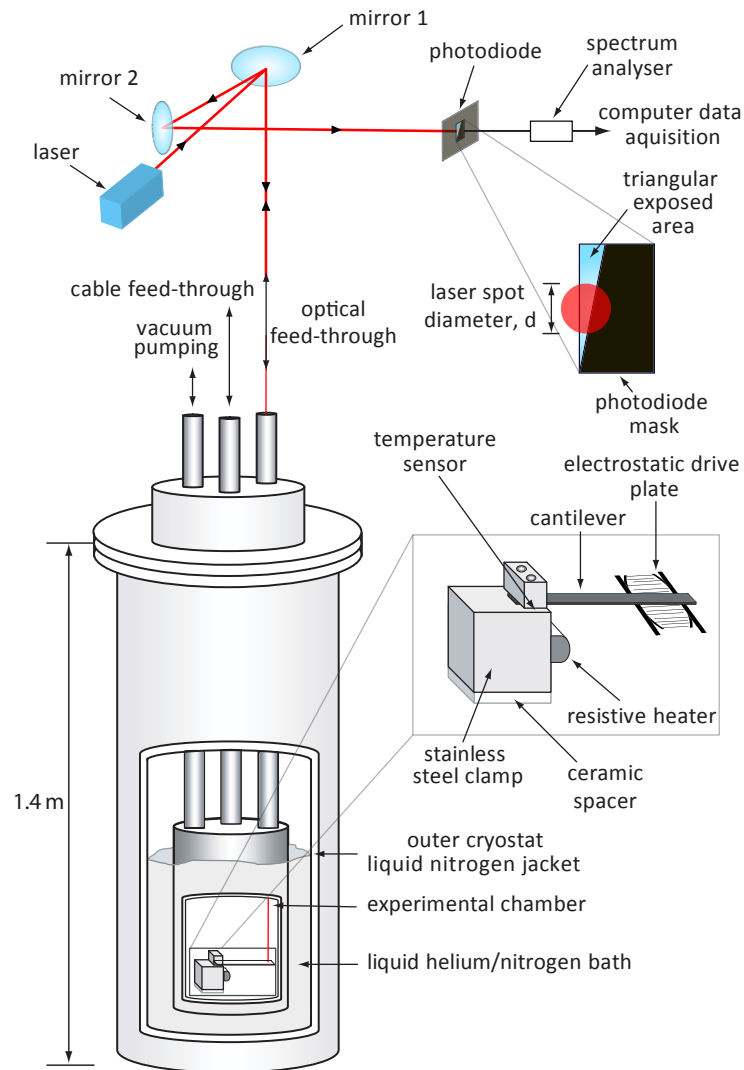
Figure 2.5: *Schematic diagram of the cryostat setup showing the optical path of the laser, highlighting the masked photodiode and clamping system for the cantilevers.*

The cantilever is held in a stainless steel clamp horizontally, and the cantilever is placed in close proximity to the the electrostatic drive plate. The clamp itself has a resistive heater attached to allow for temperature control and a silicon diode temperature sensor is mounted in the clamp directly below the cantilever. As in the case for the room temperature setup, gas damping is reduced to a negligible amount by holding the vacuum chamber at a vacuum

pressure of 1×10^{-6} mbar [90, 92]. The cryostat design allowed the vacuum chamber to be submerged in liquid helium or nitrogen to allow efficient cooling. Typical operation allowed the sample to be cooled to down to just under 12 K with average temperature fluctuations of less than 0.2 K. Measurements were taken using computing software that controls the temperature, and increases it in steps and allows the system to stabilise before taking ring downs from a series of modes.

The optical system uses a HeNe laser, similar to the room temperature setup, that is reflected down to the cantilever via an optical feedthrough, then reflected back up and subsequently reflected via mirrors 1 and 2 onto a photo-diode, as shown in Figure 2.5. The rectangular photodiode had a mask placed on top of it such that only a triangular area was exposed. The reflected laser spot moves up and down the photodiode when the cantilever is excited at a resonant frequency as it vibrates, and the result is photodiode output current proportional to the amplitude of the motion of the spot. The laser spot with diameter, D, is at least $5 \times$ larger than the widest exposed region of the exposed triangular section of the photodiode, ensuring a linear signal readout.

It can be shown that the angular frequency of the nth bending mode of a cantilever is given by [93],

$$\omega_n = (k_n L)^2 \frac{a}{2\sqrt{3}L^2} \left(\frac{Y}{\rho}\right)^{\frac{1}{2}}, \tag{2.23}$$

where a is the cantilever thickness, L is the cantilever length, Y is the Young's modulus and ρ is the density. This equation was used to predict the various resonant bending modes of the cantilever.

As with the room temperature measurements, cantilever mechanical loss can be calculated from the ring down Equation 2.14. Then the coating loss can be extracted using Equation 2.22, using an un-coated cantilever with similar properties to the measured coated cantilever to get $\phi_{\text{substrate}}$.

2.4 Investigating atomic structure and chemistry

2.4.1 Transmission electron microscopy

Over the past 80 years, materials science has been revolutionised by the creation of the electron microscope. In 1925 Louis de Broglie theorized the wave-like properties of the electron, which had a much smaller wavelength than light [94]. This wave-like nature was demonstrated by electron diffraction experiments independently carried out by Davisson and Germer, and Thompson and Reid in 1927 [95, 96]. Five years later in 1932, the term 'electron microscope' was first used in a publication by Knoll and Ruska [97] and four years after that, the first commercial transmission electron microscopes (TEMs) came onto the market. They have evolved into, arguably, the most efficient and versatile tools for the characterisation of materials.

The Rayleigh criterion for light microscopy describes the smallest resolvable distance, δ, which is related to its wavelength, λ, by:

$$\delta = \frac{0.61\lambda}{n\sin\theta},\tag{2.24}$$

where n is the refractive index of the specimen material and θ is the collection angle of the magnifying lens. This gives light microscopes a resolution of, at best, around 300 nm.

Electron microscopes were first developed with the aim of improving upon the resolution of light microscopes. The wavelength, λ_e, of the electrons used in a TEM can be calculated by firstly relating the wavelength of electrons to their momentum, p, using,

$$\lambda_e = \frac{h}{p} = \frac{h}{(2m_0 eV)^{\frac{1}{2}}},\tag{2.25}$$

where h is Planck's constant, and p can be expanded to take into account the accelerating voltage, V of the TEM where m_0 is the rest mass of the electron

and e is the electron charge. Equation 2.25 shows that as the accelerating voltage increases, the wavelength of the electrons decrease. Modern TEMs operate in the region of 100-300 keV, which means that electrons are being accelerated to around half the speed of light. Therefore, to accurately measure λ_e it is necessary to account for relativistic effects and Equation 2.25 becomes [98],

$$\lambda_{e,rel} = \frac{h}{\left(2m_0 eV \left(1 + \frac{eV}{2m_0 c^2}\right)\right)^{\frac{1}{2}}}, \tag{2.26}$$

where $\lambda_{e,rel}$ is now the relativistically corrected electron wavelength and c is the speed of light. A TEM with accelerating voltages of 200 keV, such as the Tecnai T20 used for this research, will therefore operate at a wavelength of 2.51 pm, theoretically giving the user capability of reaching greater than atomic resolution [98]. Unfortunately other limitations on the TEM, such as lens aberrations and issues with mechanical and electrical stability, mean that such picometre resolution cannot be reached [98]. However, there has been huge progress in the development of aberration correction for TEMs in the last 15 years, and it has been possible to increase the maximum resolution to sub-angstrom levels. Nevertheless, although viewing individual columns of crystals in atoms is possible, resolution is not the only important issue when developing new TEMs. It is the interaction of electrons with matter that is driving the creation of new electron microscopes and we can learn a far greater amount from these interactions than just simply producing a magnified image.

2.4.2 Electron beam interactions with materials

When a high keV electron beam hits a sample and interacts with the material a number of signals are produced [98]. The type of signals that are produced and their properties, some of which are shown in Figure 2.6, vary depending on the microscope setup and materials being studied [98].

The direct beam is formed from electrons that pass undeviated through the
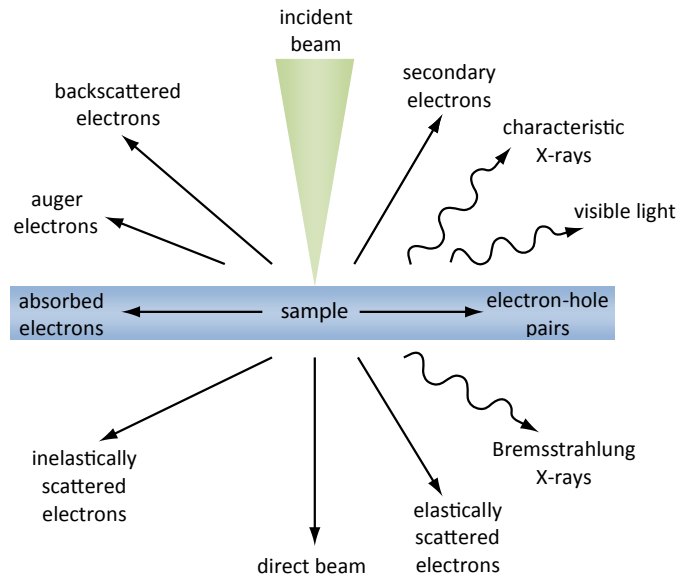
Figure 2.6: *Diagram showing the signals produced when a high keV electron beam impacts a sample material*

material. For the other signals produced, there are two basic interaction processes that govern their production, which are elastic and inelastic scattering of the incident electrons.

2.4.2.1 Elastic electron scattering

Elastic electron scattering describes the process occurring when electrons interact with the sample and lose very little of their initial energy. If we consider the interaction with one atom, there are three mechanisms that describe the effect on an incoming *negatively charged* electron as it experiences an attraction towards the *positively charged* nucleus, as shown in Figure 2.7.

Incoming electrons interacting with electrons in the outer regions of the electron cloud generally scatter with a low scattering angle, θ. Incoming electrons that penetrate the electron cloud will be attracted to the nucleus and subsequently experience a higher scattering angle. Finally, incoming electrons that pass close enough to the nucleus may experience complete backscattering, where $\theta = 180\,^\circ$ [98].
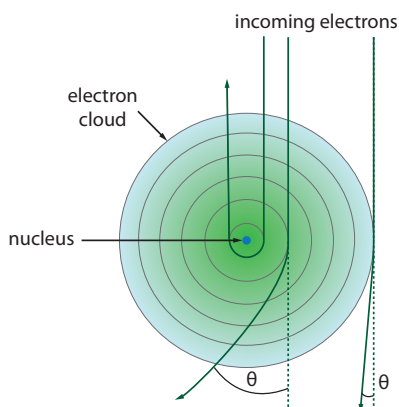
Figure 2.7: *Schematic diagram showing the various possibilities of high keV electron interaction with an atom*

Atomic scattering factor A useful way of describing electron scattering is through the atomic scattering factor, f, which describes how the electron scattering intensity varies with θ. It can be defined by [98],

$$f(\theta) = \frac{\left(1 + \frac{E_0}{m_0 c^2}\right)}{8\pi^2 a_0} \left(\frac{\lambda}{\sin\frac{\theta}{2}}\right)^2 (Z - f_x), \qquad (2.27)$$

where a_0 is the Bohr radius, E_0 is the energy of the incident electron beam with wavelength, λ, m_0 is the mass of the electron, Z is the atomic number of the scattering atom and f_x is the scattering factor, most commonly obtained from X-ray diffraction studies [99]. There have been many studies to determine accurate scattering factors such as Doyle and Turner [99], Konnet and Karle [100] and Peng *et al.* [101] for various materials.

Kirkland also produced a version of the scattering factor which depends on several computationally derived fitting parameters, called Kirkland fitting parameters, for each element [102]. Kirkland's version of the scattering factor fits the scattering intensities as a product of three Gaussian and three Lorentzian functions, which allows for very accurate fitting of the measured scattering (or diffraction) data. Kirkland's version of the scattering factor is used for the Reduced Density Function analysis, discussed in more detail in Section 2.4.7.2.

Bragg scattering The simplest way to consider scattering from multiple atoms in crystalline materials is through Bragg scattering [98]. Electrons incident on parallel crystallographic planes, a distance d apart, will produce constructive interference at an angle θ from the plane when they satisfy the Bragg Law [103],

$$n\lambda = 2d\sin\theta, \tag{2.28}$$

where n is the integral number of wavelengths λ. The Bragg law is therefore a result of the periodicity of a crystal lattice and is important when interpreting diffraction patterns. When atomic planes are closer together they produce larger scattering angles, and inter-planar spacings can be calculated since λ is known and θ can be measured [98, 103]. It is also import to note that scattering from amorphous materials also shows characteristic structures related to their short range order, as will be discussed in more detail in Section 2.4.7.

2.4.2.2 Inelastic electron scattering

Inelastic electron scattering occurs when incident electrons lose some or all of their initial energy from interacting with the sample. Many of the incident beam electrons will lose energy through a variety of processes, thus generating the electron energy loss spectrum, and subsequently also results in the production of Auger electron, X-rays and visible light [98]. Some of the processes resulting in electron energy loss are phonon and plasmon scattering, single electron excitations and direct radiation loss [104].

Phonon and plasmon scattering Atoms sitting in any material will have thermal energy causing them to oscillate around their mean atomic position. Incident high energy electrons can gain or lose energy by the transfer of this thermal energy to or from the atoms by a small amount (of the order of kT) because of this thermal energy [104]. This energy transfer is due to the creation or annihilation of phonons, and although the energy is small, around 1/40 eV,

the incident electrons can be scattered through large scattering angles [98, 104]. This creates a underlying background of scattered electrons and, in a crystalline material, describes the diffuse electron scattering between diffraction spots [98]. Plasmons describe the collective oscillations of valence electrons in a material. Incident high keV electrons can interact with the valence electrons displacing them from their equilibrium for a short period of time. The resulting energy transfer will cause the incident electrons to lose energy (of the order 15 eV), being denoted as plasmon loss electrons. This is the most common type of inelastic scattering. The amount of energy lost depends on the 'free' electron density of the material and is of the order of 5 - 25 eV [98] and results in a prominent feature of electron energy loss spectra, see Section 2.4.6.2.

Single electron scattering   When the incident high keV electrons hit the sample they can also transfer energy to a single electron. In such an inelastic interaction, this can cause an electron in the atom to move into a higher energy state or even to be ejected altogether if enough energy is transferred. After the interaction the incident electron will lose energy equal to the amount it transferred to the core-electron, and this is known as a core loss interaction. This is important for electron energy loss spectroscopy (see Section 2.4.6.2), as the characteristic energy loss can be used to identify the atomic species [104], and additionally the amount of such interactions in an energy loss spectrum can be used to quantify elemental concentrations in a material. The shape of such features in an energy loss spectrum is ideally a sharp edge, above which the interaction can happen, and below which insufficient energy is available for the transition. In practice, however, the shape of such edges is complex depending on the density of unoccupied states for the core electron to be promoted into, and this can be strongly affected by bonding, making energy loss spectroscopy also highly sensitive to chemical bonding changes in solids.

Direct radiation loss Deceleration of the beam electrons will also occur as they travel through the sample, which will cause them to emit X-rays. X-rays produced in this manner give rise a background radiation called bremsstrahlung, which is a continuous spectrum of X-rays with a maximum energy limited to the energy of the incident beam electrons. The process that describes single electron scattering can be extended to consider what happens to the ionised atom, where the atom is left in an excited state as the atom is missing an inner shell electron. The atom can reach equilibrium by taking an electron from a higher energy shell and this process generates an X-ray with a characteristic frequency. Characteristic X-rays can then be used, as in the case with single electron scattering, to identify atomic species [98].

2.4.3 The transmission electron microscope

2.4.3.1 Electron sources

There are two main types of electron sources available for TEMs. These are thermionic sources and field emission guns (FEGs).

Thermionic emission occurs when any material is heated to a sufficient temperature that you overcome the natural barrier that prevents electrons from being emitted. Richardson's law summarises thermionic emission and relates the current density of the source, J and the operating temperature, T, via the expression [98]:

$$J = AT^2 e^{-\frac{\Phi}{kT}}, \tag{2.29}$$

where A is the Richardson constant, which depends on the material used, Φ is the work function that describes the natural emission barrier and k is Boltzmann's constant. Equation 2.29 shows that in order to generate enough electrons to produce an electron beam, the temperature, T, must be sufficiently high to overcome the work function, Φ. The work function is normally around a few keV and this requires materials that can withstand extremely large temperatures without melting or vaporizing. The two most commonly
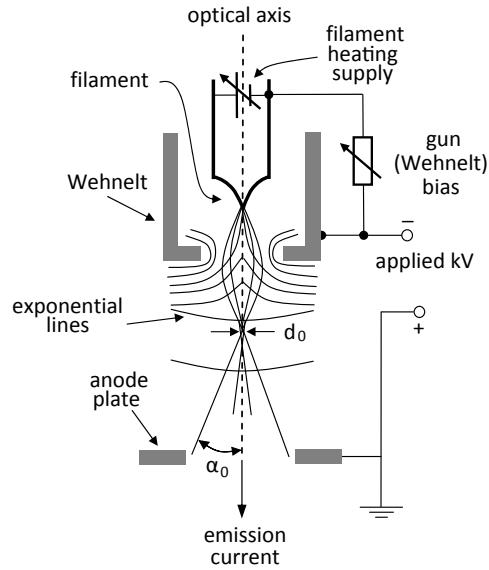
Figure 2.8: *Schematic diagram of a thermionic electron gun.*

used materials are tungsten, which has a high melting point and LaB_6, which has a low work function.

The filament acts as the cathode with the addition of the Wehnelt [98], an electrode in the electron gun assembly, which limits the emission to the tip of the filament. The Wehnelt has a small negative bias with respect to the filament; the electrons coming from the filament see the negative field and are converged to a point called the crossover, d_0. The electrons leave the cathode with a negative potential of 100 kV and are then accelerated to the earth anode acquiring an energy of 100 keV.

Field emission depends on the electric field, E, and the fact that it increases considerably with sharp points or tips,

$$E = \frac{V}{r}, \tag{2.30}$$

where V is the voltage applied to a spherical point of radius r.

The emission of electrons from field emission guns (FEGs) come in two different types: cold field emission guns and Schottky guns [98]. Two anodes negatively bias the cold field emission gun filament. The first anode provides
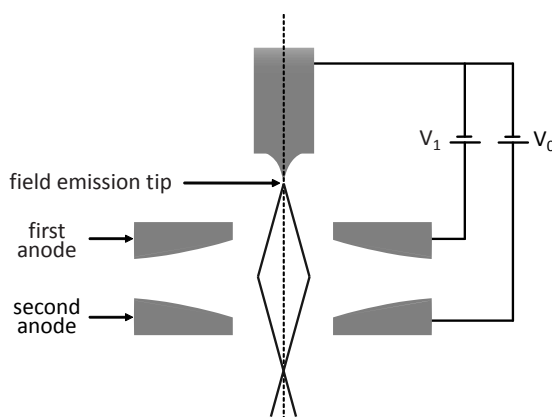
Figure 2.9: *Schematic diagram of a field emission electron gun.*

the extraction voltage from the tip and the second accelerates the electrons to a desired voltage. The tip has to be held under extremely high vacuum and be completely free from contaminants and oxides. Thermally assisted field emission guns, or Schottky guns, overcome the need to hold the instrument in such a high vacuum. In that case a coating is applied to the gun tip typically using a material such as ZrO_2 with the purpose of reducing the work function. The size of FEGs are in the order of 100 times smaller than a typical LaB_6 thermionic gun, resulting in a much higher brightness from the FEGs. The FEGs also have a smaller more coherent beam than thermionic guns and are therefore preferred for precision microscopy.

2.4.3.2   Components of the TEM column

The TEM column consists of a series of magnetic lenses and apertures that work to control the direction and rate of electrons travelling to the sample and to the detection instruments, defining the operating modes of the microscope.

Magnetic electron lenses are in place to focus the electrons as required. They normally consist of two polepieces separated by a gap, which are made from cylindrically symmetric soft iron material with a hole drilled through the centre where the beam electrons pass through. The polepieces are surrounded by coils of copper wire and when an electric current is passed through the coils

a magnetic field is generated in the polepiece hole changing the direction the electrons travel down the column. Varying the electric current in the coils will change the strength of the magnetic field, allowing control over the path the electron will take and the location of beam focal point [98].

Apertures in the column allow control over the collection angle, β, of the lens, meaning that electrons at travelling at certain angles away from the optical axis of the beam are blocked by the apertures. They are used in a number of different places either above, inside or below the plane of the lenses with varying sizes, and are generally made of platinum or molybdenum [98].

The main components of the column are the condenser lens system, objective lens system, intermediate lenses and projector lenses, as shown in Figure 2.10. Working down the column, electrons from the gun enter the condenser lens system, which controls the amount of illumination given to the sample. The first condenser lens demagnifies the gun crossover while the second condenser lens produces a parallel beam that is then passed through the condenser aperture. The condenser aperture can vary between 20 μm to 200 μm allowing further control over the illumination, where a smaller aperture gives a beam with greater coherence and therefore lower current density. The specimen plane lies between the pole-pieces of the objective lens system. The objective lens is the primary imaging lens and has a magnification of about 50 to 100 times. Due to the placement of the specimen between the pole-pieces of objective lens, the specimen can feel a magnetic field greater than 1 Tesla, allowing for magnetic investigation of the specimen, which can be manipulated by tilting the sample. A series of intermediate and projector lenses further magnify the image and project it onto a phosphor viewing screen and to the detectors.

2.4.3.3 Detecting instruments

Modern TEMs will almost certainly record images using a CCD placed above or below the phosphor viewing plate. The electrons hit against a scintillator

electron source

C1 aperture

C1 lens

C2 lens

C2 aperture

upper objective lens

sample

lower objective lens

objective aperture

SAD aperture

intermediate lens

projector lenses

retractable soft imaging system
(SIS) CCD

retractable viewing screen

entrance apertures

alignment
coils

quadrupole lenses

magnetic
prism

slit

sextupole lenses

CCD

Gatan Image System (GIF)

Figure 2.10: *Schematic of relative positions of the lenses, apertures and detection instruments on the Tecnai T20 transmission electron microscope*

plate converting the electron image into a light image, which is in turn converted by the CCD into a digital image. Many TEMs still include a traditional photographic plate, for taking images that have a greater resolution than their CCD counter parts. CCDs and photographic plates can be used for recording bright and dark field images, as well as diffraction patterns. There can also be instruments for spectroscopic imaging, such as the electro dispersive X-ray (EDX) spectrometer used for X-ray spectroscopy and electron energy loss spectroscopy (EELS) detector, both allowing for elemental analysis of the specimen.

2.4.4   FEI Tecnai T20

The Kelvin Nanocharacterisation Centre, located in the School of Physics and Astronomy in the University of Glasgow currently has three TEMs. The Philips CM20 is specially adapted for magnetic interaction studies and the FEI Tecnai F20 used for high resolution imaging and has scanning transmission electron microscopy capabilities. Here we will concentrate on the FEI Tecnai T20 (T20 for short) as this is the TEM used to collect the data for the research presented in this thesis.

The T20 transmission electron microscope is operated as a conventional TEM and has been used to carry out the atomic structure investigations on coating materials described in this thesis. Figure 2.10 shows a schematic diagram of the current setup of the T20. It uses a 200 kV LaB_6 thermionic electron source housed at the top of the TEM column and employs a two condenser lens system to allow for accurate control of the electron beam. The T20 is fitted with a side mounted Soft Imaging System (SIS) Megaview III CCD camera [105] which has high dynamic range and high sensitivity, and is used for the collection of the diffraction patterns used in this research. There is also a Gatan Image Filter (GIF) CCD [106] which has energy filtering imaging capabilities and the ability to record EEL spectra through the use of a slit

and series of quadrupole and sextupole lenses that control the dispersion, and also energy filter the beam. The GIF CCD was used to take the EEL spectra presented in this thesis.

2.4.5 Sample preparation

All of the mirror coating samples used for measurements in the TEM were made using the well established cross-section method [107] which allows the generation of thin (down to 10 nm) electron transparent regions of coating material. The coating materials investigated in this thesis are generally several hundred nm thick and deposited using argon ion-beam sputtering onto a high quality substrate of amorphous fused SiO_2 (silica) or pure crystalline silicon. These coating 'witness' samples are disks that measure 1" in diameter by 0.25" thick. These are then processed into cross-section samples suitable for TEM studies as described below.
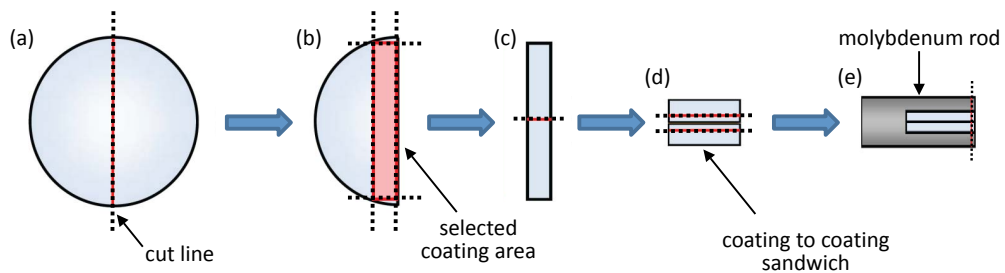
Figure 2.11: *Schematic diagrams of the sample preparation process from (a) having an initial 1" × 1/4" coated silica disc and cutting and thinning an area of interest (b) - (d), to encapsulation (e)*

Figure 2.11 (a) - (c) shows the process of taking the witness sample and cutting out an area of coating with substrate material using diamond circular saw. A 'sandwich' of substrate-coating to coating-substrate is then produced and thinned using a hand grinder until it measures around 2 mm wide by 0.5 μm thick (Figure 2.11 (d)). The next stage is encapsulation where the sandwich section is glued together using a thin layer of epoxy resin and put into a slot cut

out of a molybdenum rod again using a small amount of epoxy resin (Figure 2.11 (f)), which is then all held together by slotting this into either a brass or titanium tube. The resulting capsule is put into an oven for a minimum of 1 hour at 130 °C to cure the epoxy resin. As most of the investigated coatings are heat-treated during the manufacturing process at a temperatures higher than this, in most cases for 24 hours, it is assumed that any changes to the coating properties, including the atomic structure, are negligible. Where the coating material has undergone heat treatment during its manufacturing at a lower temperature than the 130 °C used to cure the epoxy, a longer time in the oven at lower temperature can be used to cure the epoxy or else super glue can be used. However issues with the amount of free carbon in super glue can cause contamination in the TEM and the build up of carbon on the area being studied, and the use of super glue is avoided where possible.
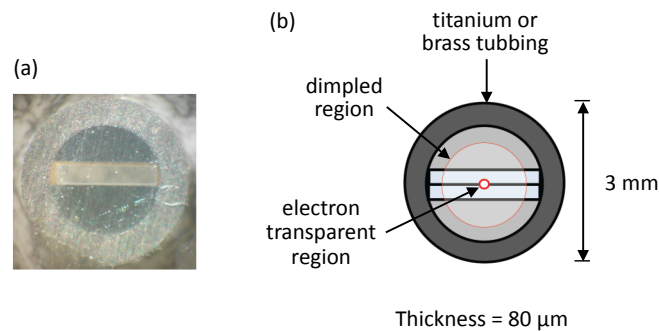
Figure 2.12: *(a) image of an example TEM cross section sample. (b) a schematic representation of the final TEM sample*

After the capsule is cured, it is cut using a diamond circular saw into individual disc sections. These are around 500μm wide and a typical encapsulated sample will produce around 10 discs. These discs are then thinned to around 80 - 100 μm using a hand grinder. Figure 2.12 (a) shows a photo taken of a typical disc at this stage. A Gatan [106] Dimpler, is used to grind a dimple at the center of disc using a rotating copper or steel wheel with diamond paste, and then polished with a felt wheel and high grade diamond paste. The dim-

pler machine accurately thins the center of the disc to around 20 μm. The final stage uses a Gatan Precision Ion Polishing System (PIPS) to mill the center and create an electron transparent region of thickness ~ 10 nm. The PIPS uses dual argon ion beams that mills both sides of the disc simultaneously. For the coating TEM samples, these beams are offset from the plane of each side of the disc at $4°$ and a beam energy of up to 4 kV is used until a small hole is created at the center, around which is the electron transparent region (see Figure 2.12 (b)). To finish the TEM sample the PIPS can be set to produce a low 0.5 kV ion beam to polish and produce a sample with the maximum amount of electron transparent regions. For the majority of the TEM samples prepared in this way, the PIPS was operated using a 'cold stage', meaning the sample was cooled with liquid nitrogen to around 100 K, which avoids any potential overheating of the sample.

Throughout the sample preparation process the sample is kept clean using common laboratory grade solvents: acetone, chloroform, ethanol and inhibisol.

2.4.6   TEM measurement techniques

2.4.6.1   Imaging and diffraction

An image in the TEM is created at the image plane, as shown in Figure 2.13 (a). In Conventional TEM (CTEM), all scattered and direct electrons that leave the sample are used to create the image, where there is no objective aperture in place. However due to the presence of the scattered electrons image contrast can be low. When viewing in bright field mode direct electrons create the image and electrons are gathered only from the central diffraction spot. By selecting only these electrons using the objective aperture, as shown in Figure 2.13 (a), a greater image contrast can be achieved. In dark field imaging the scattered electrons form the image, and one way of achieving this is shown in Figure 2.13 (b) so that the incoming electron beam is offset at some angle, so that the diffracted electrons travel through the objective aperture to form

the image. In order to study structure down at the nanometer scale, there is an imaging mode known High Resolution Transmission Electron Microscopy (HRTEM), which uses the same principles of bright field imaging, optimised using careful calibration to obtain nanometer resolution at high magnification.

In diffraction mode the diffraction pattern is created in the back focal plane, as shown Figure 2.13 (a). Diffraction patterns formed from the diffracted beams due to electron scattering can be observed in the viewing screen by taking out the objective aperture and altering the post-specimen lenses, so that the back focal plane becomes the image plane.
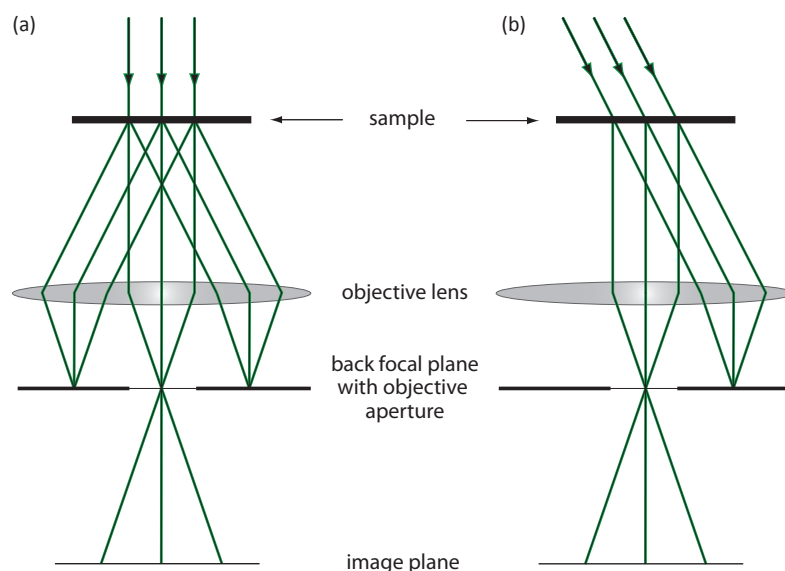
Figure 2.13: *Ray diagrams showing (a) the creation of a diffraction pattern in the back focal plane and a bright field image in the focal plane, and (b) dark field image present in the image plane by offsetting the angle of the incoming electron beam to the sample*

Bright and dark field images were used to examine the coating material. Dark field images were particularly useful for looking at samples where crystallisation had occurred, where it is possible to examine electrons Bragg scattered from crystal planes to measure their size and shape. HRTEM was also used in some cases to search for nanocrystals, that do not cause enough electron scatter to be easily identified in diffraction mode.

Convergent beam electron diffraction When there is a need to collect diffraction data from a small volume of the sample, convergent beam electron diffraction (CBED) can be used. In this method, rather than having parallel illumination on the sample, which is limited in collection area by the smallest selected area aperture, the condenser aperture and lenses are used to converge the beam onto the sample surface. Figure 2.14 shows the difference between parallel and convergent illumination on the sample. As implied from Figure 2.14 (b), conical electron beams are produced when leaving the sample and CBED patterns produce diffraction discs, as opposed to the sharp diffraction spots present under parallel illumination. The diameter of these discs are directly related to the convergence semi-angle angle, α, where a larger α will produce large overlapping discs and a smaller α will produce individually resolved discs, becoming similar to parallel illumination diffraction spots.
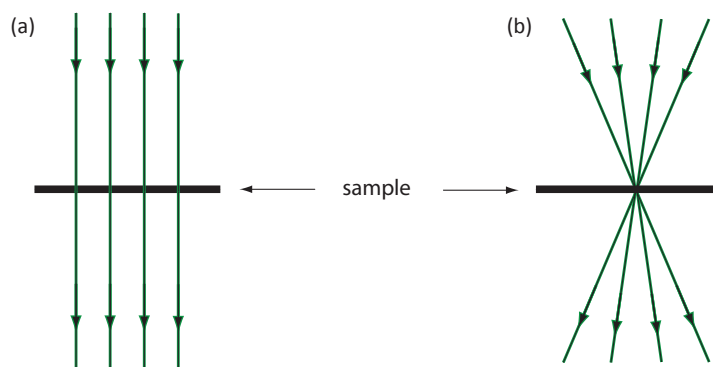
Figure 2.14: *Schematic diagram showing the electron beam path for (a) conventional parallel illumination and (b) convergent beam illumination*

CBED with a small $\alpha = 1.89\,\mathrm{mrad}$ was the method used to take all of the diffraction data for the amorphous mirror coating material, as it allowed greater control over selected areas of the sample whilst keeping the illumination as parallel as possible.

2.4.6.2   Electron energy loss spectroscopy

Electron energy loss spectroscopy (EELS) is a method of analysing the spectrum of elastic and inelastic scattered electrons from the sample material, see the previous Section 2.4.2. EEL spectra provide a means of studying compositional and chemical properties of the sample material that complements TEM imaging and diffraction [108].
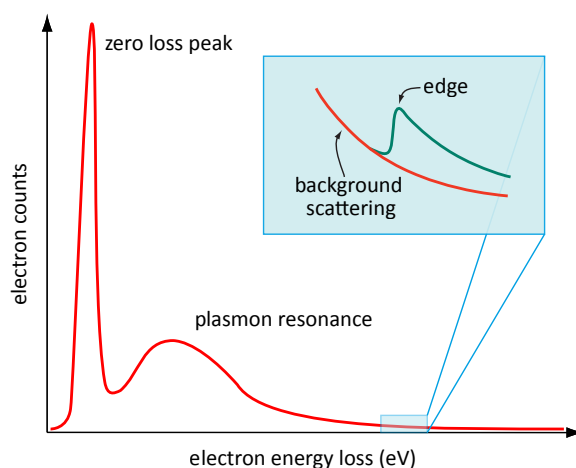
Figure 2.15: *Schematic diagram of an idealised EELS spectrum, highlighting the an example onset of an EELS edge resulting from the energy loss electrons of a specific atomic species in the sample.*

An idealised EELS spectrum as shown in Figure 2.15, represents the general spectrum that the EELS spectrometer can detect. The zero loss peak is the most prominent feature in thin samples, where electrons which do not lose beam energy scatter within a narrow cone straight through the sample. Towards increasing energies in the energy loss spectrum, the plasmon resonance peak follows, formed from inelastic plasmon scattering through wide angles as described in Section 2.4.2. The single electron scattering process, described in Section 2.4.2, produces characteristic 'edges' as shown in Figure 2.15, and are features that lie above the scattering background. An edge will decay towards a background, that will include weaker interactions as the energy loss increases. The shape of the EELS edges will change with the atomic species where heavier

elements with more electrons produces more complex interactions.

EELS has been shown to be an excellent tool for studying the composition of materials at high spatial resolution [109]. This can be carried out by firstly measuring a set energy loss window above the background after an EELS edge, where a background model is fitted to the energies just below the edge, then subtracted from it, and the resulting energy loss window is quantified through numerical integration. When a suitable cross-section is studied for a well known sample, or standard, comparison with an unknown material can yield ratios of one atomic species to the other, giving the stoichiometry of the material. This process can be described mathematically as [110],

$$\frac{N_{\mathrm{A}}}{N_{\mathrm{B}}} = \frac{I_{\mathrm{A}}(\beta, \Delta)}{I_{\mathrm{B}}(\beta, \Delta)} \frac{\sigma_{\mathrm{B}}(\beta, \Delta)}{\sigma_{\mathrm{A}}(\beta, \Delta)}, \tag{2.31}$$

where N_x is the number of atoms per unit area, I_x is the energy loss intensity, σ_x is the partial scattering cross-section, β is the collection angle, Δ is the EELS edge integration window (or area) and $x = $ A or B atomic species. The term $\sigma_{\mathrm{B}}(\beta, \Delta)/\sigma_{\mathrm{A}}(\beta, \Delta)$ can be found using a known cross-sections of the material or standards with well known A - B compositions.

EELS was used in the research presented in this thesis to calculate the ratio of tantalum to oxygen present and also titanium doping levels in the mirror coating samples. The EELS edges analysed are shown in Table 2.1 below.

Atom	Edge	Energy loss (eV)
Tantalum	$N_{4,5}$	229
Titanium	L	456
Oxygen	K	532

Table 2.1: *Coating information for samples throughout the report*

The tantalum $N_{4,5}$ edge does not have a well known cross-section and was therefore experimentally measured from a known standard of $LiTaO_3$. To do this a TEM sample was prepared from a perovskite $LiTaO_3$ [111] substrate,

which was used as a standard on the assumption that an ideal Ta:O ratio of 1:3 was present in the sample. EELS data was acquired under the same conditions Ta_2O_5 coatings for the $LiTaO_2$ sample, and a previously calculated oxygen K cross-section was then used to calculate the tantalum $N_{4,5}$ cross section.

2.4.7 Amorphous materials

The majority of the mirror coatings studied for this research are amorphous in nature. The term amorphous meaning 'without form' describes disordered materials, where none of the periodic long range order of crystalline materials is present. However, these materials are not completely without form, they have structure in the range of $\lesssim 10$ Å [112]. It is possible to characterise this short range order, and common techniques such as neutron or X-ray diffraction are used regularly to investigate amorphous materials [113]. More recently, transmission electron microscopy has been used to study these materials [112]. The advantage of using electrons over neutrons or X-rays is that electrons can be focused to collect data from selected nanometer areas and have relatively large scattering cross section, compared to the millimeter scale and relatively small scattering cross sections of neutrons and X-rays [112].

The study of the amorphous mirror coatings presented in this thesis uses techniques developed to probe the short range order of amorphous materials using transmission electron microscopy.

2.4.7.1 The reduced density function

The typical way to describe an amorphous structure is through the use of statistical distribution functions [113], which describe the probability distribution of finding atoms at a particular distance, say r, from a central point. There are a number of different distribution functions in commonly used, but in this thesis the reduced radial distribution function or reduced density function (RDF) is used, denoted as $G(r)$.

Diffraction data collected from the TEM, when radially averaged from a central point, can be viewed as an intensity distribution in scattering (q) space. This intensity distribution can be expressed statistically as,

$$I(q) = N\langle f\rangle^2 + 4\pi N\langle f^2\rangle \int_0^\infty [g(r) - \rho_0]\frac{r}{q}\sin(qr)dr, \qquad (2.32)$$

where N is the number of atoms, r is the distance from a central atom, f is the scattering factor of the atoms,

$$q = \frac{4\pi(\sin\theta)}{\lambda}, \qquad (2.33)$$

$$N = \sum_i N_i, \quad \text{for atom type i}, \qquad (2.34)$$

$$\langle f\rangle^2 = \frac{\left(\sum_i N_i f_i\right)^2}{N^2}, \qquad (2.35)$$

$$\langle f^2\rangle = \frac{\sum_i N_i f_i^2}{N} \qquad (2.36)$$

$$\rho_0 = \sum_i \rho_i, \qquad (2.37)$$

and $g(r)$ is the pair distribution function. To further explain $g(r)$, firstly let $g^{(n)}(\mathbf{r}_1, \mathbf{r}_2, \ldots, \mathbf{r}_n)$ represent the density distribution of n atoms. Then a distribution of one atom $g^{(1)}(\mathbf{r})$ is the probability density of finding an atom at a location $\mathbf{r}$ and $g^{(n)}(\mathbf{r}_1, \mathbf{r}_2, \ldots, \mathbf{r}_n)$ describes the probability density of finding n atoms at $\mathbf{r}_1, \mathbf{r}_2, \ldots, \mathbf{r}_n$ simultaneously. Therefore it follows that the two atom (or pair distribution), $g^{(2)}(\mathbf{r}_1, \mathbf{r}_2)$, commonly denoted as $g(r)$, describes the probability of finding atoms at $\mathbf{r}_1$ and $\mathbf{r}_2$ simultaneously, and r ($r = |\mathbf{r}_1 - \mathbf{r}_2|$) denotes the distance between the two atom locations in a homogenous and isotropic system.

To compute the RDF, $G(r)$, it is necessary to first define the reduced intensity function, $\varphi(q)$,

$$\varphi(q) = \left[\frac{I(q) - N\langle f^2\rangle}{N\langle f\rangle^2}\right]q. \qquad (2.38)$$

This allows us to extract the pair distribution function $g(r)$ from the intensity profile. The (RDF) is then defined as,

$$G(r) = 4\pi r \left[g(r) - \rho_0\right] = \int_0^\infty \varphi(q) \sin(qr) dq. \qquad (2.39)$$

From the above process, it has been shown that the formation of the RDF, $G(r)$, can be made simply from the Fourier sine transform of $\varphi(q)$ calculated from $I(q)$. More generally, the RDF is a statistical representation of where atoms sit with regards to a central atom.

It should be noted that historically, the radial distribution function $J(r)$ is more commonly used in the literature, especially within the neutron and X-ray diffraction community. $J(r)$ predates the RDF and is different in that $J(r) = r(G(r) + 4\pi r\rho_0)$. Reviews of the different methods of displaying distribution functions can be found in the literature, for example [114].

2.4.7.2 Experimental method for RDFs and atomic modelling

TEM calibration The most important step in the experimental procedure is to ensure that the TEM is calibrated well. The intensity profile generated from the diffraction data is $I(q)$, i.e., a function of scattering space, q. The term δq is a measure of the pixel size that has to be carefully measured as it will directly affect $I(q)$ and therefore the end results in the RDF. In order to translate the pixel size into δq a well known Si crystalline standard is used, and diffraction patterns are taken under the same conditions used when taking data from the amorphous mirror coatings. Condenser, diffraction and objective astigmatism is also corrected at this stage, in order to ensure minimal distortions to the diffraction patterns.

From Figure 2.16 the labelled Bragg scattered diffraction spots have been Miller indexed, which is a standard way of identifying the diffraction spots using Cartesian co-ordinates (lmn). Silicon has a diamond cubic crystal structure and it can be shown that the distances between two adjacent diffraction spots are,

$$r_1 = \frac{a}{\sqrt{l^2 + m^2 + n^2}}, \qquad (2.40)$$
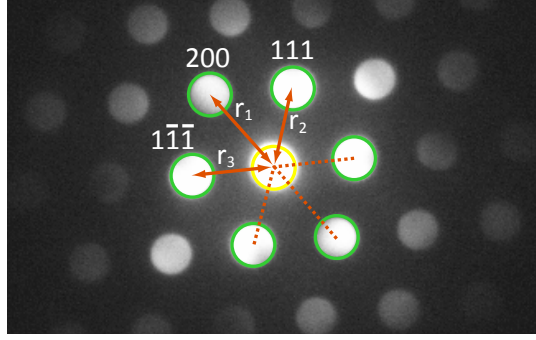
Figure 2.16: *Diffraction pattern of a Si cross section collected at a convergence semi-angle of $\alpha = 1.89$ mrad showing indexed diffraction spots and labelling the distances from their centre to the central diffraction spot*

where a is the lattice parameter. In this case the distances between the indexed diffraction spots in the Si diffraction pattern to the central diffraction spot, labelled as r_1, r_2, r_3 in Figure 2.16 are,

$$r_1 = \frac{a}{2}, \qquad r_2 = r_3 = \frac{a}{\sqrt{3}}, \tag{2.41}$$

where $a = 5.431$ nm, the lattice parameter of Si. A distance $r = 2\pi/q$ from the central spot in q space, and therefore the difference in q, Δq, between two diffraction spots will be $\Delta q = 2\pi/d$, for the silicon crystal structure. Therefore it is possible to calculate the pixel size, δq, in terms of q,

$$\delta q = \frac{\Delta q}{n}, \tag{2.42}$$

where n is the number of pixels in the CCD between the diffraction spots. Every data collection session on the TEM started by carrying out this calibration procedure on a standard Si sample before changing to a coating sample, carefully keeping the calibration settings the same.

Data collection and processing   Diffraction patterns are collected from the coating layer and are recorded with a convergence semi-angle of $\alpha = 1.89$ mrad, and spot size full width half maximum of 80 nm. Figure 2.17 (a) shows a bright field image of a typical single layer Ta_2O_5 mirror coating, where the

dark region is the Ta_2O_5 layer. The diffraction pattern data was collected from suitably thin areas of the sample that were around 10 - 20 nm thick, which reduces effects from multiple electron scattering to a negligible amount and avoids the need to energy filter the data [112]. Figure 2.17 (b) shows a typical diffraction pattern that was collected solely from the Ta_2O_5 layer. The radially averaged intensity profile of the diffraction pattern is then used as the raw data for calculating the reduced scattering intensities and RDF. Figure 2.17(c) shows the radial averaging process, where the unwanted effects from the pointer are masked before the radial average is taken.
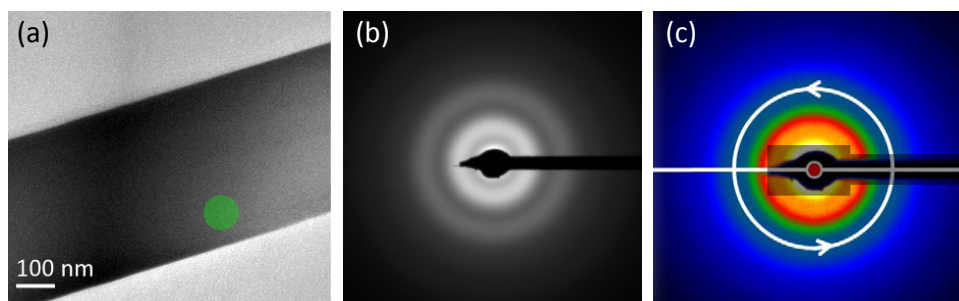
Figure 2.17: *Data collected from the TEM of: (a) a bright field image of a Ta_2O_5 coating on a silica substrate where the dark region in the Ta_2O_5 coating with a green highlighted area where the beam is focused to collect data solely from the coating material, (b) the resulting amorphous diffraction pattern of the Ta_2O_5 coating with characteristic diffuse discs, (c) a representation of the radial averaging program that finds the centre of the diffraction pattern and then radially averages the data, with masks applied over the pointer to exclude it from the radial average.*

The resulting intensity profile, $I(q)$, from the Ta_2O_5 layer is shown in Figure 2.18. In order to obtain the reduced intensity distribution $\varphi(q)$ defined in Equation 2.38, a fitting curve to $I(q)$ is first obtained by expressing $N\langle f^2 \rangle$ as,

$$N\langle f(q)^2 \rangle + I(q_{max}) - N\langle f(q_{max})^2 \rangle, \tag{2.43}$$

where we choose the maximum q value in the data that is not noisy, q_{max}, that lies on the $I(q)$ data curve. In this way, N can be adjusted so that the fitting

curve lies along $I(q)$ at high q until the maximum, q_{max}.
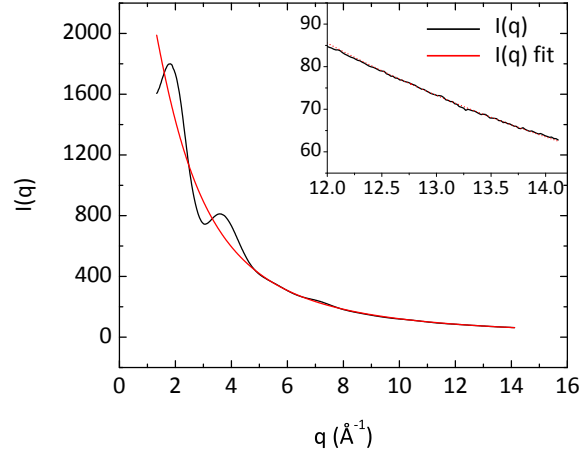
Figure 2.18: *Graph of the intensity distribution, I(q), from diffraction data collected from a Ta_2O_5 coating*

The scattering factor, f as defined in Equation 2.27 (Page 38), can be fitted to the experimental data using a parameterised asymptotic representation developed by Kirkland [102] where $f_{Kirkland}$ is defined in the following way,

$$f_{Kirkland} = \sum_{i=1}^{3} \frac{a_i}{q^2 + b_i} + \sum_{i=1}^{3} c_i \exp(-d_i q^2), \qquad (2.44)$$

where a_i, b_i, c_i and d_i are the Kirkland fitting parameters.

The terms $\langle f \rangle^2$ and $\langle f^2 \rangle$ used in the definitions of $I(q)$ and $\varphi(q)$ then become,

$$\langle f \rangle^2_{Kirkland} = p_O f_O^2 + p_{Ta} f_{Ta}^2 + p_{Ti} f_{Ti}^2, \qquad (2.45)$$

and

$$\langle f^2 \rangle_{Kirkland} = (p_O f_O + p_{Ta} f_{Ta} + f_{Ti})^2, \qquad (2.46)$$

where $p_z = N_z/N_{total}$ and z = O, Ti, Ta as required is the composition factors of O, Ti and Ta. Appendix A lists the Kirkland fitting parameters used in this thesis for O, Ti, and Ta.

An example of the fitted $I(q)$ is shown as the red line in Figure 2.18 with a magnified area showing a good fit between $N\langle f(q)^2 \rangle + I(q_{max}) - N\langle f(q_{max})^2 \rangle$ and $I(q)$ at high q.

Acquiring the reduced scattering factor After a good fit has been achieved with $I(q)$, the reduced scattering factor, $\varphi(q)$, can be computed through Equation 2.38. Figure 2.19 shows the $\varphi(q)$ computed from the previously fitted $I(q)$.
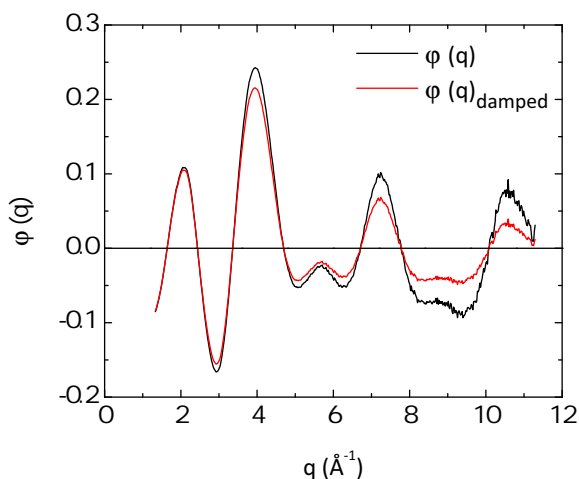
Figure 2.19: *Graph of the reduced scattering intensity distribution, $\varphi(q)$, from diffraction data collected from a Ta_2O_5 coating*

In Figure 2.19, the $\varphi(q)_{damped}$ plot uses a technique to reduce the effects of noise in the data by applying a damping term, $D(q) = \exp(-bq^2)$, where b is the damping factor [113]. This damping term reduces oscillations in the sum of wave functions that produce $G(r)$, as defined in Equation 2.39. Research conducted by Chen [115] shows that application of the damping factor effectively reduces noise, particularly at high q, and makes a negligible difference to the peak positions and widths on the final $G(r)$ plot where the damping factor ≤ 0.5. The use of the damping factor is standard practice when producing the RDF when there is noise present at high q.

Acquiring the reduced density function The RDF can then be computed through Equation 2.39 and an example Ta_2O_5 $G(r)$ plot is shown in Figure 2.20. The variables N, q_{max} and b can be adjusted so that the best possible fit to experimental data is achieved and an accurate $G(r)$ is found. Diffraction patterns placed in the middle of the CCD experience a degradation

in data quality as the edges of the rectangular CCD are reached. At high q data becomes very noisy and can be cut from the analysis to ensure a good fit with the rest of the data. However, for every diffraction pattern there is always an attempt to include the maximum amount of radially averaged data points from the diffraction pattern, and therefore get the highest q range, or highest q_{max}, possible. For the majority of the analysed diffraction patterns the average maximum q value, q_{max}, used was around $q_{max} \sim 10$, which is roughly 600 radially averaged data points from the diffraction pattern.
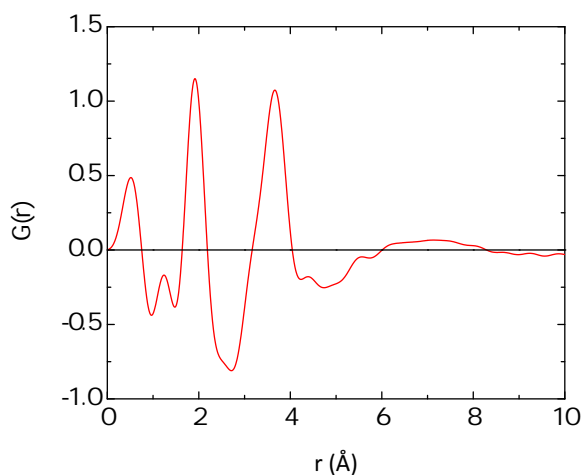
Figure 2.20: *Graph of the reduced density function, $G(r)$, from diffraction data collected from a Ta_2O_5 coating*

Data below 1 Å in the RDF can is regarded as noise, as these distances are unphysical, and is minimised by ensuring the best possible fit to the data. Disregarding the noise peak below 1 Å in the example Ta_2O_5 $G(r)$ shown in Figure 2.20, there are two distinct peaks at 1.9 Å and 3.8 Å. These peaks represent the distances from a central atom where atoms are likely to sit, and are therefore the nearest atomic neighbour distances. To find out what the atoms at these distances are likely to be, it is possible to compare these distances from known crystal Ta_2O_5 structures. The Cambridge Crystal Structure Database [116] has many such structures, and reveals that Ta - O distances occur around the 2 Å point and Ta - Ta distances at around 3.5 Å. Therefore, one could assume

that the peaks in the amorphous Ta_2O_5 RDF are the result of Ta - O and Ta - Ta distances for the 1.9 and 3.8 Å peaks. However there is not a great deal of certainty, at this point, with atomic distances because there is no way of resolving the data between the different atomic species.

Atomic modelling In order to accurately probe the atomic structure further and gain a fuller understanding of the information stored in the RDF, Reverse Monte Carlo (RMC) refinements of atomic models using the experimental data from the RDF can be carried out. Information from density functional theory molecular dynamics (MD) simulations of liquid quenching is used in the RMC refinements in order to obtain a physically stable model of the amorphous material, which fits both the theoretical and experimental data. The modelling process can be broken into three stages as will now be described. These stages represent an example of the most commonly used settings for modelling, although this can be changed and further details will be given where the process deviates from the description below.

stage one An initial small model of generally < 100 randomly packed atoms in a cubic cell is created and then refined using RMC software developed by Borisenko [117, 118] to fit the experimental RDF. The size of the model at this stage is chosen to provide an acceptable balance between containing enough atoms to allow a reasonable representation of the structure and few enough to still allow the MD simulations to run in a reasonable period of time. The cell size is chosen so that it gives a density close to an experimentally measured density. This initial model is then refined using an RMC approach by comparing $\varphi(q)$ calculated from the model structures with the experimental $\varphi(q)$ and moving random atoms until an acceptably good match is achieved.

stage two In the second stage, CASTEP [119] is used to perform MD simulations based on density-functional theory (DFT), this allows us to ensure

that all the atoms in the model sit in a physically reasonable positions. This utilises norm-conserving pseudopotentials of Lee *et al.* provided within the CASTEP code [119] within the generalised gradient approximation (GGA) using the Perdew-Burke-Ernzerhof (PBE) exchange-correlation functional [120] where an energy cut off is set at 200 eV. The RMC refined small model is used as a starting structure for melting and cooling simulations using MD within a canonical (constant NVT) ensemble. The model is first melted at 3000 K for 5 ps, then cooled down to 2000 K and equilibrated for 10 ps. The melt is then cooled down to 500 K in steps of 300 K, allowing 5 ps equilibration at each step. Finally, the structure is equilibrated at 300 K for 10 ps. Total simulation time is therefore 50 ps with the time step of 2 fs. Although several high frequency vibrational modes (for instance, including bonded vibrations) can be anticipated in the material, a longer time step is used as a reasonable compromise between describing atomic diffusion and vibrations. The temperature is controlled using an implementation of the Nose-Hoover thermostat. [121] The electron density was sampled only at the gamma point, which is a reasonable approximation considering the material is an insulator.

stage three To better understand the atomic structure of the amorphous Ta_2O_5 over a longer range, a final large model for RMC refinement is prepared by assembling together 27 randomly oriented small models obtained from the MD simulations of liquid quenching. This model is then refined using one small 0.1 Å maximum displacement step per iteration in the RMC routine, to preserve the simulated bond length and angle distributions as much as possible, while at the same time fitting the model to the experimental diffraction data and avoiding any unphysical distances.

The modelling refinement process is best represented in a flow chart as shown in Figure 2.21 where the individual steps are carried out as described

above. This diagram shows the key steps involved that have been previously described in this section.
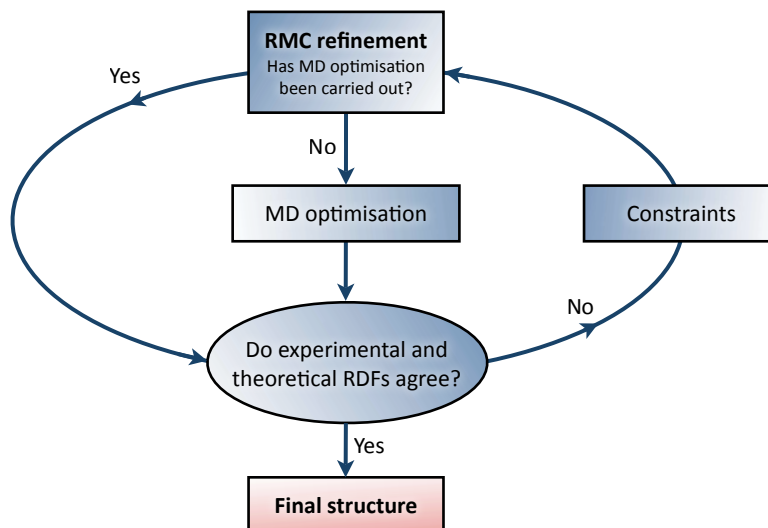
Figure 2.21: *Flow chart of the iterative modelling refinement process, from an initial model where constraints are applied and leading to a final energy optimised atomic structure*

The resultant atomic model gives the ability to look at how each atomic species in the sample behaves. One can therefore obtain the partial RDFs between any two atomic species pair such as Ta - O, Ta - Ta or O - O and gain bond type and angle distributions. This is an important step in understanding the atomic structure, as it allows the full interpretation of the data stored in the RDF.

This data can then be used to compare to differences in the measured mechanical losses of the coatings to identify a potential mechanism. Results from the RDFs of the various mirror coatings studied and their atomic models are shown in the following experimental chapters.

2.4.7.3   Note on fitting issues with the RDFs

As previously mentioned in Chapter 2 the RDF measurements rely on good quality data, where having a clean and thin sample, accurately measured stoichiometry and good TEM calibration are key to getting the best quality fit.

The best fit is obtained when scattering intensities calculated from the Kirkland fitting parameters closely match the experimental data at high q, for a $q > 10$ (see Section 2.4.7.2 for further explanation).

The quality of fit can be measured by the size of the noise peak below 1 Å in the RDF plots, where large noise peaks indicate a poorer fit and small noise peaks indicate the best quality fit. It is primarily the aim to only consider RDFs that produce good fits with experimental data, where the noise peak is significantly less than the subsequent peaks above 1 Å in the RDFs. These then go into the average RDF calculation, further reducing the effects of any random noise. This is because large noise peaks, indicating poorer fits, can affect primarily the second, and to a lesser extent the first, peak heights in the RDF above 1 Å. Figure 2.22 shows this effect on the same electron diffraction data when a large positive or negative noise peaks are present, compared with the optimal fitting for this particular data set. When the noise peak is positive it has the effect of over estimating the second peak, and when it is negative it underestimates the second peak. There are only minimal changes to the position of the first peak and the remainder of the RDF.
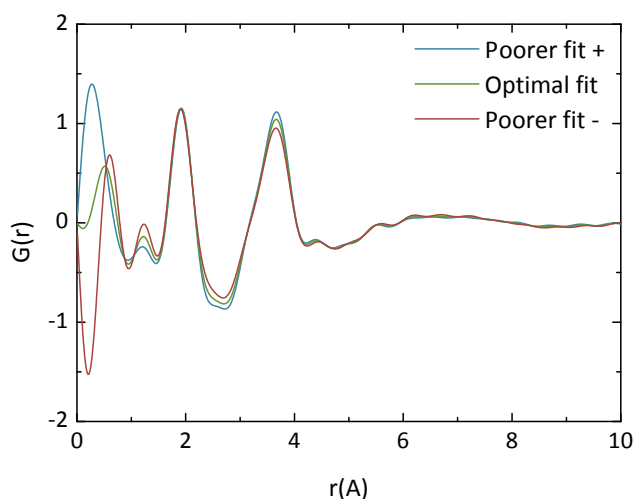
Figure 2.22: *RDFs of the same electron diffraction data with different size noise peaks below $r = 1$ Å. The data shows how a poor fit which is indicated by a large loss peak can cause changes in RDF peaks at greater r.*

These loss peaks vary in each RDF produced and are therefore the cause of much of the errors with the statistical analysis of the RDFs for each type of coating. The electron diffraction data from the MLD Ta_2O_5 coatings was particularly difficult to produce good fits with when creating the RDFs. Due to the nature of the sample preparation, the coating is more likely to be thicker when it is closer to the substrate, and it is difficult to collect data from the thinnest areas where electron scatter is at a minimum and the best quality RDFs are produced. It is therefore possible the trends seen in the RDF statistical analysis are exaggerated or are indeed reduced due to a reduction in the quality of fits. It is not possible to accurately quantify this effect at present.

Further investigations are required to improve our data collection and fitting procedures to ensure the best quality RDF data. The primary aim will be to extend the q range of our data, where the Kirkland scattering potentials should match the data well at high q, producing the best quality fits. Improvements will also be made to the sample preparation process to create the greatest amount of thin coating areas (around 10 nm) and find better ways to avoid any contamination, which causes a build-up of free carbon on the coating surface and essentially increases the sample thickness.

2.5   Conclusions

Thermal noise arising from the mechanical loss of the dielectric mirror coatings used in the optics of interferometric gravitational wave detectors is an important limit to the detector sensitivity. Understanding the sources of the mechanical loss and how this relates to the atomic structural properties of the coatings is important if we are to find ways of reducing its effects for future generations of detectors. Hence significant efforts have been made to firstly measure the mechanical loss of different types of low loss materials that are used in the dielectric materials. Also, understanding the material properties of these coatings and identifying the mechanisms of mechanical loss is of sig-

nificant interest. Techniques have been developed using transmission electron microscopy to probe the atomic structure and chemistry of the coatings, notably using reduced density functions, for the first time, as a way of examining the atomic structure of amorphous mirror coatings.

The research presented in this thesis uses the theory and experimental techniques described in this chapter to investigate the mechanical loss and the atomic structure and chemistry of a variety of candidate mirror coatings, in an attempt to develop ways of identifying the sources of thermal noise and understand the mechanisms behind it.

Chapter 3

Investigations into the material properties of Ta$_2$O$_5$ mirror coatings

3.1 Introduction

As discussed in Chapter 2, thermal noise arising from the mechanical loss in the mirror coating material is expected to be an important limiting factor to the sensitivity of future interferometric gravitational wave detectors. This limiting factor is expected at the most sensitive operational frequency band of the detectors from tens, to several hundred, Hertz [65, 75]. Therefore, reducing the effects of coating thermal noise has become an active area of research key to the design of future generations of detectors.

This chapter will focus on the effect of heat-treatment on temperature dependent mechanical loss measurements and the atomic structure of pure Ta$_2$O$_5$ coatings. As mentioned in Chapter 1, some of the planned third generation gravitational wave detectors may work at cryogenic temperatures in order to reduce thermal noise. Although this may seem an intuitive way to reduce thermal noise, at very low temperatures both Ta$_2$O$_5$ coatings and SiO$_2$ show loss peaks having an activation energy related to the loss process. In the bulk SiO$_2$ used for test-mass substrates, a broad loss peak occurs centered at around 50

K [122, 123], which is thought to be caused by thermally activated transitions of oxygen atoms between two energy states - where there is a distribution of bond angles in the amorphous structure. This broad loss peak means that SiO$_2$ is not the substrate material of choice for studying the mechanical loss of the coatings at low temperatures. Instead single crystalline silicon, which has low loss at cryogenic temperatures is the preferred substrate [124]. Ta$_2$O$_5$ coatings, as will become apparent, have low temperature loss peaks that change with the heat-treatment of the coatings carried out during the manufacturing process [125, 126]. The exact reason for these observed changes in the mechanical loss as a function of temperature is not well understood and is an area of active research, as it presents an interesting avenue from which to study the possible underlying mechanisms of mechanical loss. Therefore it is important to understand how heat-treatment leads to changes in the fundamental loss mechanisms. Understanding the effect of heat-treatment on the atomic structure, and correlating structural changes to the observed changes in the mechanical loss, is an important step forward in this process.

3.2 Investigating the effect of heat-treatment on Ta$_2$O$_5$ coatings

3.2.1 Mechanical loss measurements

Mechanical loss measurements were previously carried out by I. Martin on Ta$_2$O$_5$ coatings heat-treated at 300, 400, 600 and 800 °C, where the coated samples had been placed in an oven for 24 hours in air at the desired temperature subsequent to deposition. The coatings were manufactured by CSIRO [127] and were each 500 nm thick. These coatings were deposited on silicon cantilevers (as opposed to SiO$_2$ cantilevers) in order to avoid the low temperature loss peak observed with silica, as discussed in the Introduction. The experimental method followed a similar process to that outlined in Chapter 2,

Section 2.3.4, and the results are shown below in Figure 3.1 [126].
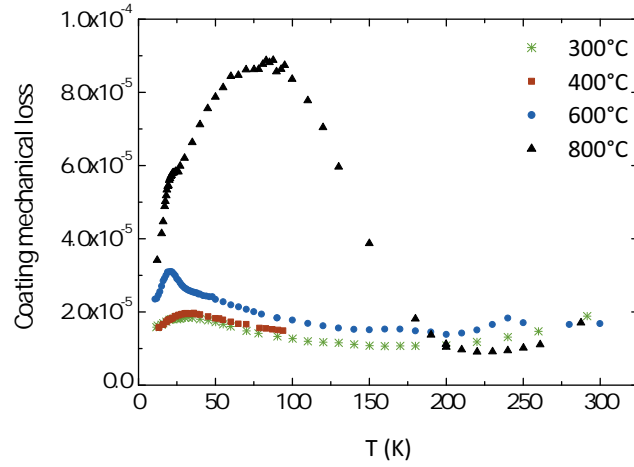
Figure 3.1: *Mechanical loss measurements of the fourth bending mode (1960 Hz) of four cantilevers coated with Ta_2O_5 and heat-treated at 300, 400, 600 and 800 °C respectively [126].*

A low temperature loss peak is clearly visible for each heat-treatment temperature measured. For the 300 and 400 °C coating a broad loss peak occurs at around 35 K. For the 600 °C coating a much more defined loss peak occurs at 20 K. The 800 °C coating has a large and broad loss peak at around 80-90 K, which has a small plateau at around 20 K, suggesting another emerging loss peak. The clear changes between the coating mechanical loss at cryogenic temperatures and heat-treatment suggests some interesting changes in the structure of these coatings. To probe these structure changes and find ways of accurately analysing them, atomic structure investigations using transmission electron microscopy were then carried out and are discussed in the following subsections.

3.2.2 Initial TEM measurements

The initial investigations using the TEM included bright field imaging and electron diffraction (see Chapter 2, Section 2.4.6).

Figure 3.2 (a) shows a representative bright field image from a single layer
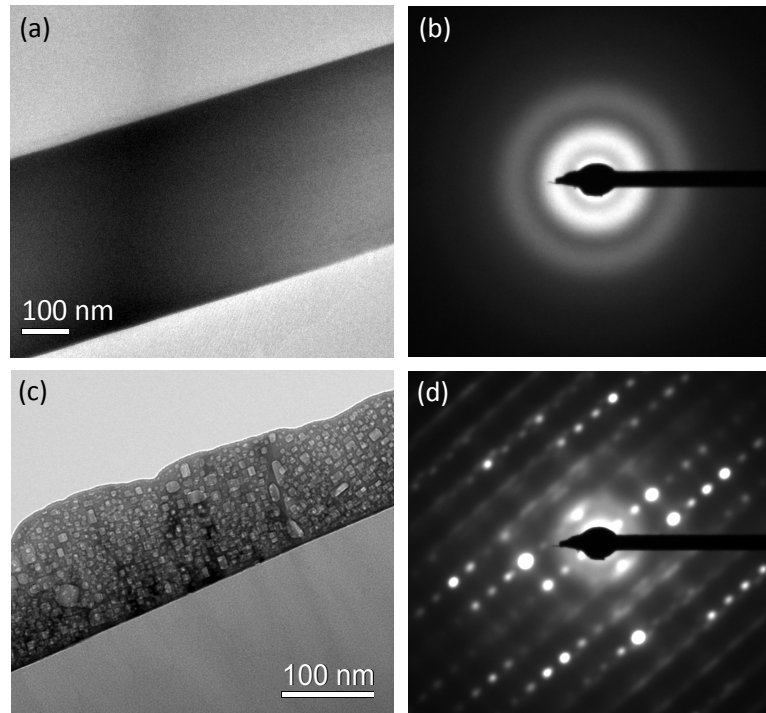
Figure 3.2: *(a) bright field image of a single layer amorphous Ta$_2$O$_5$ coating where the dark layer is Ta$_2$O$_5$ and light layer is SiO$_2$ substrate, (b) amorphous diffraction pattern of a Ta$_2$O$_5$ layer from the 300°C coating, (c) bright field image of a single layer crystallised 800°C Ta$_2$O$_5$ coating where the dark layer is Ta$_2$O$_5$ and light layer is SiO$_2$ substrate and (d) crystalline diffraction pattern, showing Bragg scattering spots of a Ta$_2$O$_5$ layer from the 800°C coating.*

Ta$_2$O$_5$ coating where the higher atomic number Ta atoms produce more electron scatter and therefore a dark layer appears, as compared to the lower atomic number Si atoms which make the SiO$_2$ substrate appear lighter. When the coating remains amorphous a typical diffraction pattern as shown in Figure 3.2 (b) is observed, where diffuse rings are present as a consequence of the short range order in the structure. Similar diffraction patterns are visible for the coatings heat-treated to 300, 400 and 600 °C, demonstrating that these coatings are substantially amorphous. Figure 3.2 (d) shows the diffraction pattern from the 800 °C coating shows well-ordered Bragg scattered diffraction spots indicating that the coating has crystallised and therefore has long

range order, with a grain size larger than the size of the aperture used to record this selected area diffraction pattern (that is hundreds of nm across). Comparing these results with the mechanical loss measurements show that a possible explanation for the large broad loss peak observed at around 80-90 K for the 800 °C heat-treated coating could be caused by onset of crystallisation induced by heat-treatment. Although changes in the diffraction patterns are subtle and difficult to pickup by eye, there are clearly large changes present in their mechanical losses. Changes in the diffraction patterns will only become evident and measurable with quantitative evaluation through the use of Reduced Density Function (RDF) analysis.

3.3   Atomic structure investigations

3.3.1   The 400 °C heat-treated coating

To gain the maximum amount of information stored in the amorphous diffraction patterns of the Ta_2O_5 coatings, the reduced density function (RDF) can be computed from the scattering intensities of the diffraction pattern which store information on the local atomic structure. The RDF itself gives a statistical representation of where the nearest neighbour atoms sit with regards to a central atom.

RDFs were computed from diffraction data collected from multiple thin areas of the coating, where the process of computing the RDF is described in Chapter 2, Section 2.4.7. An atomic model was then created by firstly creating a small model of 77 randomly packed atoms which was then reverse Monte-Carlo refined to fit the experimental RDF data. The size of the cell was chosen so that it gave a density close to the experimentally measured density of 7.68 g/cm^3 (see Appendix B for further details on the coating density measurement). Molecular dynamic (MD) simulations based on density-functional theory (DFT) were then performed to ensure all the atoms in the model sat in

physically reasonable positions, denoted as the DFT model at this stage. To better understand the amorphous Ta_2O_5 structure over a longer range, a large model was created by assembling together 27 randomly oriented small models obtained from the MD simulations and RMC refined back to experimental RDF data, to create a final refined model (or DFT + RMC model) used in the subsequent analysis. This process is described in further detail in Chapter 2, Section 2.4.7.2. It should be noted that pure Ta_2O_5 was assumed at this stage and subsequent analysis of EEL spectra of these coatings indicates variations in stoichiometry, see Section 3.4.1.
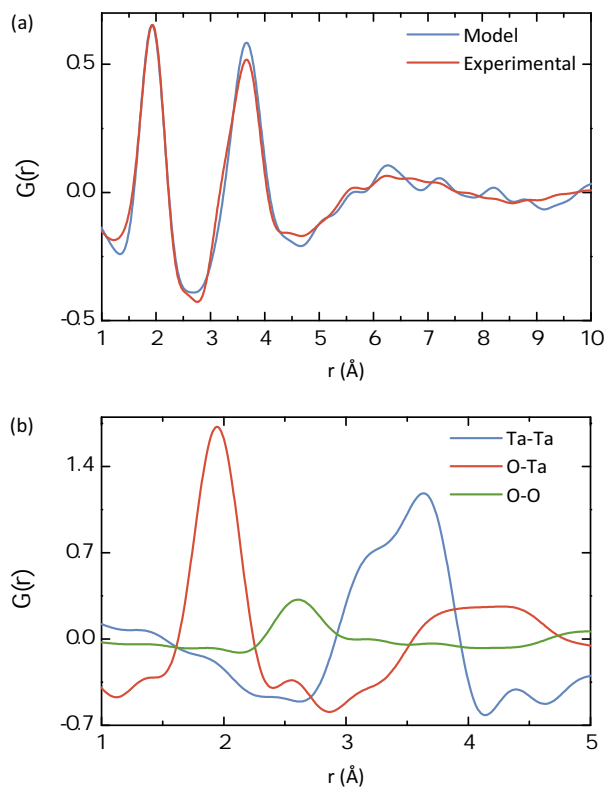
Figure 3.3: *For the $400°C$ Ta_2O_5 coating (a) shows the comparison between the final amorphous Ta_2O_5 model and experimental RDFs, (b) shows the partial RDFs showing individual nearest neighbour distances within the model. In both cases the y-axis $G(r)$ represents the normalised probability of finding an atom at a particular distance r (x-axis) from a central atom.*

The first investigations were carried out on the 400 °C coating and the resultant RDF is shown in Figure 3.3 (a) along with the RDF generated with the final model which shows good agreement with experiment. Figure 3.3 (b) shows the partial RDFs (PRDFs) computed from the final model, where only interactions between two types of atoms are taken into account, i.e., Ta-Ta, Ta-O and O-O, and the sum of these partial RDFs represents the total RDF generated from the model. Comparison between the PRDFs to the computed RDF show that the the first peak position corresponds to the Ta-O distances found at 1.93 Å and the shoulder of the second peak at around 3.2 Å corresponds to Ta-Ta distances. Beyond the second peak there appears to be no longer range order, as expected from an amorphous material [103].
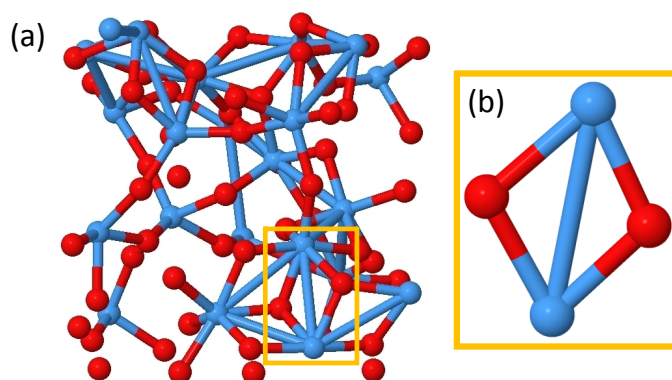
Figure 3.4: *For the 400° C Ta$_2$O$_5$ coating (a) shows the atomic model from the molecular dynamics simulations and (b) highlights the stable Ta$_2$O$_2$ ring fragment*

Analysis of the model shows that the refined amorphous structure has a considerable contribution from a planar or nearly planar Ta$_2$O$_2$ ring fragment with an average Ta-Ta distance of 3.2 Å as highlighted in Figure 3.4 (b). The Cambridge Crystal Structure Database provides access to the structure of a number of previously studied compounds containing similar fragments with Ta-Ta distances varying from 2.71 Å to 3.64 Å with an average of around 3.2 Å in good agreement with the value obtained from the model [128]. Similarly the

Ta-O distances in the model were also in good agreement with these compounds and also the crystalline phases of Ta_2O_5.
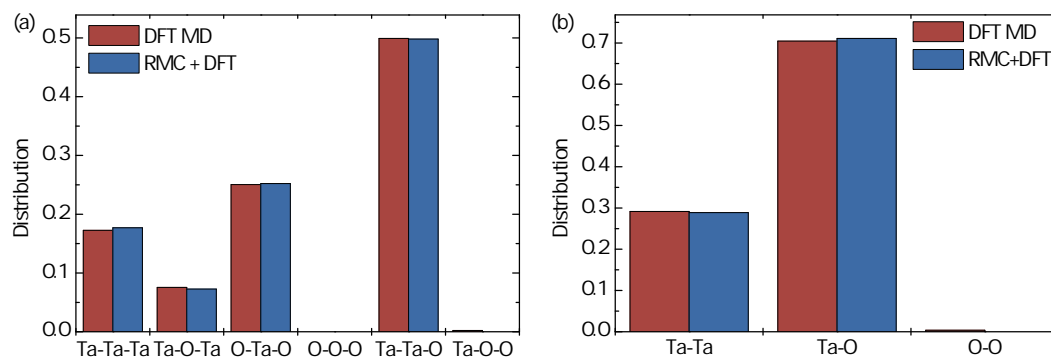
Figure 3.5: *Parameter distributions for the 400°C coating after the molecular dynamics step compared with those after the large model RMC step: a) bond angle type distribution; b) bond type distribution.*

Studying the bonds in the sample yields useful comparative information, where a bond is defined as an atom to atom distance of less than the sum of their covalent radii (Ta = 1.7 Å [129], O = 0.73 Å [130]) plus a bond tolerance factor set at 0.1 Å. Figure 3.5 shows that there is no apparent change in the bond distribution between the structure modelled by the the DFT MD simulations and the refined model.
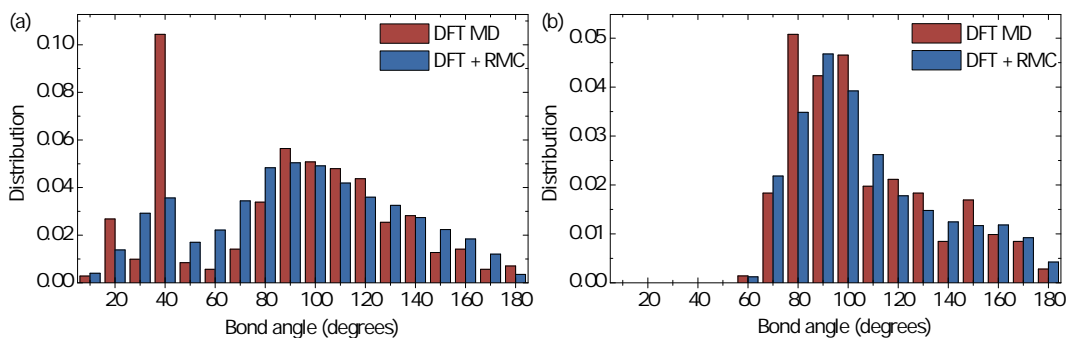
Figure 3.6: *Bond angle distributions for the 400°C coating after the molecular dynamics step compared with those after the large model RMC step:a) Ta-Ta-O angles; b) O-Ta-O angles.*

Figure 3.6 shows that the bond angle distributions show the most consid-

erable changes between the DFT MD and the refined model in the number of Ta-Ta-O angles between 30-40 ° and in the number of O-Ta-O angles between 70-80 °. These bond angles represent those of the Ta_2O_2 ring fragments and show that they are slightly over represented in the DFT MD model. However overall analysis of the bond type and bond angle distributions of the DFT MD model only show a very small difference with the refined model. This shows that the (final DFT and RMC) refined model represents a good match to the experimental diffraction data and also has an energetically stable atomic structure.

This initial investigation into probing the atomic structure of the 400 °C Ta_2O_5 coatings appears to yield promising results for identifying structural information that may be useful for comparing differences in atomic structures between other coatings with varying constituent properties and manufacturing methods [131].

3.3.2 The 300 °C and 600 °C heat-treated coatings

The next stage was to investigate the atomic structure of the coatings with varying heat treatment temperature. Choosing the 400 °C coating as the first coating to study was deliberate because it is close to the mid point of our heat treatment temperature steps. In order to avoid the lengthy process of a new DFT MD model for each temperature step, the 400 °C DFT model was used, as before, to build larger models which were then RMC refined to the experimental RDFs of the 300 and 600 °C coatings. The assumptions made at this point were that both the 300 and 600 °C coatings were pure Ta_2O_5 and that they had a density equal to the 400 °C coating. The 400 °C was also allowed to refine further in order to achieve the best possible agreement with experimental results.

Figure 3.7 (a) shows the averaged RDFs of at least five individual RDFs, generated from diffraction patterns taken from different areas in the coat-
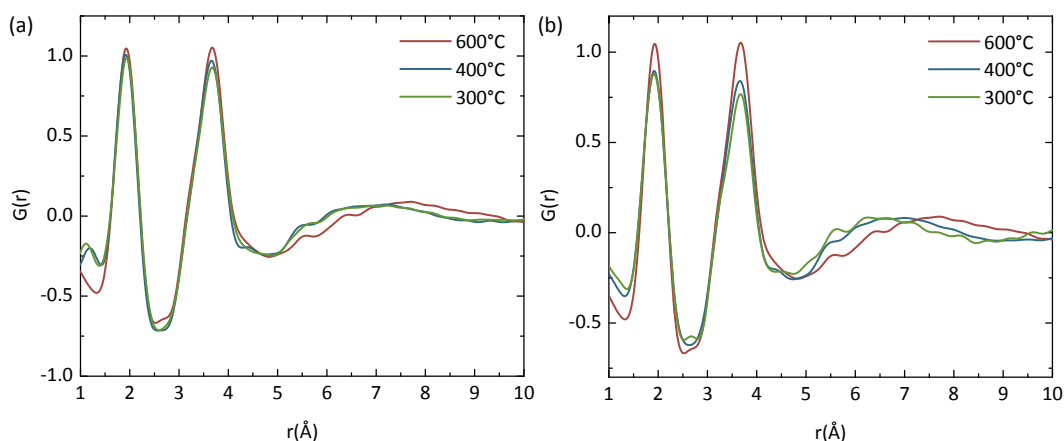
Figure 3.7: *Experimental RDFs for the modelled CSIRO Ta_2O_5 coatings, showing (a) the averaged experimental RDFs for each coating and (b) RDFs chosen that emphasise the change in local structure present between the coatings.*

ing, that show only subtle changes in the atomic structure with varying heat-treatments. They show that as the temperature is increased the peaks become more well defined, suggesting an increase in local ordering towards a crystalline state, as happens with the crystallised $800\,°C$ heat-treated coating. The second peak, which relates to Ta-Ta atomic distances and longer range Ta-O distances, also increases in height faster than the first peak. Although there is evidence that the coatings are becoming more ordered with increasing heat-treatment temperatures, there was no evidence of any crystallisation in the 300, 400 and $600\,°C$ coatings. This was further investigated using HRTEM to search for signs of nano-crystals in the coating structures, however no evidence of their existence was found.

The average changes are subtle, however individual RDFs showing the local structure at a particular point in the coating can show greater changes. For this reason we can emphasise the trends shown in the averaged RDFs by choosing a single local structure RDF from each of the heat-treated coatings which show the greatest difference, as shown in Figure 3.7 (b). This allows us to better identify the changes in the atomic structure that take place during heat-

treatment, even though it only relates to the area with the greatest difference.

To fully study the maximum changes seen with heat-treatment, atomic models were refined to the local structure RDFs shown in Figure 3.7 (b).

The partial RDFs from these models are shown in Figure 3.8, where RDFs are generated by taking only two atomic interactions into account from the models, i.e., Ta-O, O-O and Ta-O. Therefore the sum of these partial RDFs would give the full Ta_2O_5 RDF. At this stage, these are only distance relationships and not necessarily bonds. Figure 3.8 (a) and (c), Ta-O and Ta-Ta bonds show the greatest change in the first major peaks, and less of a difference in interactions at greater distances. As previously discussed the Ta-O occurs at around 1.9 Å and from the partial RDFs it is clear that there is little effect from other atomic interactions on this peak. The Ta-O distances impact slightly on the second major peak at 3.2 Å however as the heat-treatment temperature increases, the Ta-O contributions to the second peak do not significantly change, instead the changes to the second peak are dominated by Ta-Ta interactions. In-between the two major peaks from Ta-O and Ta-Ta interactions in the RDF lies the O-O distances, where the peak heights are emphasised by the y-axis scale used in 3.8(b) and the influence of these distances on the total RDF is minor due to the small scattering factor of oxygen. Moreover, this O-O partial RDF seems rather insensitive to heat treatment temperature. This RDF does not show significant changes as heat treatment temperatures are varied. This suggests that changes in the atomic structure as heat-treatment temperature is increased are dominated by an increase in the ordering in Ta-O distances, Ta-Ta distances and longer range Ta-O distances.

There are also some visible changes in the bond distributions, where as before, we define a bond to be an atom to atom distance of less than the sum of their covalent radii plus a tolerance factor of 0.1 Å. Figure 3.9 (a) shows the bond distributions for the different heat-treated coatings for Ta-Ta, Ta-O and O-O bonds. The bond type distributions show that as heat-treatment tempera-
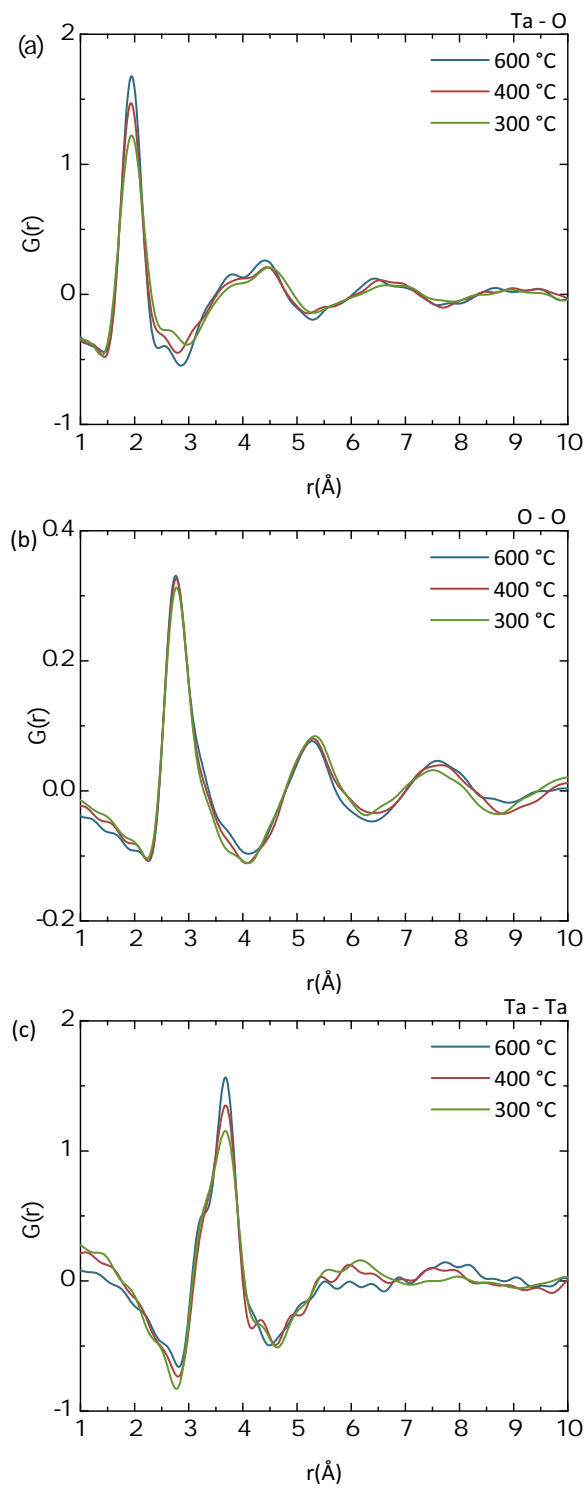
Figure 3.8: *Partial RDFs for the heat-treated Ta₂O₅ coatings, when considering only a) Ta-O distances, b) O- O distances and c) Ta-Ta distances.*
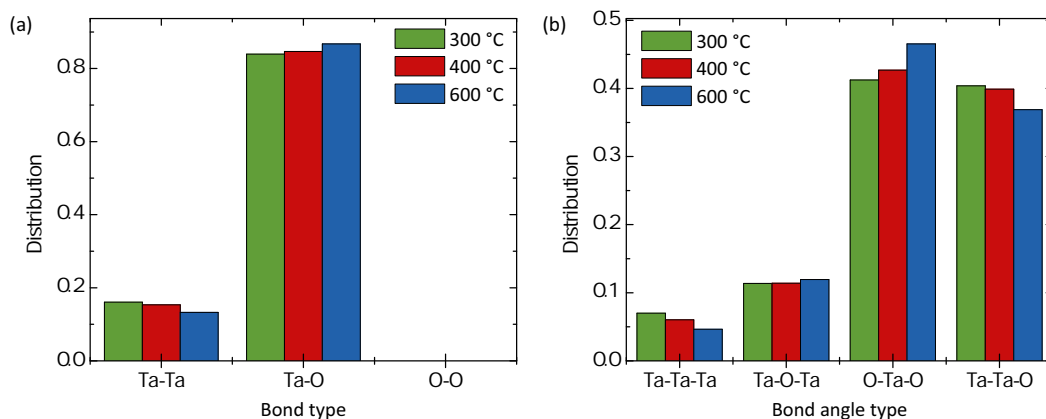
Figure 3.9: *Parameter distributions for the heat-treated Ta_2O_5 coatings for a) bond type distributions and b) bond angle type distributions.*

ture rises the distribution of Ta-Ta bonds decrease and the distribution of Ta-O bonds increase. This suggests that as heat-treatment temperature increases Ta atoms move further away from neighbouring Ta atoms, decreasing the Ta-Ta bond distribution, and allowing an increase in bonding with O atoms. There were no O-O bonds found in any of the models. The bond angle type distributions were also studied for Ta-Ta-Ta, Ta-O-Ta, O-Ta-O and Ta-Ta-O bond angle types, and are shown in Figure 3.9 (b). This illustrates that the most prevalent bond angle types in these coatings are O-Ta-O and Ta-Ta-O, with relatively minor contributions from Ta- Ta-Ta and Ta-O-Ta bond angles. The greatest variation in the bond angle types is O-Ta-O and Ta-Ta-O, in line with the variations in the bond types, where Ta-O contributions increase and Ta-Ta contributions decrease with rising heat treatment temperature.

Bond angle distributions were also studied to further explore the bond angle types for each model and are shown in Figure 3.10, where the bond angle distributions are normalised to their bond angle type. The Ta-Ta-O bonds between 30-40 $^{\circ}$ (Figure 3.10 (b)) and O-Ta-O bonds between 70 and 80 $^{\circ}$ (Figure 3.10 (d)), which are a result of the Ta_2O_2 ring fragments, in the 600 $^{\circ}$C coating. As previously mentioned, these ring fragments can be thought of as crystalline building blocks and they have an increased presence as the heat-
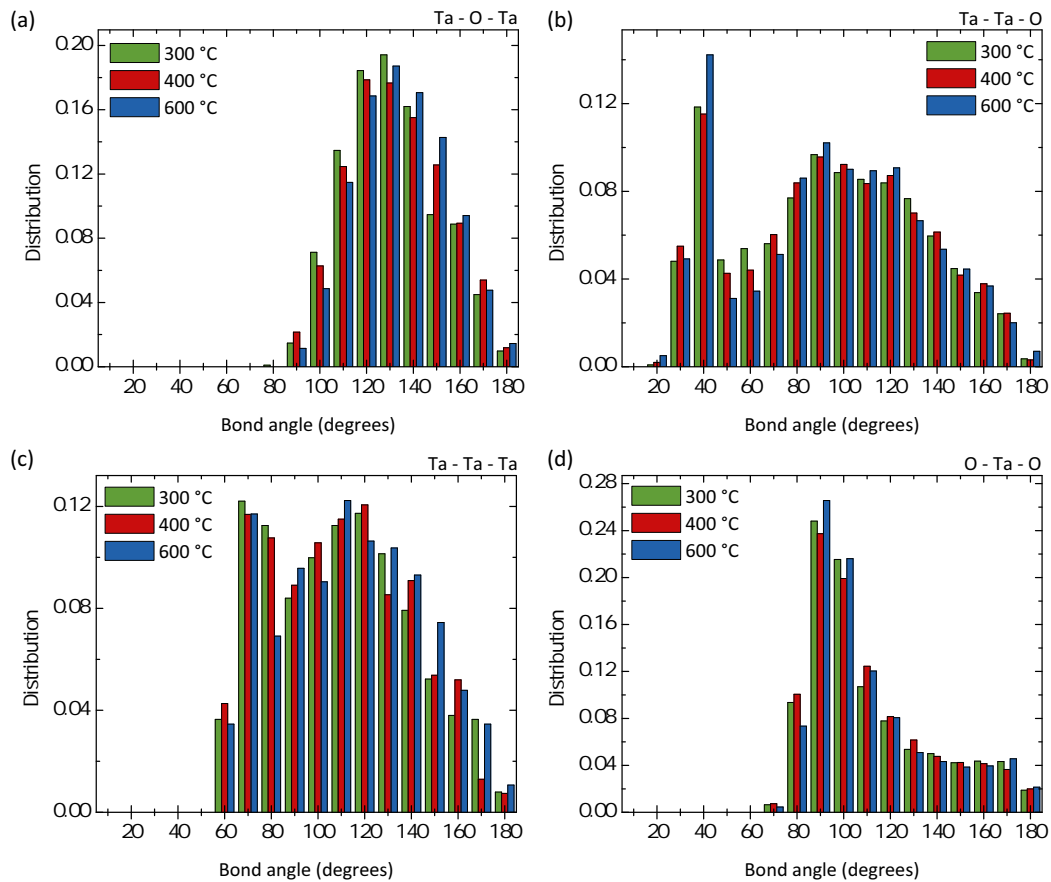
Figure 3.10: *Bond angle distributions for the heat-treated Ta_2O_5 coatings for a) Ta-O-Ta angles, b) Ta-Ta-O angles; c) Ta-Ta-Ta angles; and d) O-Ta-O angles.*

treatment temperature rises as seen by the rise in Ta-O bonds, giving further evidence of a more ordered state. However, as the heat-treatment temperature rises the distribution of Ta-Ta bonds decreases and they essentially stretch so that the two tantalum atoms are far enough from each other that they are no longer bonded, although the ring structure of Ta-O-Ta-O still exists. Evidence of this trend is seen in the bond angle distributions where, as shown in Figure 3.10 (a), the distribution of Ta-O-Ta bonds sit at higher angles, from 140-180 °, as heat-treatment temperature increases, as would be expected if the Ta_2O_2 ring fragment is stretching. Figure 3.10 (c) shows the distribution of Ta-Ta-Ta bond angles having a sharp maximum at 70-80 ° and high probability of

finding angles at 110-120°, where there appears to be a preference towards higher angles as heat-treatment temperature increases, although there is not a large visible difference in the angle distributions, even if the occurrence of this bond type within the atomic model is decreasing (Figure 3.9 (b)).

Atom	300 $^\circ$C	$\pm$	400 $^\circ$C	$\pm$	600 $^\circ$C	$\pm$
Tantalum	5.40	1.80	5.60	1.75	5.24	1.78
Oxygen	1.59	0.71	1.63	0.67	1.65	0.65

Table 3.1: *Co-ordination numbers for the heat-treated Ta_2O_5 coatings, the '$\pm$' values indicate the spread obtained for a given co-ordination number.*

The number of bonds that each atom type on average is likely to have is given by its co-ordination number. The co-ordination numbers of the materials in these coatings were also studied using the same bond conditions as previously described, and are shown in Table 3.1. There is considerable spread in the co-ordination numbers, as can be expected due to the nature of amorphous materials producing a range of bonding configurations, which makes it difficult to draw any firm conclusions. However, the average co-ordination numbers suggests that as heat-treatment temperature increases the average co-ordination number of tantalum is at its highest for the 400 $^\circ$C coating and then decreases for the 600 $^\circ$C coating, with the oxygen co-ordination number gradually increasing with temperature. This agrees with previously described bond distributions where the distribution of Ta-O bonds increases and Ta-Ta bonds decreases as the heat-treatment temperature increases. These co-ordination numbers appear to be significantly lower than published high temperature studies of Ta_2O_5 of co-ordination numbers in the region of 6 to 7 for tantalum and oxygen in the region of 2 to 3. The reason for this may be due to the initial assumption that the models were created under, where perfect stoichiometry of Ta_2O_5 was assumed. As will become apparent in the following sections these coatings are oxygen deficient. The effect of extra oxygen atoms in the struc-

ture can cause an underestimation in the co-ordination of each oxygen atom and subsequently tantalum atoms. This is because some of the oxygen atoms in the models appear not to be bonded at all and therefore indicating that the model has not reached an equilibrium due to over estimating the number oxygen atoms. It is therefore important that experimental stoichiometry be measured and used as an input for future models in order to obtain the most accurate models possible.

3.4 Improvements to data quality

Although there are observed changes in the heat treated coatings as has been discussed, there are some areas where it is possible to improve the experimental procedure in order to get the most accurate results possible. To that end research was carried out to allow the inclusion of variations in the stoichiometry of the different heat-treated Ta_2O_5 samples using data from electron energy loss spectroscopy (EELS) data and improve statistics by increasing the collected TEM data and hence the number of RDFs studied.

3.4.1 Including EELS stoichiometry

EEL spectra were used to calculate the stoichiometry (see Chapter 2) of the 300, 400, 600 and 800 °C heat-treated Ta_2O_5 and the results are shown in Figure 3.11 where a tantalum to oxygen ratio of 0.4:1 is the ratio that gives a perfect stoichiometry of Ta_2O_5. It shows that the three coatings that remain amorphous (300, 400 and 600 °C) are oxygen deficient and the 800 °C coating, which has crystallised becomes oxygen rich.

From these results it is clear that the stoichiometry deviates from the previously assumed Ta_2O_5. Therefore in order to obtain the most accurate results possible it is necessary to use these stoichiometries when generating the RDFs and atomic models in order to get the best fit with experimental data.
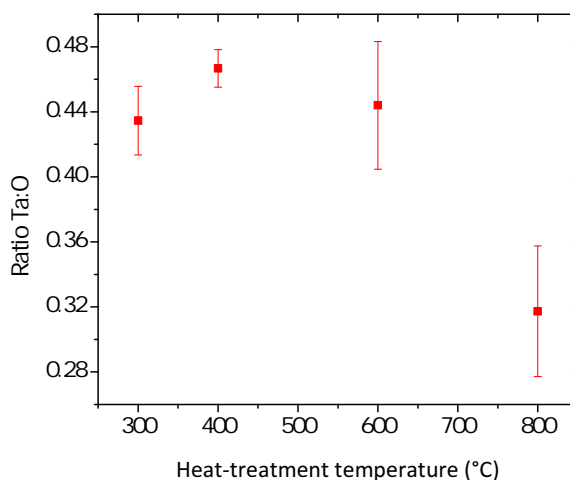
Figure 3.11: *The ratios of Ta:O in the heat-treated coatings, where Ta:O of 0.4:1 gives the ratio for pure Ta_2O_5.*

3.4.2   Increasing the number of RDF measurements

Increasing the number of RDFs is also important when considering the quality and error associated with the RDF. Therefore more TEM electron diffraction data were taken with the 300, 400 and 600 °C heat-treated Ta_2O_5 coatings, in order to improve the quality of the statistics. The EELS stoichiometry for these coatings was also used when calculating the RDFs.

The results are presented in Figure 3.12, where rather than showing the individual RDFs, the most important features of the RDFs, the first and second peak position, height and full width at half maximum, are shown for the different heat-treatment temperatures. Changes in the peak positions would indicate changes in the distance distributions in the sample. An increase in the peak heights along with a decrease in FWHM would suggest an increased order in the coating, giving more tightly defined atomic distances, suggesting a tendency towards a crystalline state. As the previous sections on the coating modelling suggest, the first peak in the RDF predominantly occurs from Ta-O distances and the second peak from Ta-Ta distances and longer range Ta-O distances. Therefore by analysing these key attributes of the RDF, it allows the tracking of any changes in the RDFs and hence atomic structure between

different coatings, before the modelling stage. It also gives a statistical error produced from the variance of multiple RDFs measured for each coating.

Figure 3.12 shows that from an average throughout the coating of around 15 RDFs for each coating, it is apparent that there is no clear differences between the coatings and that most of the observed changes lie within error. The reason for this may be due to problems with the RDF fitting, where many RDFs had large noise peaks. The exact cause for this is still under investigation and it was decided that only the best fits would be carried through to the final results, which were the 15 RDFs used in the analysis for Figure 3.12 (See Chapter 2, Section 2.4.7.3, for further discussion).

It should be noted that local structural changes are still observed as investigated previously in this chapter. This means that in the process of averaging many RDFs variations in the local atomic structure are lost, meaning that changes may be taking place over a longer range than is observable in the RDF short range order. The reasons for changes in the local atomic structure are explored further in Section 3.7 where the process of heat-treatment can be thought of as causing different changes through the coating itself from the coating surface to the coating areas closest to the substrate.

3.5   The 800 °C heat-treated coating

The 800 °C heat-treated Ta_2O_5 coating was the only coating studied from this set that had crystallised, and therefore there was no RDF analysis carried out on it. However, closer investigation of the coating shows some interesting structural properties.

Figure 3.13 (a) shows a typical TEM bright field image of amorphous Ta_2O_5 coating (dark area) on a silica substrate (light area). The same imaging techniques on the 800 °C coating, Figure 3.13 (b) and (c), shows a very different image with evidence of complex structures and what appear to be bubble structures. It is thought that a possible explanation for the oxygen rich environment
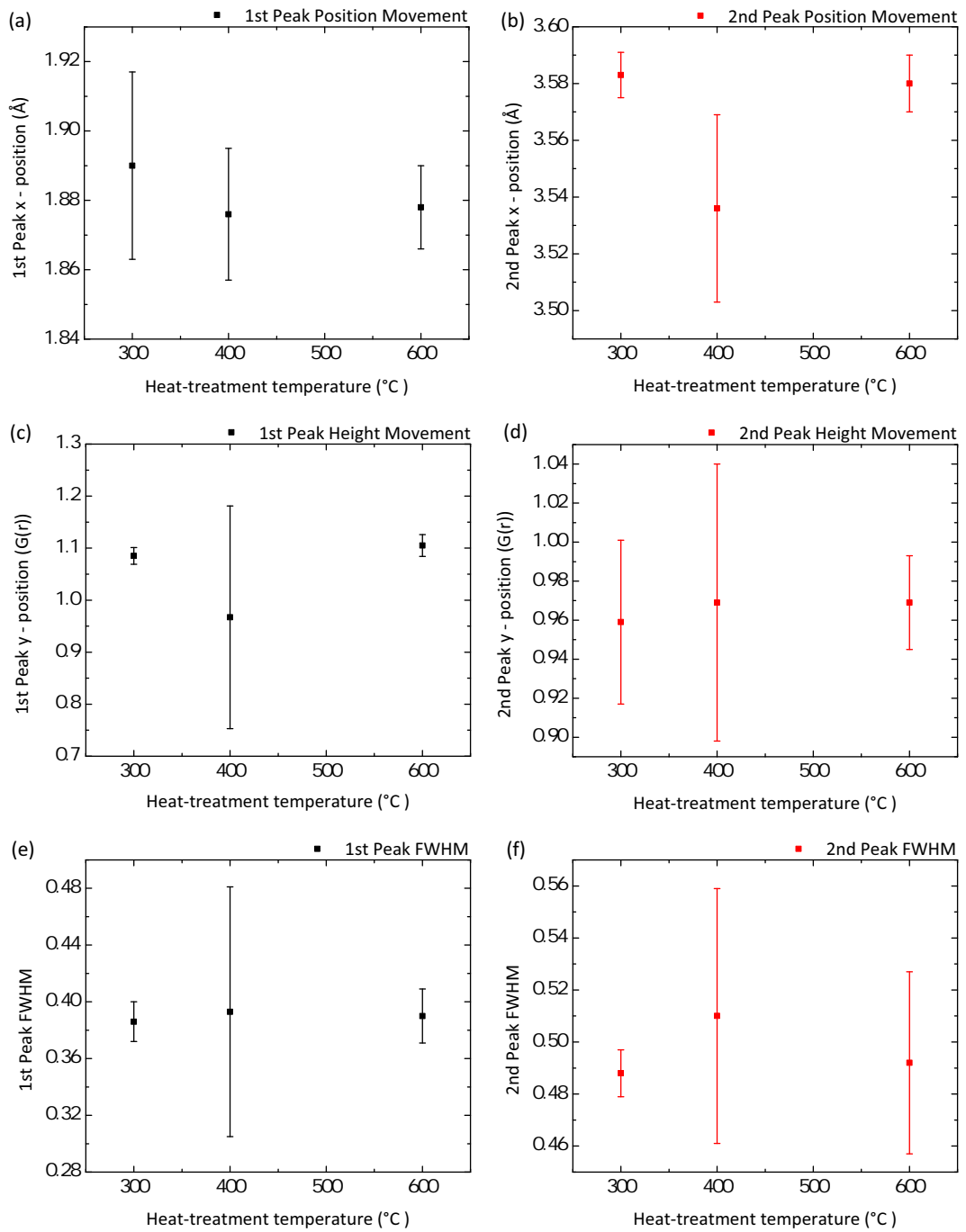
Figure 3.12: *RDF analysis of the CSIRO heat-treated Ta_2O_5 coatings, where the changes in the RDFs against heat-treatment temperature are presented. (a) and (b) show the changes to the 1st and 2nd major peak positions, (c) and (d) show changes in the 1st and 2nd peak height respectively, and (e) and (f) shows the changes in the 1st and 2nd peak full width half maxima respectively.*
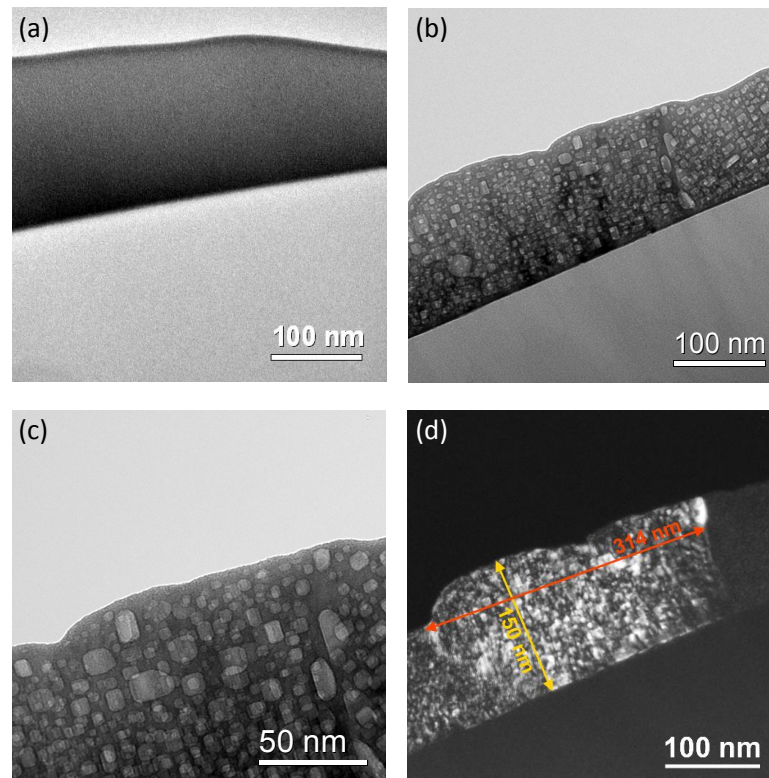
Figure 3.13: (a) shows a TEM bright field image of the amorphous 600°C coating, (b) shows a TEM bright field image of the 800°C coating showing small 'bubble' structures with (c) showing an increased magnification image to highlight these structures, and (d) shows the TEM dark field image highlight the crystalline nature of the material with an overlay of the crystal dimensions in nm.

of the coating is that oxygen has been trapped in the bubble structures as the coating crystallised during heat-treatment, where the coating is placed in an oven in air for 24 hours at 800 °C. The crystallisation of the coating has created a polycrystalline material with large crystals that vary in size from around 100 nm to 500 nm, a typical crystal measuring 314 nm by 150 nm is shown in the dark field image in Figure 3.13 (d).

Referring back to the coating mechanical loss results in Figure 3.2 on Page 71 with the large loss peak at 90 K it is clear to see that the onset of crystallisation could be the cause, where phonon scattering at the crystal grain

boundaries could be responsible for the increase in mechanical loss [132].

3.6 Low water content heat-treated Ta$_2$O$_5$ coatings

ATF [133] produced a series of 'low water content' heat-treated Ta$_2$O$_5$ coatings at 300, 450 and 600 °C. These coatings were deposited on the substrate using an ion-beam-sputtering in a low water content environment and heat-treated in air for 1 hour. The exact details of the coating procedure are not available and are the intellectual property of ATF [133]. The 'low water content' manufacturing process was recommended by ATF as a possible way to increase the coating performance and subsequently reduce its mechanical loss.

Research was therefore carried out on these coatings to measure their mechanical losses and study their atomic structure to look for changes from the previously studied CSIRO coatings. A similar procedure to the cryogenic mechanical loss measurements carried out with the CSIRO coatings was carried out with the ATF low water content coatings.

3.6.1 Mechanical loss measurements

Mechanical loss measurements made at cryogenic temperatures were carried out using the process detailed in Chapter 2. The results shown on Figure 3.14 are the mechanical losses of the coated cantilevers at modes around 1.5 kHz. Figure 3.14 shows the mechanical losses of the coated cantilevers. The loss of the coating was not calculated due to insufficient control sample data (where losses of un-coated cantilevers are subtracted from the losses of the coated cantilevers to extrapolate the loss associated only with the coating). The mechanical loss measurements of the control samples will be the subject of a future investigation.

The 300 °C sample has a broad low temperature loss peak that is centered at around 60 K. As the heat treatment temperature is increased the low tempera-
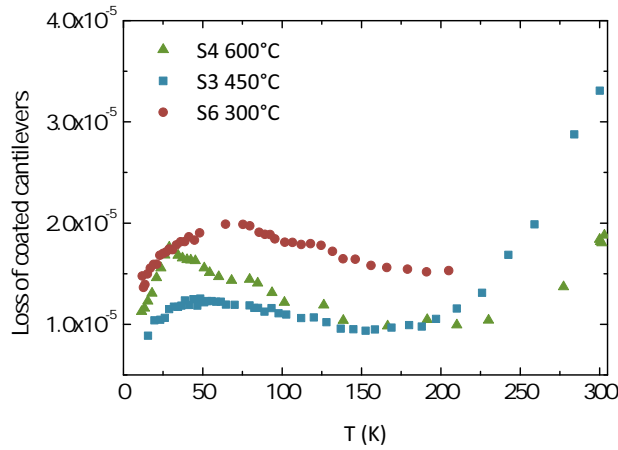
Figure 3.14: *Coated cantilever loss against temperature for the ATF low water content Ta$_2$O$_5$, highlighting the low temperature loss peak positions, for the $\sim$ 1 kHz mode.*

ture loss peak moves down in temperature and becomes slightly more defined, at 450 °C heat-treatment the peak is centered at around 54 K. At 600 °C heat-treatment a much more narrow and more defined peak is present at around 36 K. This pattern is similar to what has been previously investigated in the heat-treated CSIRO Ta$_2$O$_5$, and may be the result of the sample moving into a more ordered state which we shall explore further. A major difference between the CSIRO Ta$_2$O$_5$ and other previously measured heat-treated Ta$_2$O$_5$ is the relative positions and shapes of the low temperature peaks at similar heat-treatment temperatures.

Figure 3.15 shows the clear differences from the CSIRO Ta$_2$O$_5$ to the ATF Ta$_2$O$_5$ coating losses, where the CSIRO coatings have low temperature peaks that are narrower in range and occur at lower temperatures. Figure 3.15(a) shows similar shaped loss peaks for the 300 °C where the ATF loss peak appears broader and occurs at higher temperature, at around 60 K, than the CSIRO loss peak at around 30 K, with a difference of around 30 K between them. Figure 3.15(b) shows a broad loss peak occurring at around 54 K for the ATF coating heat-treated at 450 °C against a more narrow and defined peak at around 30 K for the CSIRO coating heat-treated at 400 °C, with a
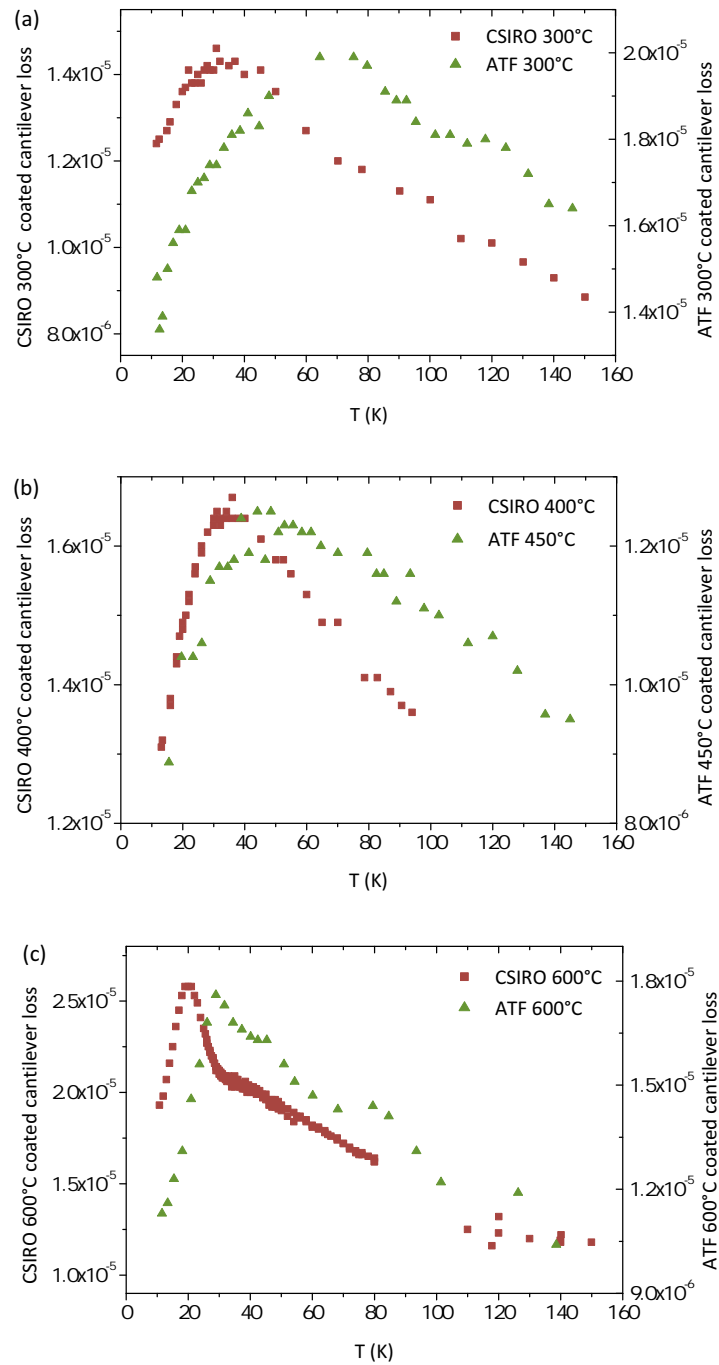
Figure 3.15: *Coated cantilever loss data (a) showing the low temperature loss peak in the 300°C, (b)400/450°C and (c) 600°C coatings for both the CSIRO [126] and ATF low water content Ta$_2$O$_5$ coatings, highlighting the differences in peak positions and shapes between the two types of coatings.*

smaller difference between them of around 20 K. Figure 3.15(c) shows that for the 600 °C loss peak, both the CSIRO and ATF low temperature loss peaks show similar shapes in the onset of the low loss peak, although it appears that the CSIRO peak falls off at a faster rate than the ATF peak, which also has a broader shape as in the case for the 300 °C and 400/450 °C coatings. The 600 °C loss peaks are separated by about 10K from the CSIRO to ATF coatings. It is interesting to note that the difference in low temperature loss peak positions between the CSIRO and ATF coatings decreases as heat-treatment temperature increases.

This gives evidence of significant changes that could possibly be a direct effect of ATF's low water content manufacturing process. This may also be due to the shorter heat-treatment time, where the CSIRO coatings undergo 24 hours of heat treatment compared to ATFs 1 hour. To investigate these differences further it is possible to calculate the activation energies associated with each of the ATF Ta$_2$O$_5$ coatings and compare it to previously measured values for the CSIRO Ta$_2$O$_5$ coatings.

3.6.1.1   Activation Energies

It has previously been shown that the low temperature loss peaks can vary slightly in temperature with frequency [126]. These movements can be attributed through a thermally activated dissipation process that can be described by the Arrhenius equation [132, 134],

$$\tau = \tau_0 e^{E_a/k_B T}, \tag{3.1}$$

where the relaxation time, τ, is characterised by a rate constant, τ_0, and activation energy, E_a. It has been shown that this dissipation process can be associated with the loss peak temperature, T_{peak}, at an angular frequency, ω_0, by,

$$\omega_0 \tau_0 e^{E_a/k_B T_{peak}} = 1, \tag{3.2}$$

which can be expressed as,

$$\ln \omega_0 = \ln \tau_0^{-1} - \frac{E_{\mathrm{a}}}{k_{\mathrm{B}} T_{\mathrm{peak}}}, . \tag{3.3}$$

Therefore from equation 3.3, plotting $\ln \omega_0$ against $1/T_{peak}$ will produce a straight line that will yield the activation energy and rate constant for the dissipation process.

This process was carried out for the ATF Ta$_2$O$_5$ coating and Figure 3.16 shows the resultant Arrhenius plots. Figure 3.16 (a) shows the 300 °C plot for the peak at around 60 K where the activation energy and rate constant, calculated from the linear fit, is (38.98 ± 18.69) meV and $(1.2 \pm 0.27) \times 10^{-7} s$, respectively. Unfortunately there is a rather large error attributed to the 300 °C results because of difficulties associated with the specific geometry of the cantilever causing coupling between torsional and bending modes, which reduced the ability to effectively measure changes in motion at the all of the resonant modes. For the 450 °C and 600 °C coatings the activation energies were (34.31 ± 9.19) meV and (33.02 ± 4.77) meV, respectively, with rate constants of $(1.17 \pm 0.15) \times 10^{-7}$ s and $(1.1 \pm 0.09) \times 10^{-8}$ s, respectively, as calculated from their Arrhenius plots (Figure 3.16 (b) and (c)).

Previous studies of the CSIRO heat-treated Ta$_2$O$_5$ coatings show similar results for the activation energy of the 600 °C coating, at (35.6 ± 2.5) meV [126]. However the activation energies vary greatly at lower temperature heat treatments, where the CSIRO 300 °C has an activation energy of (66 ± 10) meV. The large change of activation energies associated with the heat-treated CSIRO samples has also been seen in other measurements of heat-treated ion-beam sputtered Ta$_2$O$_5$ manufactured by LMA [135]. It is therefore very interesting to note that, in the case for the ATF Ta$_2$O$_5$ even with the large error associated with the 300 °C ATF Ta$_2$O$_5$, the activation energies from the 300, 450 and 600 °C coatings show a relatively flat trend with only minimal changes between their averages.
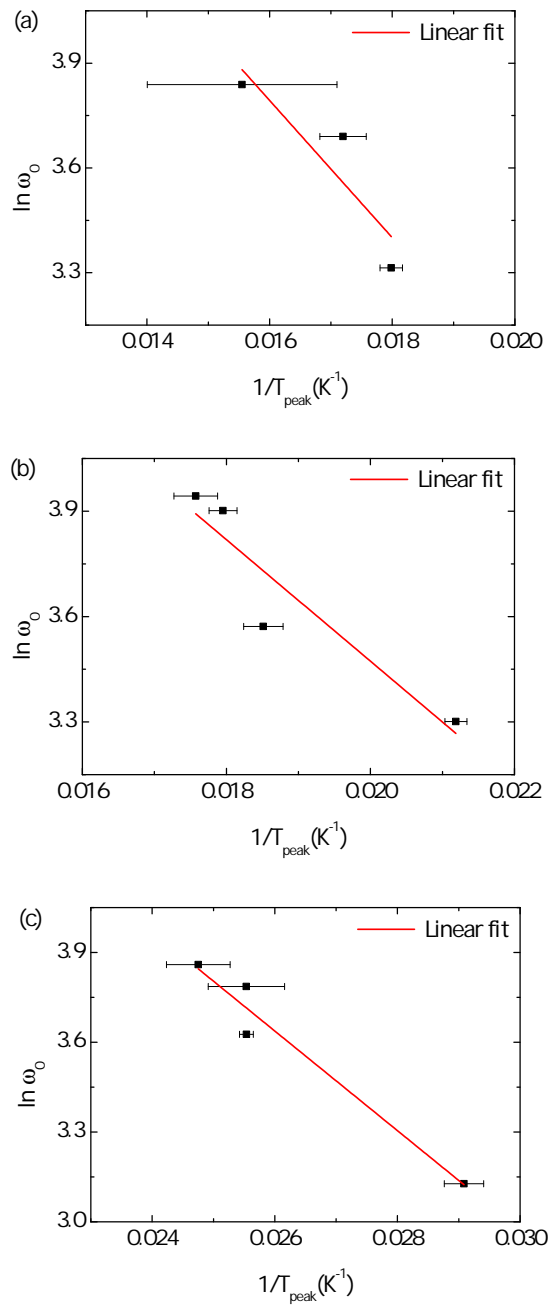
Figure 3.16: *Arrhenius plots for the low temperature loss peaks of the (a)300, (b) 400 and (c) 600 °C ATF low water content coatings*

3.6.2   Atomic structure and chemistry investigations

EELS spectra were taken and Figure 3.17 shows the resultant stoichiometries. The low water content coatings appear to be oxygen deficient and variation
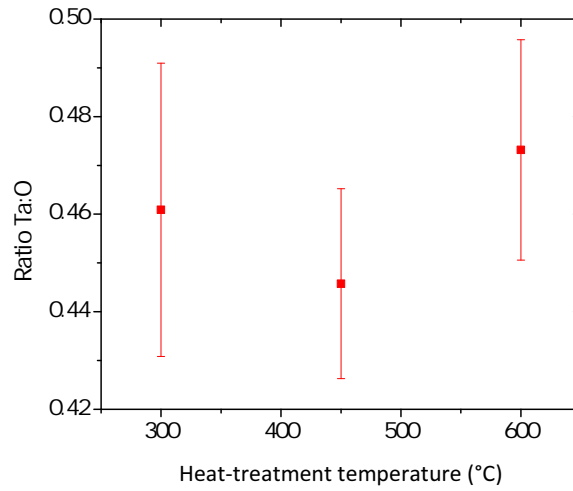
Figure 3.17: *The ratios of Ta:O in the ATF low water content heat-treated Ta$_2$O$_5$ coatings taken from EELS stoichiometry data. A ratio of Ta:O of 0.4:1 would give exactly Ta$_2$O$_5$.*

between the coatings lies within error, although the 600 °C coating appears to be slightly more oxygen deficient than the others. These EELS stoichiometries were then used as input parameters for the calculating the RDFs.
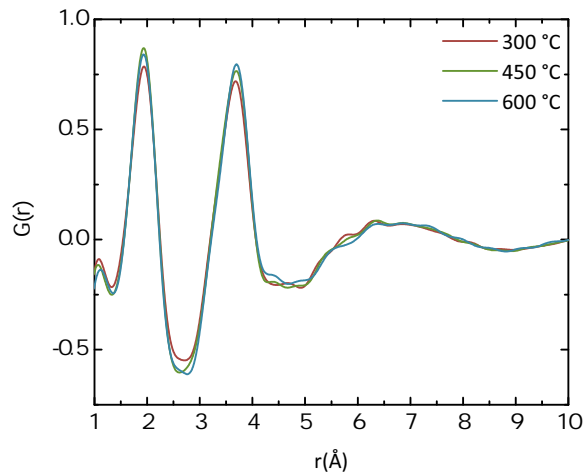
Figure 3.18: *The averaged RDFs of the the ATF low water content heat-treated Ta$_2$O$_5$ coatings, showing subtle differences between them.*

The RDF measurements were carried out following the procedures described in Chapter 2, Section 2.4.7, and the resultant averaged RDFs for each

each heat-treated coating are shown in Figure 3.18. Similar changes to the CSIRO heat-treated Ta$_2$O$_5$ are present in the ATF Ta$_2$O$_5$ coatings in case of the second peak where Ta-Ta distances dominate; as heat treatment temperature rises the second peak becomes more dominant, suggesting an increase in order for the Ta-Ta distances. The first peak however shows a slightly different pattern with the 450 °C showing the highest peak. The changes are subtle and it is important to consider the error associated in the RDFs.

As in the case with the CSIRO coatings, the most important aspects of the averaged RDFs are tracked between the coatings, including the standard deviation error carried through from the errors in the individual RDFs, and are shown in Figure 3.19. Most of the changes between the RDFs lie within error, however the second position and height (Figure 3.19 (b) and (c)) show an increasing trend with heat-treatment temperature, highlighting the increasing Ta-Ta distances as is apparent from Figure 3.18. The second peak full-width-half-maximum (Figure 3.19 (f)) also shows a slight decrease in the 600 °C giving rise to a slightly more ordered state.

3.7 MLD Ta$_2$O$_5$ heat-treated coatings

Another set of ion-beam sputtered Ta$_2$O$_5$ coatings was prepared by MLD [136] which included a sample that had undergone no heat-treatment and also a sample heat-treated to 600 °C in air for 24 hours. These coatings had a thickness of 1 μm. Previous atomic structure investigations of heat-treated Ta$_2$O$_5$ coatings have given rise to only minimal changes in the average atomic structure and, as shown in the case for the CSIRO coatings, larger changes in the local sample areas. In the case of heat-treatment it may be possible that the temperature difference across the thickness of the coating from the surface to the substrate as the sample undergoes heat treatment causes changes in the average atomic structure from the coating surface to the substrate. Therefore, an investigation was made into identifying systematic variations in the atomic
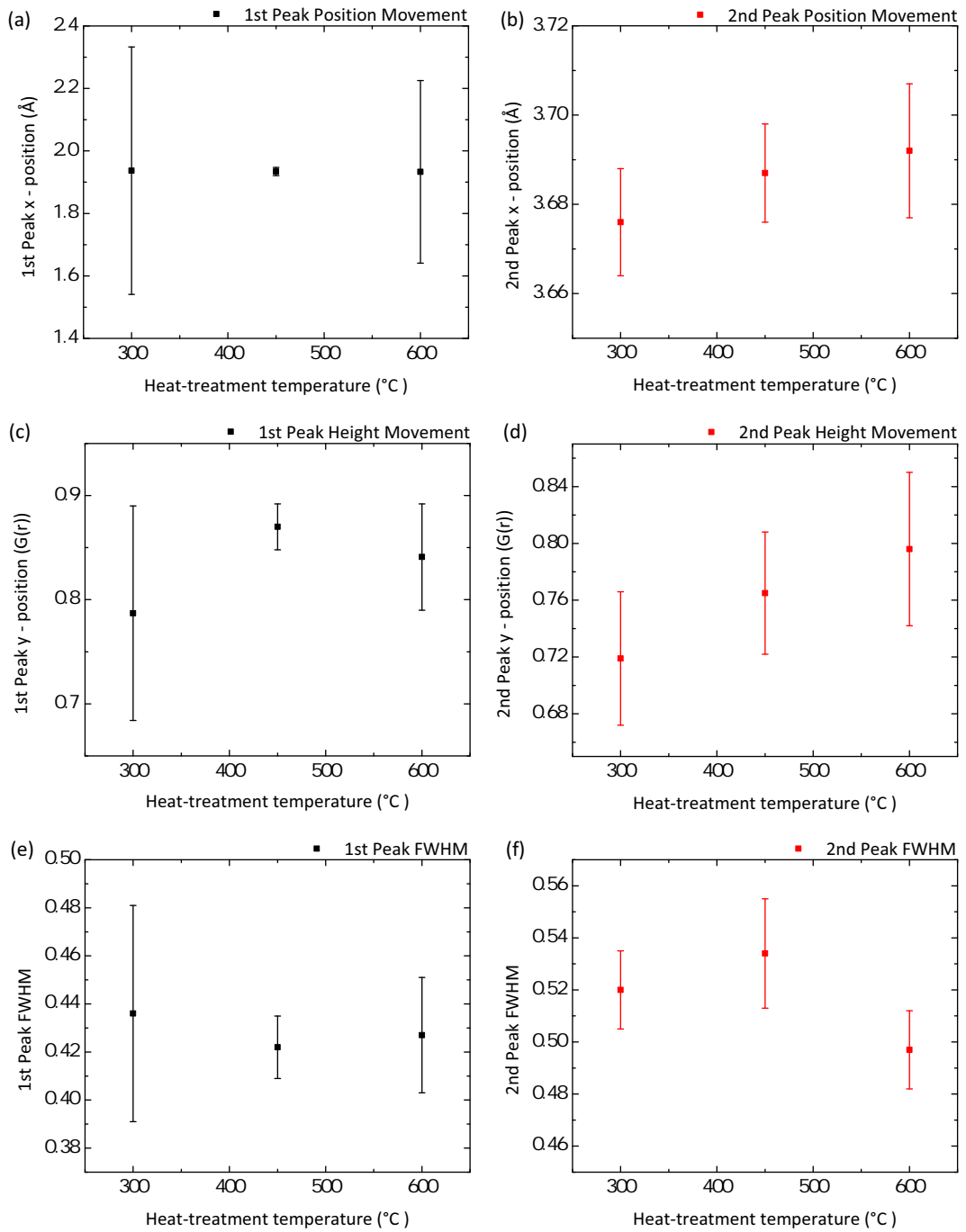
Figure 3.19: *RDF analysis of the ATF low water content heat-treated Ta$_2$O$_5$ coatings, where the changes in the RDFs against heat-treatment temperature are presented. (a) and (b) show the changes to the 1st and 2nd major peak positions, (c) and (d) show changes in the 1st and 2nd peak height respectively, and (e) and (f) shows the changes in the 1st and 2nd peak full width half maxima respectively.*

structure by collecting the RDFs from the coating surface to the substrate. This was also made possible due to the increased thickness of this coating.

3.7.1 Atomic structure and chemistry investigations using area mapping

RDFs were collected by mapping the area in the coating where the diffraction data used to calculate the RDFs was taken.
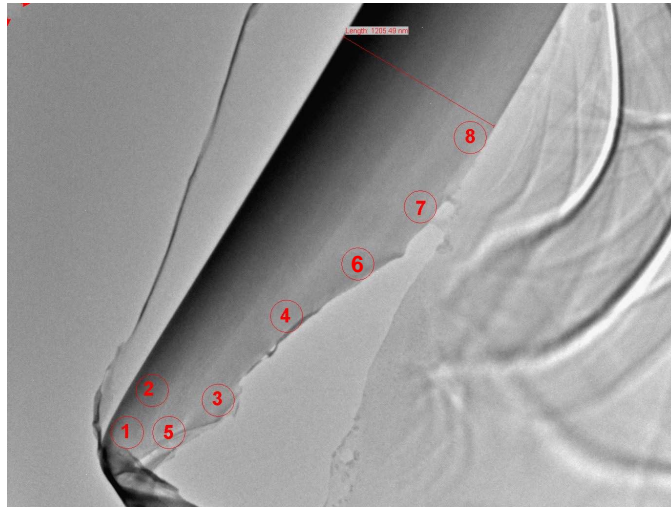
Figure 3.20: *TEM bright field image showing the non-heat-treated MLD coating, highlighting the selected areas where electron diffraction data was taken from. Area 1 is the closest to the coating surface, and area 8 is closest to the Si substrate*

Figure 3.20 shows the map of collection areas for the diffraction data taken from the non-heat-treated coating. Each mapped area has a large radius of 200 nm, where a beam diameter of 50 nm was used to collect the diffraction data, ensuring that diffraction data was collected within the mapped areas. Area 1 starts at the surface of the coating going to area 8 near the bulk of the coating. A similar area mapping procedure was also carried out on the 600 °C heat-treated coating. Five diffraction patterns were collected for each area, and the RDFs were calculated and analysed.
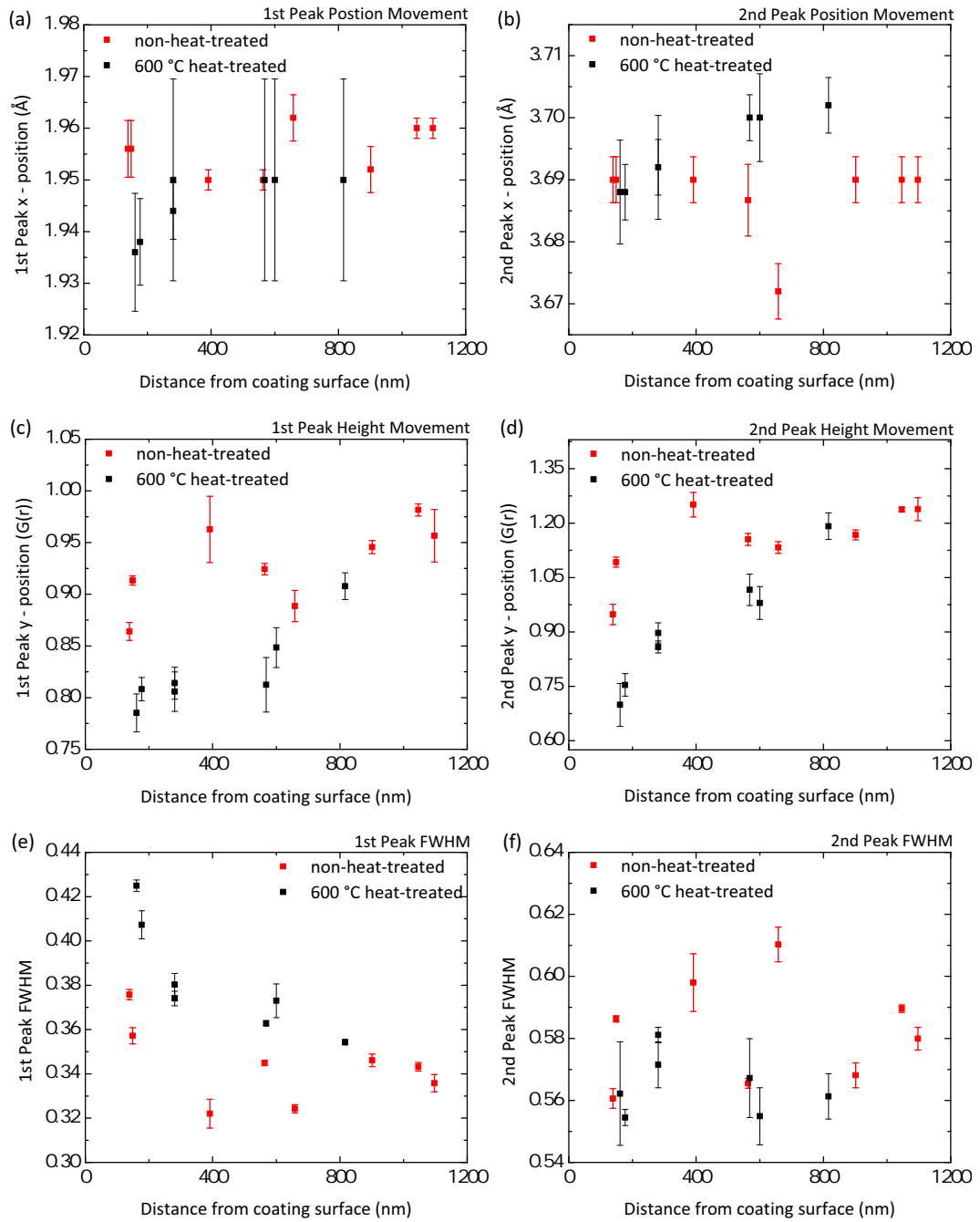
Figure 3.21: *RDF analysis of the MLD heat-treated Ta$_2$O$_5$ coatings, where the changes in the RDFs against depth into the coating are presented. (a) and (b) show the changes to the 1st and 2nd major peak positions, (c) and (d) show changes in the 1st and 2nd peak height respectively, and (e) and (f) shows the changes in the 1st and 2nd peak full width half maxima respectively.*

Figure 3.21 shows the complete analysis, tracking changes in the RDFs which include first and second peak heights, positions and full width half maxima. The data shown here present the first evidence that systematic changes may be taking place in the atomic structure across the depth of the coating, where the coating surface appears more ordered than the coating closest to the substrate. Figure 3.21 (a) shows that there is little measurable movement of the 1st peak position, which is related mainly to Ta-O distances, for both the non-heat-treated and 600 °C heat-treated coating. However, Figure 3.21 (c) does show changes, with significant scatter for the non-heat-treated coating and a generally increasing trend for the for the 600 °C heat-treated coating. Figures 3.21 (b) and (d) show the second peak position and height, which relates to the Ta-Ta and longer range Ta-O distances. This shows an a flat trend with significant scatter for the non-heat-treated coating. The 600 °C coating shows a general increasing trend for both the second peak position and height. Figures 3.21 (e) and (f) show significant scatter for the full width at half maxima (FWHM) of the 1st and 2nd peaks for both coatings, although the first peak for the 600 °C coating shows more of decreasing trend with increasing coating depth.

In general there is more scatter in the non-heat-treated coating making it difficult to identify any clearly changing trends in the atomic structure. The 600 °C sample does appear to show identifiable trends that suggest that the coating becomes more ordered closer to the substrate, as the first and second peak heights increase and the FWHM of the first peak decreases.

Problems that occurred while measuring these coatings, explained further in the next section, made it difficult to interpret the RDFs due to large noise peaks, and it is therefore not clear that these are accurate trends. However as a first attempt it shows a promising method to further identify changes in the atomic structure of these coatings, by collecting data through the depth of the coating. It is therefore important that future investigations of heat-treated

coatings include the analysis of this area mapping method to prove that these results are repeatable and show consistent changes. The addition of modelling the separate regions will give the best possible understanding of the atomic structure changes that take place with heat-treatment.

3.8 Conclusions

It has been shown that using temperature as a probe of mechanical loss in these Ta_2O_5 coatings produces valuable insights into the mechanisms for mechanical loss. Heat-treating Ta_2O_5 coatings causes changes in the mechanical loss observed at low temperature, with loss peaks arising in the region of 10s K which increase in magnitude and become more defined as the heat-treatment temperature rises, but decrease in temperature. This remains true until crystallisation, where in the case for the 800 °C crystallised coating a larger broad loss peak occurs at 90 K.

Changes in manufacturing deposition methods between the coating manufacturers affect the mechanical loss and atomic structure of the coatings, where it was shown that using a low water content manufacturing processes significantly changes the positions of the low temperature loss peaks, both broadening and pushing the peak position up in temperature, and also reduces the variances in the activation energies over heat-treatment temperatures.

For the CSIRO heat-treated coatings, it has also been shown that heat-treatment produces subtle changes to the averaged local atomic structures. The general trend shows that as heat-treatment temperature increases the coatings becomes more ordered, moving towards crystallisation between the 300-600 °C coatings and crystallising at 800 °C. Accurate atomic models based on experimental diffraction data of these coatings show stable structures, that show Ta_2O_2 ring fragments which were found to be features present in the crystalline phase of the material. The models show that these crystalline building blocks are randomly oriented and reproduced in the coating structures over a

long range, giving rise to the amorphous nature of the material. The Ta_2O_2 ring fragments also appear to increasing in population as heat-treatment temperature rises, as the coating becomes more ordered, and they also appear to stretch slightly with increased Ta-O-Ta angles. There also appear to be fewer Ta-Ta and more Ta-O bonds present as heat-treatment temperature is increased. The observed changes of increased ordering, presence of the Ta_2O_2 ring fragments and less Ta-Ta bonds are the major observable changes.

Further improving methods in the experimental procedures for taking the diffraction data will result in better fitting RDFs, and therefore give a more accurate interpretation of the atomic structure. Using experimental stoichiometries from EELS is an important method to increase the accuracy of the measured atomic structure. Area mapping, where electron diffraction data is taken from different area provides a promising way for more accurately identifying changes in the atomic structure with heat-treatment, by looking for systematic changes from the surface of the coating to the point where it joins the substrate. Initial investigations show that these changes are visible and that increasing heat-treatment temperature causes more ordered coating material closest to the substrate, compared with areas of coating near the coating surface.

Chapter 4

Investigations into the material properties of Ta_2O_5 mirror coatings doped with TiO_2

4.1 Introduction

The second generation of detectors, such as Advanced LIGO, will use multi-layer Ta_2O_5 coatings that are doped with TiO_2. The coating manufacturer LMA [135] first suggested doping Ta_2O_5 with TiO_2 as a possible alternative coating material to pure Ta_2O_5. TiO_2 as a dopant has the benefit of Ti ions being a similar size to Ta ions, and also Ti-O and Ta-O bonds are similar in length, and is therefore able to act as a simple substitutional alloying element in a Ta_2O_5 system. It was also found that the melting point of TiO_2/Ta_2O_5 alloys was relatively high [137]. The combination of these factors gave a strong case for studying Ta_2O_5 coatings doped with TiO_2 as they would have a stable amorphous structure and possibly give a high quality alternative to Ta_2O_5 coatings.

The coatings studied in this chapter are multi-layer coatings with 30 alternating layers of $\lambda/4$ (at 1.064 μm) thick SiO_2 and Ta_2O_5 doped with TiO_2, and manufactured by LMA [135]. The doping concentrations were 0, 8.3, 20.4, 25.7, 28.3, 53.8 % (cation) TiO_2 as determined from EELS stoichiometry mea-

surements. LMA has a number of coating chambers and the $0, 8.3, 20.4, 28.3$ %
doped coatings were deposited in a coating chamber smaller than the coating
chamber used to deposit the 25.7 and 53.8 % doped coatings. These coatings
were deposited using ion-beam sputtering and also heat-treated at 600 °C for
24 hours.

It should be noted that the data presented in this chapter expresses the
level of TiO_2 doping as a TiO_2 cation percentage, thus for simplicity, TiO_2
doping is denoted simply as Ti doping. The coatings will also be labelled by
the percentage of Ti (cation percent) doping i.e., the Ta_2O_5 doped with 20.4%
TiO_2 coating is denoted as the 20.4% Ti coating.
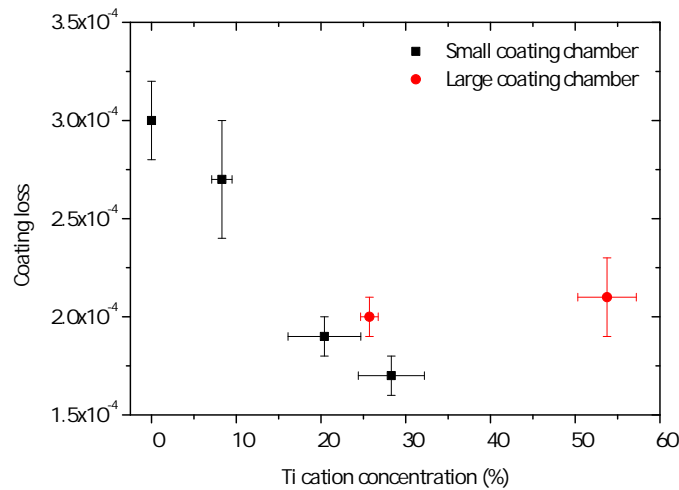
Figure 4.1: *Mechanical loss measurements made at room temperature are shown
against various concentrations of Ti doping, for the doped Ta_2O_5 coat-
ings [138].*

Coating mechanical loss measurements were previously made at room tem-
perature for each of the Ti doping concentrations, and the results are shown
in Figure 4.1 [138]. The Ti doping concentrations were measured using EELS
stoichiometry (see Chapter 2, Section 2.4.6.2). As these are multi-layer coat-
ing mechanical loss measurements, the mechanical loss values include the loss
associated with the SiO_2 component, as well as the Ta_2O_5 doped with TiO_2.
However, any changes in the mechanical loss can be assumed to be the result of

the changes to the TiO_2 doping concentration as this is the only variable during the manufacturing process, although extraction of the Ta_2O_5 doped with TiO_2 coating component would be preferable for future and more detailed investigations.

The results clearly show that as Ti doping increases, the mechanical loss decreases until it reaches a minimum for the 28.3% Ti coating, it then increases again for the 53.8% Ti coating. There is a roughly 40% drop in mechanical loss from its highest point at 0% Ti doping to the lowest point at 28.3% Ti doping. This change suggests that changes in the coating structure give rise to the observed changes in mechanical loss. It is therefore important to study any changes in the atomic structure of these coatings in an attempt to understand the observed changes in mechanical loss.

4.2 Atomic structure and chemistry investigations

4.2.1 RDF measurements

In order to investigate any possible changes in the atomic structure of these coatings the local atomic structure was investigated using RDF measurements, following the process described in Chapter 2.

The averaged RDFs for the doped Ta_2O_5 coatings are shown in Figure 4.2, where each RDF is the average of at least 10 RDFs from diffraction data collected from different locations in each coating. Figure 4.2 (a) very clearly shows a varying RDF structure, meaning that the short-range atomic structure is noticeably changing as the Ti doping concentration increases. This change is highlighted in Figure 4.2 (b) where only the RDFs of the 0% and 53.8% Ti doped coatings are shown. Here, it can clearly be seen that the first major peak at around 2 Å, which from comparison to interatomic distances from crystalline data is probably from to Ta-O and Ti-O distances, or simply metal-oxygen
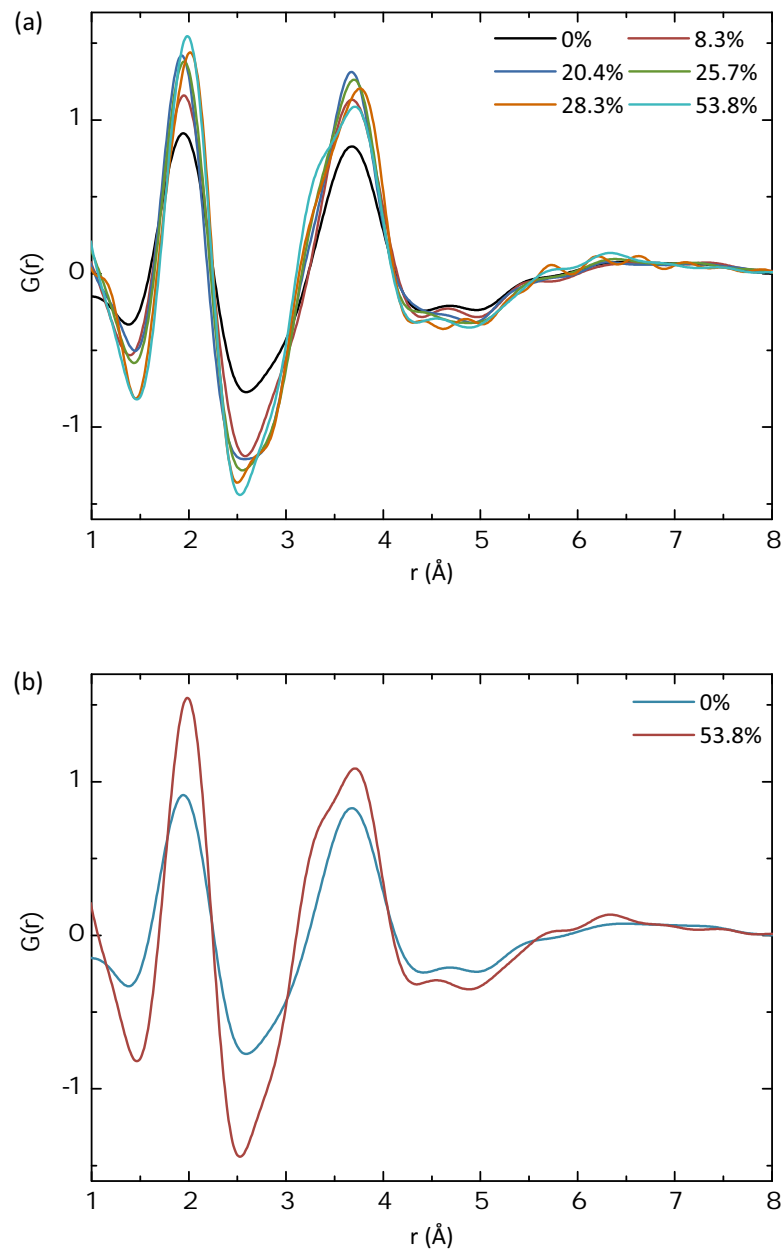
Figure 4.2: *Experimental RDFs for the Ta_2O_5 doped with TiO_2 coatings for (a) the full range of Ti doping levels, and (b) only the 0% and 53.8% Ti coatings*

distances, increases in height and decreases in width indicating increased order in these distances as Ti doping concentration increases. The second peak shows increased height but also a change in shape, which may indicate an increased order from the distances present in this peak, likely to be Ta-Ta, as well as Ta-

Ti and Ti-Ti where Ti doping is present or more simply metal-metal distances.

The observed changes in the RDFs are highlighted by tracking the most important changes between the average RDF for each Ti doped coating (as previously described in Chapter 3, Section 3.4.2) where, excluding any data below 1 Å regarded as noise, the first and second major peak positions, heights and full width at half maxima (FWHMs) are measured and shown in Figure 4.3. Figure 4.3 (a) and (b) highlight the changes in the position (r(Å)) of the first peak and second peaks, respectively, and show that the first peak position moves from a minimum at 20.4% Ti doping to a maximum at 28.3% Ti doping, and the second peak has a minimum at 8.3% and a similar maximum at 28.3% Ti doping. Interestingly, both the first and second peak positions show similar patterns of change with increasing Ti doping, both with maximum values for the 28.3% Ti coating, indicating that the metal-oxygen and metal-metal distances are furthest apart at the 28.3% Ti coating. Figure 4.3 (c) shows that the first peak height (G(r)) has a generally increasing trend as Ti doping increases, indicating an increasing probability of finding the nearest neighbour distances of Ta-O or Ti-O at the peak maximum. This is further supported by evidence that the peaks are becoming narrower as Ti doping increases, as shown when examining the FWHM of the peak (Figure 4.3 (e)), indicating a decrease in distance distribution. Figure 4.3 (d) shows that the second peak height increases from 0% Ti doping until a maximum at around 20% Ti doping and then decreases with increasing Ti doping. At the same time, Figure 4.3 (f) shows that the peak width increases with increasing Ti doping. This change in shape is likely due to the increased variety of interactions that make up the second peak from Ta-Ta and Ta-Ti or Ti-Ti when Ti doping is present. This will be discussed further when examining the atomic models in Section 4.2.2.2, where it will be shown that Ta-Ti distances are shorter than Ta-Ta distances giving an explanation for the widening of the second peak. The second peak appears to be at the most ordered state, with a minimal distance distribution
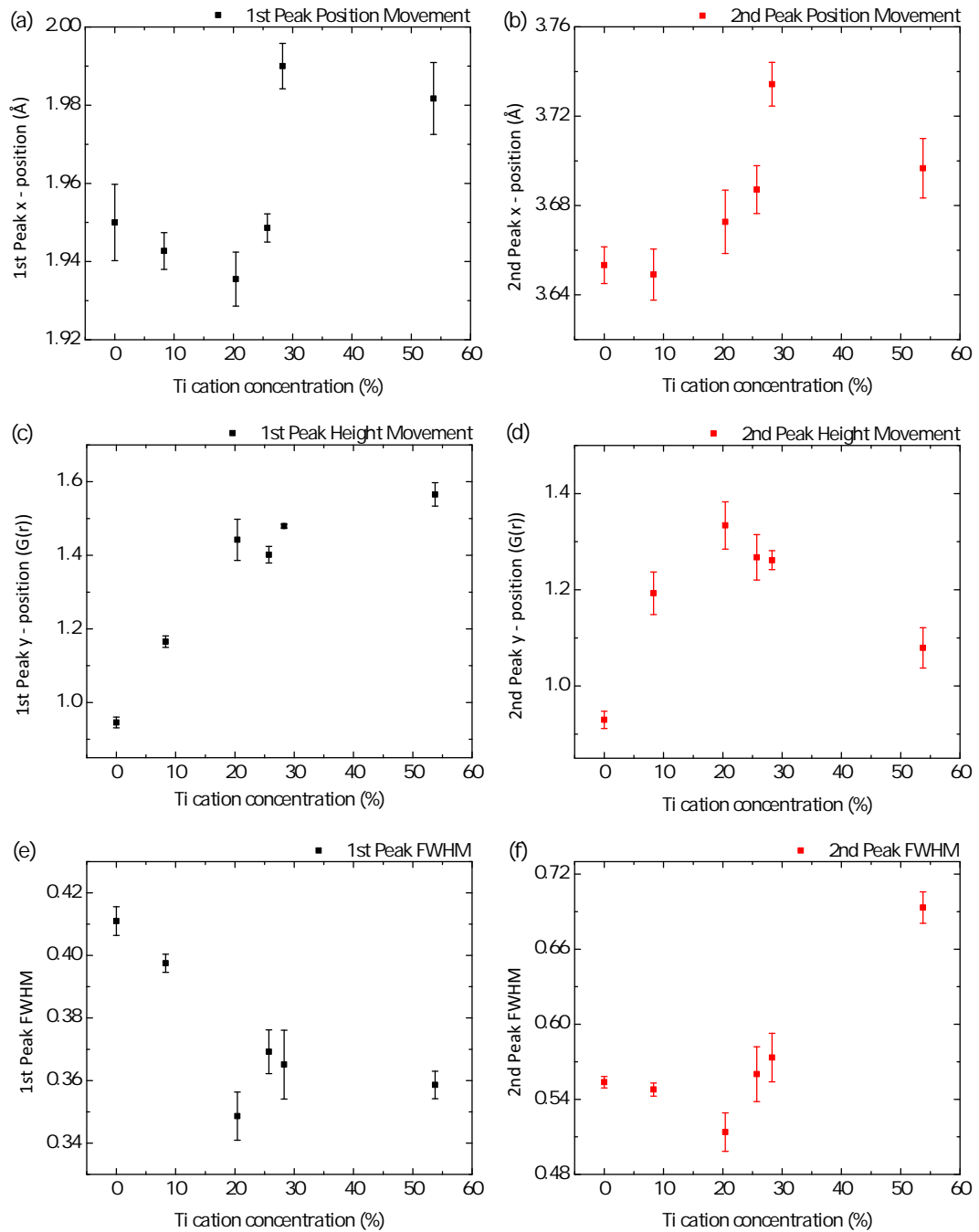
Figure 4.3: *RDF analysis of the doped Ta_2O_5, where the changes in the RDFs against depth into the coating are presented. (a) and (b) show the changes to the 1st and 2nd major peak positions, (c) and (d) show changes in the 1st and 2nd peak height respectively, and (e) and (f) shows the changes in the 1st and 2nd peak full width half maxima respectively.*

for the 20.4% Ti coating because the peak position is at its maximum and width is at its minimum.

4.2.2 Atomic models of the 20.4% and 53.8% Ti doped coatings

To further investigate the observed changes in the RDFs it is necessary to create atomic models. Atomic models were created for 20.4% and 53.8% Ti doped Ta_2O_5 coatings, following a similar procedure to that discussed in Chapter 2, Section 2.4.7. These concentrations of Ti doping were chosen because they were the only doped Ta_2O_5 coatings to have experimentally measured densities at the time of creating the models, which were 7.01 g/cm^3 [139] for 20.4% Ti doped coating and 5.50 g/cm^3 [140] for the 53.8% Ti doped coating. Experimental stoichiometries measured from EELS data were also used as inputs to these models, and are shown in Table 4.1.

Coating	Stoichiometry (Ta:Ti:O)
20.4% Ti	0.26:0.06:0.68
53.8% Ti	0.17:0.20:0.63

Table 4.1: *EELS stoichiometries for the 20.4% and 53.8% Ti doped Ta$_2$O$_5$ coatings*

There is very little literature on crystalline structures of tantalates having a TiO_2 component. However, one study described Ta-O and Ti-O bonds to have very similar bond distances in crystalline material, and that Ti atoms can be generally thought of a replacing Ta atoms in a crystalline structure [141]. Therefore, Ti atoms were given identical constraints to Ta atoms on positions relative to other Ti, Ta or O atoms in the model, for the purposes of the RMC refinement process.
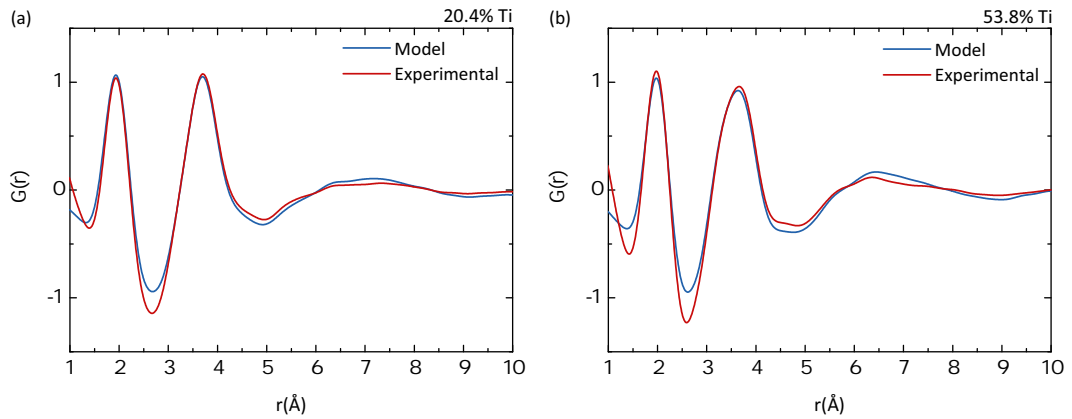
Figure 4.4: *Reduced density functions for the doped Ta_2O_5 coatings comparing the experimentally measured RDFs to the refined model RDFs for (a) the 20.4% Ti coating, and (b) the 53.8% Ti coating.*

4.2.2.1 DFT and refined model comparisons

Figure 4.4 shows the generally good agreement achieved between RDFs generated from the final refined models to the experimental RDFs for both the 20.4% and 53.8% Ti doped models. As with the heat-treated series 400 °C Ta_2O_5 coating in Chapter 3, the final refined (DFT + RMC) models were then compared to the DFT models in order to ensure the final atomic structure was viable.
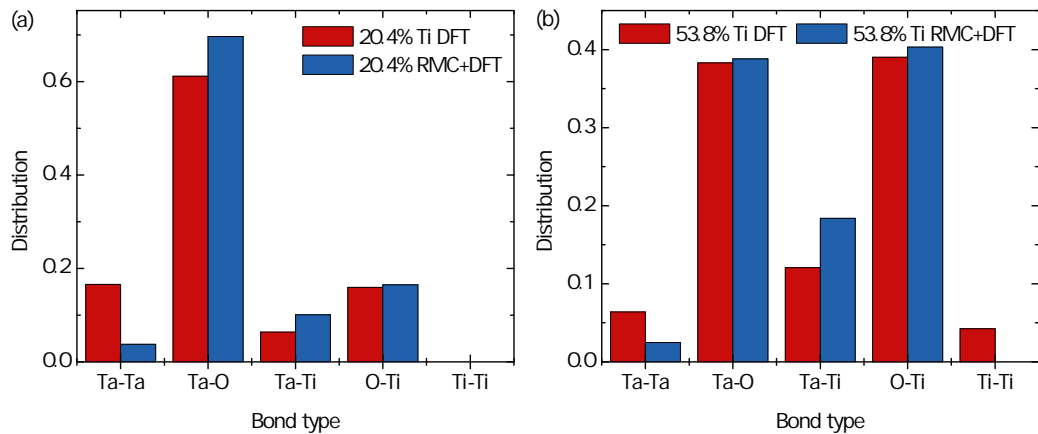
Figure 4.5: *Bond type distributions comparing the DFT model and the refined (RMC+DFT) models for (a) the 20.4% Ti coating, and (b) the 53.8% Ti coating.*

Bond distributions were studied between the DFT model and final refined model to compare differences in the structures, where as before a bond is defined as an atom to atom distance of less than the sum of their covalent radii (Ta = 1.7 Å [129], Ti = 1.6 Å [129], O = 0.73 Å [130]) plus a bond tolerance factor set at 0.1 Å. Figure 4.5 (a) shows the distribution of the bond types in the 20.4% Ti coating and shows only a slight change in the distribution, most notably in the Ta-Ta bonds and the Ta-O bonds. No Ti-Ti bonds where found in the 20.4% Ti models.

Similar comparison between the refined model and DFT model for the 53.8 % Ti model are shown in Figure 4.5 (b). The largest change in bond type distribution is for the Ta-Ti bonds, where there is an increase in their distribution between the DFT and refined models. Overall, the distribution appears to be consistent between the DFT and refined model. There were also a small number of Ti-Ti bonds found in the 53.8% Ti DFT model, which did not exist in the final refined model.

The bond angle and bond angle type distributions were also generated from the models and shown in Figure 4.6. Figure 4.6 (a) shows the bond angle type distribution comparison between the DFT and refined models for the 20.4% Ti coating. The largest differences are between the O-Ta-O and the Ta-Ta-O bond angle types, both of which are important for the structure of the Ta_2O_2 ring fragments, as previously discovered in the CSIRO heat-treated coatings. The O-Ta-O bond angle type represents a smaller fraction of bond fragments in the DFT model compared to the refined model and the Ta-Ta-O represents a larger fraction of bond fragments in the DFT model compared to the refined model. Although the Ta_2O_2 ring fragments are prominent in both models, there appears to be a reduction in the Ta-Ta bonds that relates to a large reduction in the Ta-Ta-O bond angles from the DFT to refined models. This may be an indication of a possible over estimation of the Ta_2O_2 ring fragments in the DFT model. Figure 4.6 (b) shows a similar comparison for the 53.8%
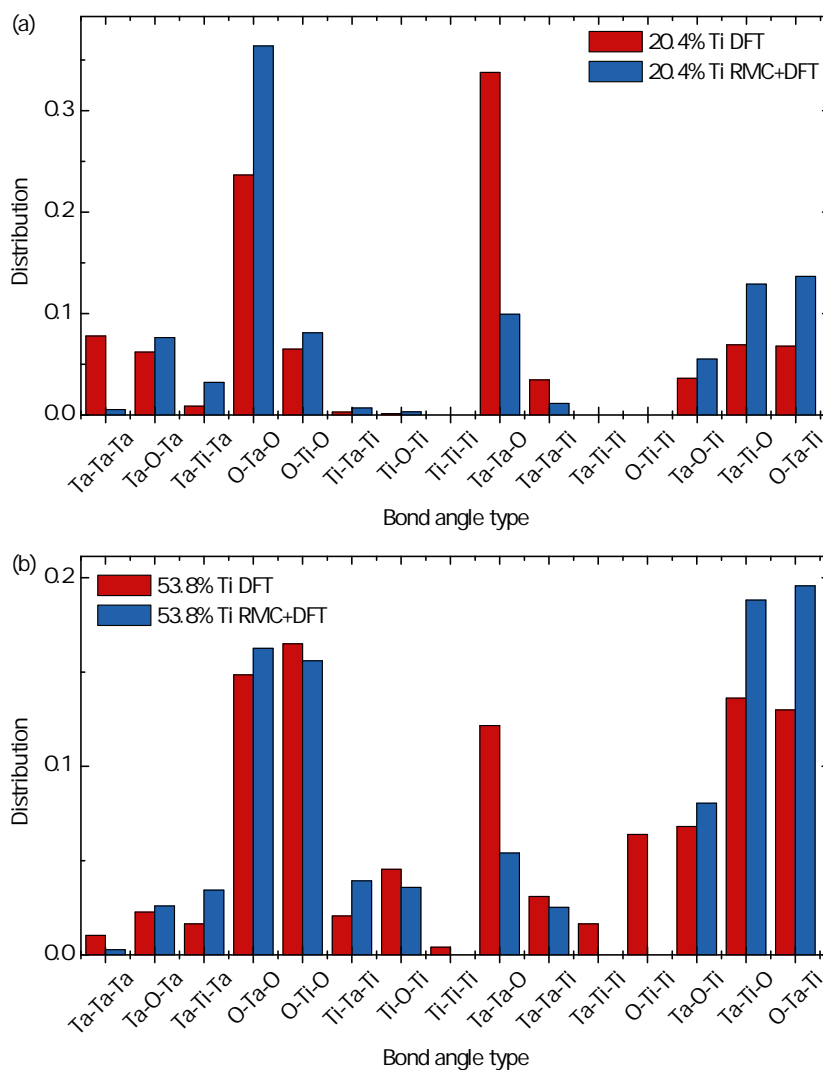
Figure 4.6: *Bond angle type distributions comparing the DFT model and the refined (RMC+DFT) models for (a) the 20.4% Ti coating, and (b) the 53.8% Ti coating.*

Ti coating, which shows a generally good agreement, with the largest changes between the Ta-Ta-O, the Ta-Ti-O and the O-Ti-Ta bonds.

As discussed in Chapter 2 the refined model is generated from creating 27 randomly orientated DFT models, which is then RMC refined to the experimental RDFs. Ideally there would be very little change between the average bond structures. However even though the atom movement is restricted for each iteration to 0.01 Å during the refinement process, some movement is in-

evitable where atoms are moved to avoid any unphysical differences and also to ensure the best agreement with the experimental data. These changes in the bond angle type suggest that there may be a need to improve the molecular dynamics simulations used to generate the DFT model, this will be discussed further in Chapter 6.
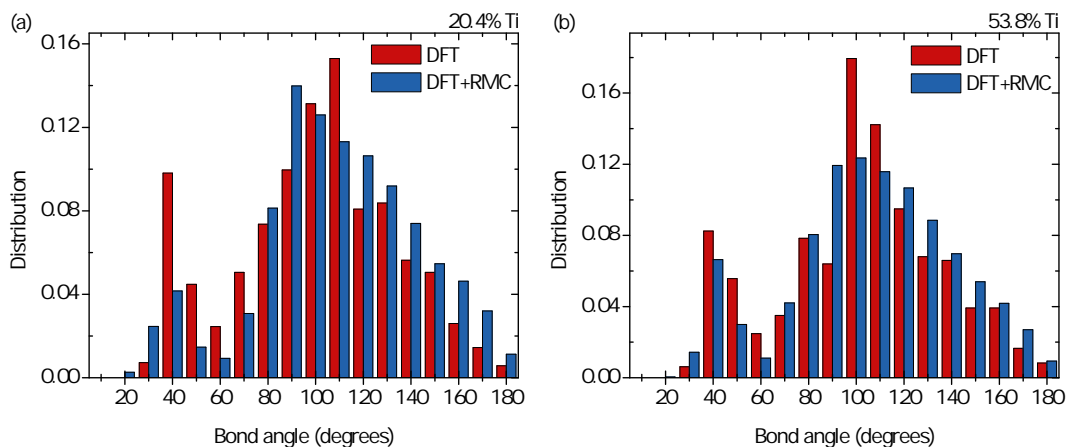
Figure 4.7: *Average bond angle distributions comparing the DFT model and the refined (RMC+DFT) models for (a) the 20.4% Ti coating, and (b) the 53.8% Ti coating.*

The average bond angle distribution of all the bond angle types for the DFT and refined models for the 20.4% and 53.8% Ti coatings are shown in Figure 4.7 (a) and (b) respectively. They show that in general the average bond angle distributions are in good agreement between the DFT and refined models. The largest difference in the 20.4% Ti models is around 40 °, where there appears to be an over estimation of these bond angles in the DFT model (Figure 4.7 (a)). For the 50.8% model the largest difference is around 100 ° where the large spike in bond angles at this angle in the DFT model appears to spread over a range of angles more evenly in the refined model (Figure 4.7 (b)). In general the average bond angle distributions are in good agreement between the DFT and refined models with the refined models showing a more spread out distribution, which is reasonable given the increased size of the model.

The comparison between the DFT models and the refined models show

that there are some differences between their average structures, most notably when looking at the bond type distributions. However these changes are not large enough to cause concern about the validity of the refined models and in general there is a sufficient agreement between them. Also, the addition of the Ti into the structure makes the system much more complex and it is therefore more difficult to get a perfectly fitting system, especially from the DFT stage. Further refinement is possible for these models to get a closer match with the experimental RDFs, although it is expected that it will only change the features seen in the current refined models by a very small amount. At this stage it is reasonable to assume that the refined models give a good representation of the amorphous structure of these coatings, although there is room for some future improvements to be made.

4.2.2.2 20.4% and 53.8% Ti doped Ta$_2$O$_5$ coating model comparisons

This section compares the two final refined models for the 20.4% and 53.8% Ti doped Ta$_2$O$_5$ coatings. Figure 4.8 shows the partial RDFs for the for the 20.4% and 53.8% Ti doped coatings, where RDFs are created from the model based on only two atom pairs i.e., Ta-Ta, Ta-O, Ti-Ta, O-O, Ti-O and Ti-Ti. The addition of all of these atom pair RDFs for each coating would result in the full RDF of the models. The partial RDF relates to interatomic distances and not bonds, as there are no defined bond parameters at this stage. Figure 4.8 (a) shows that, for the 20.4% Ti coating, the first major peak occurring at around 2 Å in the RDF is comprised of metal to oxygen distances that is dominated with Ta-O distances with a small contribution from Ti-O distances. There is then a small contribution from O-O distances at around 2.7 Å. In the region of 3 to 4.5 Å, metal to metal distances are dominant with a significant contribution from Ti-Ta distances and the largest contribution from Ta-Ta distances. There is also a very small contribution from Ti-Ti distances at around 3.6 Å and some

longer range contributions from Ta-O distances at around 4.5 Å. The dominant contributions in the partial RDF are from the Ta-O and Ta-Ta distances with smaller contributions from atom to atom distances involving Ti, as would be expected given the small percentage of Ti doping in the coating.

The 53.8% Ti coating has a much larger contribution from Ti atom interactions as expected. From 1.5 to 2.4 Å Ta-O distances and a larger contribution from the Ti-O distances create the major contributions to the first peak in the full RDF. The addition of the atomic distances from 3 to 4 Å creates most of the contributions from the second major peak in the experimental RDF. It is apparent that this peak widens when compared to the 20.4% Ti coating based on the larger contribution from the Ti-Ta distances at 3.3 Å with other major contributions from Ti-Ti distances at 3.6 Å and Ta-Ta distances at 3.8 Å. The Ti-Ti distances also have a much more noticeable role in the 53.8% Ti coating with a reduction in the contribution from the Ta-Ta distances, as is perhaps expected given the much larger Ti doping concentration.
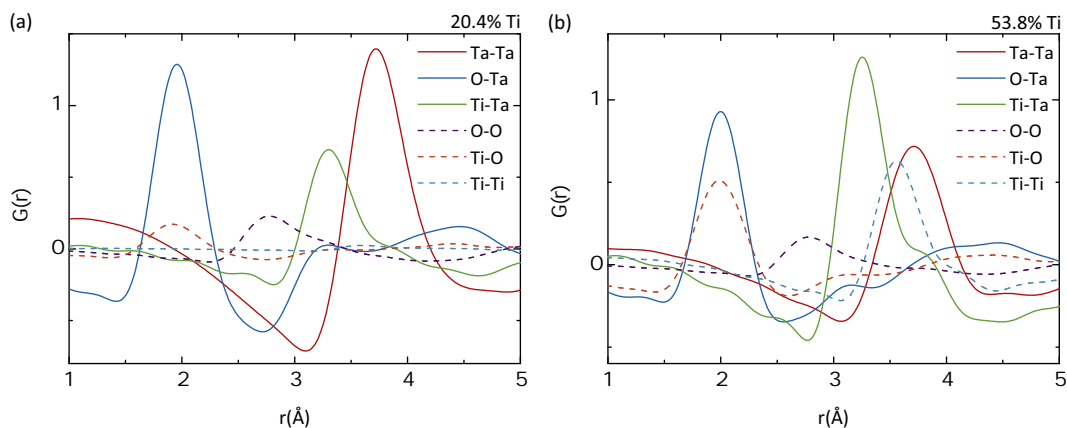
Figure 4.8: *Partial RDFs for the (a) 20.4% and (b) 53.8% Ti doped coatings.*

Bond analysis comparisons were carried out for the 20.4% and 53.8% Ti models. The bonds were defined as before when examining the DFT and refined models, where a bond is defined as an atom to atom distance of less than the sum of their covalent radii (Ta = 1.7 Å, Ti = 1.6 Å, O = 0.73 Å)

plus a bond tolerance factor set at 0.1 Å.

Bond Type	20.4% Ti	53.8% Ti
Ta-Ta	3.45	3.45
Ta-Ti	3.25	3.23
Ta-O	2.00	2.02
Ti-O	1.99	2.03

Table 4.2: *Average bond lengths (Å) for 20.4% and 53.8% Ti coatings*

The average bond distances for the two coatings are shown in Table 4.2, the results show that the average bond distances remain relatively constant between the coatings and that they correspond well to the major peaks distance distributions shown in the PRDFs (Figure 4.8). This also highlights that the Ta-Ti bonds are around 0.2 Å shorter than Ta-Ta bonds.
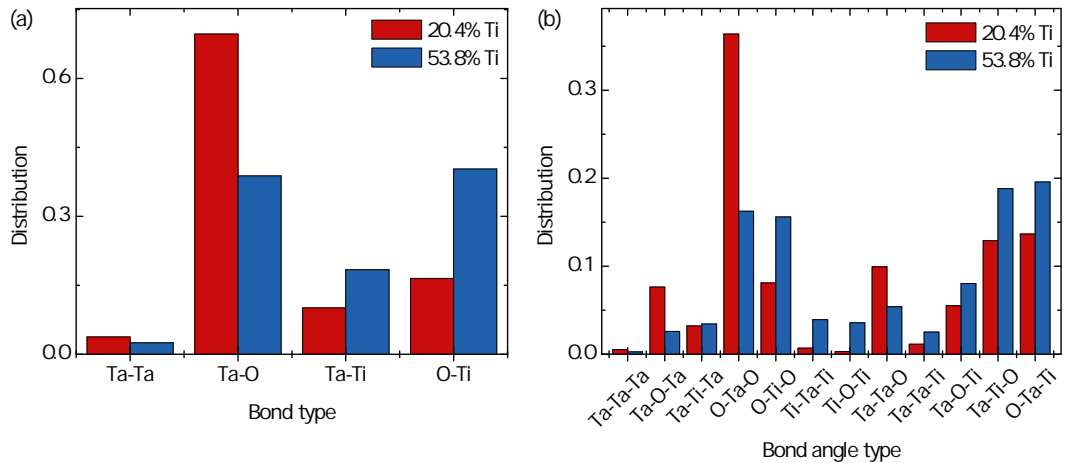
Figure 4.9: *Parameter distributions comparing the 20.4% and 53.8% Ti coatings: a) bond type distribution; b) bond angle type distribution.*

Figure 4.9 (a) shows the comparison for bond type distribution and shows that Ta-Ta content stays relatively constant between the Ti doping levels. The Ta-O bonds show a decrease in proportion as the Ti doping increases, as expected due to the increased proportion TiO_2 in the atomic structure, subsequently causing an increase in the level of Ta-Ti and O-Ti bond distributions.

The bond angle type distributions shown in Figure 4.9 (b) reflect the changes observed in the bond type distributions, with fewer contributions from the bond angles that involve Ta-O bonds and an increase in O-Ti bonds as the Ti doping level increases. This is most noticeable when examining the O-Ta-O and O-Ti-O distributions. In the same way Ta-O-Ta decreases as Ti-O-Ti and Ti-O-Ta increases with the increase in Ti doping.
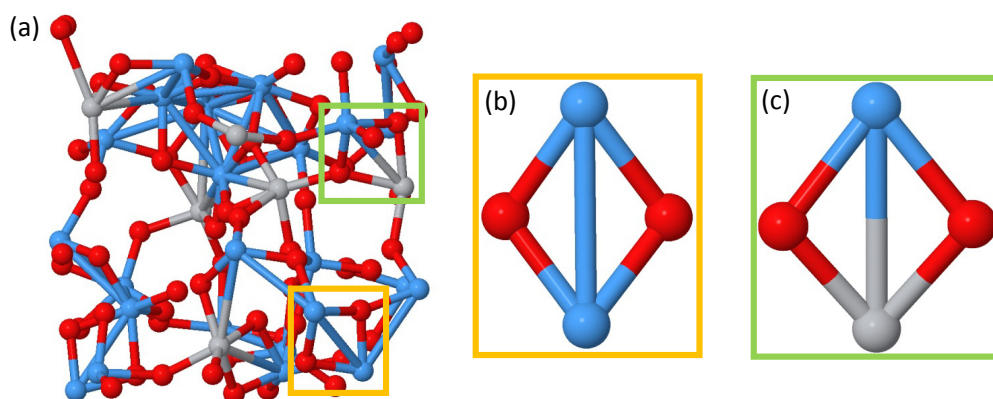
Figure 4.10: *Image of 20.4% Ti doped coating model for the (a) DFT model high-lighting the (b) Ta_2O_5 ring fragments and (c) $TaTiO_2$ ring fragments present in the models.*

In both of the doped Ta_2O_5 models there were contributions from the Ta_2O_2 ring fragments that were previously seen in the heat-treated Ta_2O_5 coatings. Figure 4.10 (a) shows the model that is the result of the DFT model for the 20.4% Ti coating, highlighting the presence of the Ta_2O_2 ring fragment (Figure 4.10 (b)). The refined models show the same features over a longer range and the DFT model is shown only because it is smaller and representative of the large refined models. Interestingly the presence of the Ti atoms produced $TaTiO_2$ ring fragments as shown in Figure 4.10 (c). This gives further evidence that Ti can take the place of a Ta atom in the coating structure, as suggested in the literature for similar crystalline compound structures [142, 143]. The $TaTiO_2$ ring fragments became a more prominent feature in the 53.8% Ti doped coating as expected with the increased Ti content in the coating structure.

A small number of Ti_2O_2 ring fragments were also present in the coatings, although they did not share a Ti-Ti bond.

In order to further examine the changes to the bonds in the coatings and to further investigate the ring fragments, the bond angle distributions have been examined for the various bond angle types and are shown in Figure 4.11.

The bond angle type distributions show clear variations between the coatings as previously discussed and shown in Figure 4.9 (b). However it is interesting to note that the bond angle distributions for each bond angle type do not show any very significant changes. This suggests that for 20.4% and 53.8% Ti doping levels the positions that atoms prefer to sit in are similar in each case, even though the Ti doping substantially increases.

As previously described, the $TaTiO_2$ ring fragments have Ta-Ti bonds that are slightly shorter than the Ta-Ta bonds present in the Ta_2O_2 ring fragments. This is reaffirmed through analysis of the bond angle distributions where the Ti-O-Ta bond angles (Figure 4.11 (c)) have a lower average in bond angle distribution at $110°$, than the Ta-O-Ta bond angles (Figure 4.11 (a)) at around $130°$. In both cases the peaks of these bond angle distributions appears to reduce by around $10°$ as the Ti doping is increased. This is further shown through the distribution of O-Ti-O bond angles (Figure 4.11 (d)) have more spread at higher angles around $100°$ compared to the O-Ta-O bond angles (Figure 4.11 (b)) at around $90°$. The Ta-Ta-O (Figure 4.11 (f)) and the Ta-Ti-O (Figure 4.11 (g)) bond angle distributions both show a defined peak at $30°$ and $40°$ relating to the ring fragments, which in both cases become more defined as the Ti doping increases. The Ti-O-Ti bond angles shown in Figure 4.11 (e) show similar distributions to the Ta-O-Ta and Ta-O-Ti bond angles giving evidence for the Ti_2O_2 ring fragments, even if they have very low occurrence in the models as shown in 4.9 (b). The Ti-Ta-Ti bond angles (Figure 4.11 (h)) show the range of all metal bond angles, with a peak at around $70\text{-}80°$ and there appears to be more of a spread at higher angles as Ti doping increases.
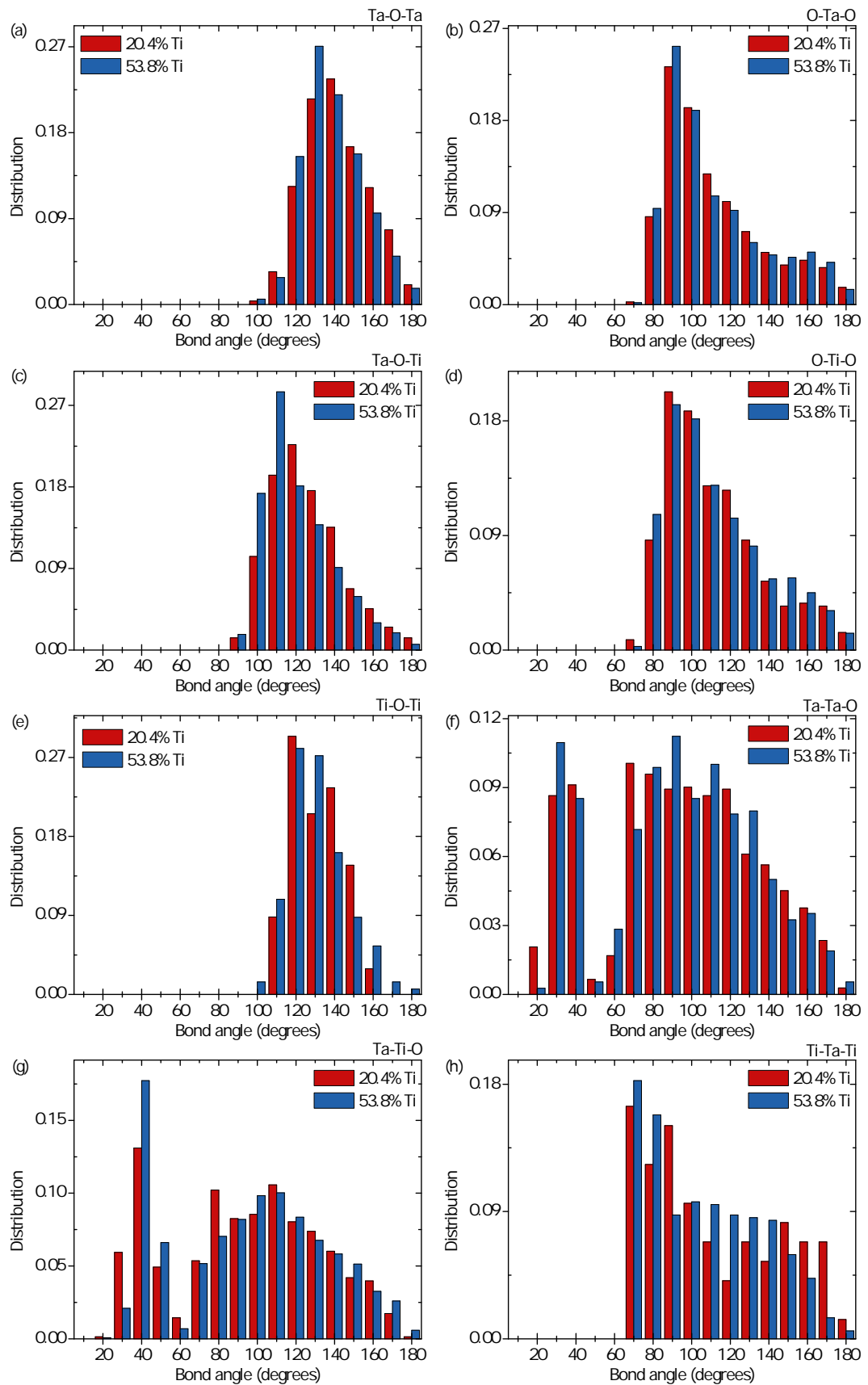
Figure 4.11: *Bond angle distributions for the comparing the 20.4% and 53.8% Ti coatings for the labelled bond angle types.*

Co-ordination numbers for these coatings were also found and are shown in Table 4.3. As with the results for the heat-treated CSIRO Ta_2O_5 coatings in Chapter 2, the co-ordination numbers show considerable spread as may be expected due to the nature of amorphous materials, and it is therefore difficult to make firm conclusions from obtained values. However, the average co-ordination numbers show that when the Ti doping is increased, the tantalum co-ordination number increases while the titanium co-ordination number decreases. The oxygen co-ordination number also increases slightly as Ti doping increases.

Atom	20.4% Ti	$\pm$	53.8% Ti	$\pm$
Tantalum	4.83	1.45	5.72	1.83
Titanium	5.89	1.80	4.80	1.75
Oxygen	1.68	0.64	1.97	0.71

Table 4.3: *Co-ordination numbers for the Ta_2O_5 coatings doped with TiO_2, the '$\pm$' values indicate the spread obtained for a given co-ordination number.*

4.3 Preliminary studies of the relationship of Ti doping to mechanical loss

Preliminary investigations were carried out to identify any correlation between changes in the coating structure with changes in the mechanical loss. In particular correlations between the first (metal-oxygen dominant distances) and second (metal-metal dominant distances) major peak positions in the RDF and their FWHMs were observed. They are shown in Figure 4.12 where the RDF properties are overlayed with the mechanical loss measurements.

Figure 4.12 (a) shows the 1st RDF peak position with the mechanical loss overlayed. It shows that the first peak position is at its maximum of around 2 Å at the same point as the mechanical loss is at its minimum, and is from the
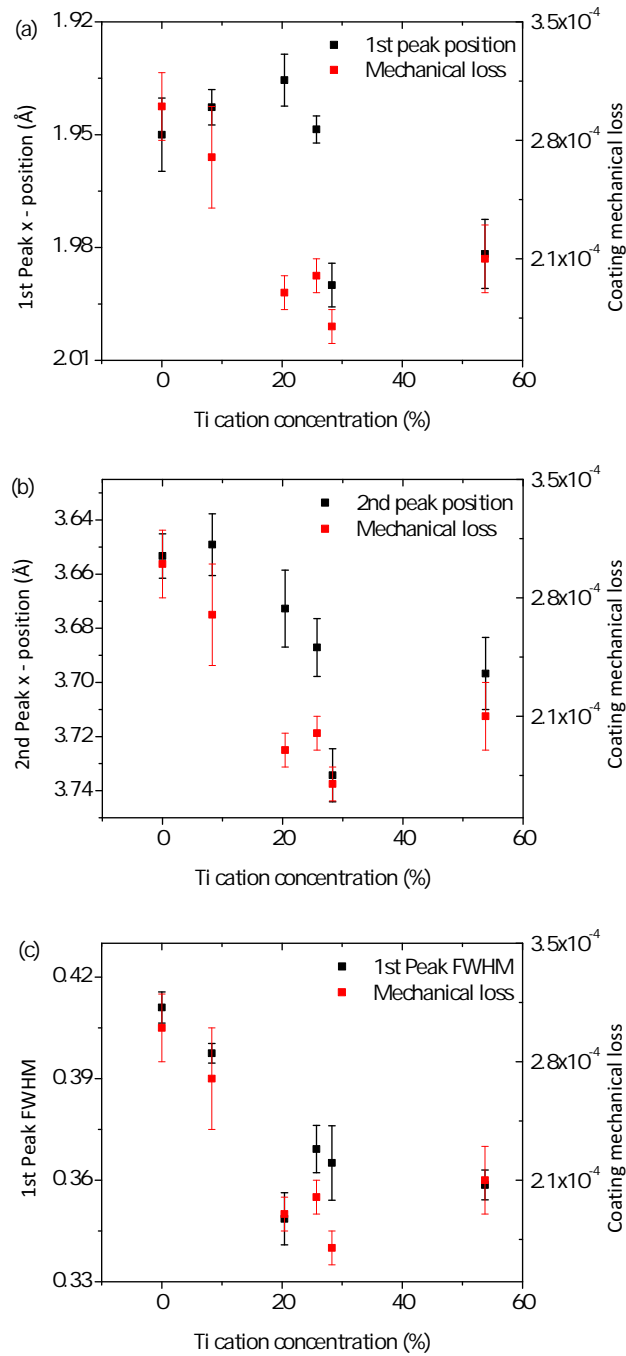
Figure 4.12: *RDF parameter statistics overlayed with the measured multi-layer coating mechanical loss against the Ti doping concentrations, highlighting the interesting trends in the structure with the changes in mechanical loss.*

28.3% Ti coating. There is a similar pattern for the 2nd RDF peak positions shown in Figure 4.12 (c), with the maximum peak position of around 3.74 Å at the minimum mechanical loss given by the 28.3% Ti coating. Interestingly as the Ti doping increases both the first and second peak positions follow a somewhat similar trend, where before and after the 28.3% Ti doping level the peak positions are at a shorter distance and the mechanical loss is higher. Figure 4.12 (b) shows that the 1st peak FWHM also follows a similar trend to the mechanical loss, although the FWHM minimum does not occur for the 28.3% Ti coating. This shows that in general as the peak becomes narrower and more well defined the mechanical loss is also reduced. The remaining measured RDF properties do not show any more obvious correlations with the measurements of mechanical loss.

Oxygen deficiency was also calculated based on the EELS data where it assumed that every Tantalum atom should be accompanied with 2.5 Oxygen atoms and likewise every Titanium atom should be accompanied with 2 Oxygen atoms, due to the ideal combination of Ta_2O_5 and TiO_2. This implies that for a given doped Ta_2O_5 coating the oxygen deficiency, δ_O, from the EELS stoichiometry is:

$$\delta_O = \frac{O_{total} - ((Ti_{total} \times 2) + (Ta_{total} \times 2.5))}{(Ti_{total} \times 2) + (Ta_{total} \times 2.5),} \tag{4.1}$$

where n_{total} is the total fraction of element n calculated from the EEL spectra.

The results are shown in Figure 4.13, where the sample that is closest to the ideal compound and is therefore the least oxygen deficient is the 28.3% Ti coating, which is also the coating with the lowest measured mechanical loss and may be a potential avenue to explore in the future as a potential correlation between stoichiometry and loss. The 25.7% and 53.8% Ti coatings are both around 25% oxygen deficient which is considerably higher than the other coatings. This may be because these coatings were manufactured in a different and larger coating chamber, where there may have unintentionally been less oxygen present in the atmosphere inside the chamber.
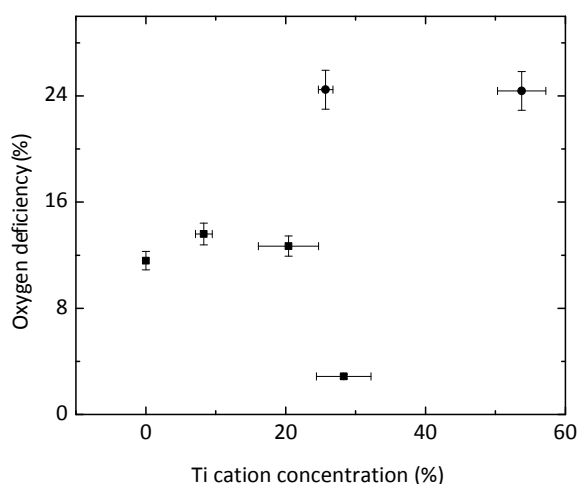
Figure 4.13: *Oxygen deficiency against Ti doping concentration*

4.4 Conclusions

Multi-layer coatings manufactured by LMA that consisted of 30 alternating layers of SiO_2 and Ta_2O_5 doped with TiO_2 show a significant reduction of mechanical loss of up to 40%, when comparing measurements from the 0% Ti coating (only Ta_2O_5) to the 28.3% Ti coating. This observation made it important to investigate changes in the atomic structure that may be causing this reduction.

Changes in the atomic structure were analysed between the doping concentrations through analysis of the RDFs (Figure 4.3). The RDFs showed that an increase in the contribution from the TiO_2 significantly changes the local atomic structure of the coating.

The atomic models of the 20.4% and 53.8% Ti coatings were then modelled. It was shown that the RDFs generated from the refined models had generally good agreement with experimental RDFs. Comparisons were made between their DFT models, produced after molecular dynamics simulations, and their refined models, which are large models produced from the DFT models and then refined back the experimental RDF data, in order to examine the quality of the refined model. The results show that in general the DFT and the final

refined models produce similar bond type and average bond angle distributions meaning that these models are viable and representative of their coating's amorphous atomic structure.

Comparisons between the 20.4% and 53.8% Ti coatings atomic structures were then carried out. The comparisons highlighted the increasing contributions from the Ti-Ta/Ti and Ti-O distances as the Ti doping level increases as shown in the partial RDF (Figure 4.8). Bond distances were also shown to be very similar between the 20.4% and 53.8% Ti coatings, where Ti-O bonds where on average 0.2 Å shorter that Ta-O bonds. The bond type and bond angle type distributions showed an increase in distributions from Ta-Ti and Ti-O as the Ti doping increased and a subsequent reduction in Ta-Ta or Ta-O contributions. There were also no Ti-Ti bonds found in the coating structures. Further analysis of the coating structure revealed that there was still considerable contributions from the Ta_2O_2 ring fragment, as seen in the CSIRO heat-treated Ta_2O_5, but with the addition of $TaTiO_2$ ring fragments that increased in presence with the higher doping percentage. Analysis of the bond angle distributions verified these $TaTiO_2$ ring fragments and also indicated that the Ta-O-Ti bond angles are slightly lower than the Ta-O-Ta bond angles, as expected with the shorter Ta-Ti bonds. The co-ordination numbers were also compared and they indicated that the Ta co-ordination increases, as the Ti co-ordination decreases, with increased Ti doping. Future research will aim to create atomic models for all of the Ti doping concentrations in order to fully understand the changes in the atomic structure between them, paying particular attention to the structure of the 28.3% Ti coating model which has the lowest measured mechanical loss.

A preliminary analysis comparing the changes in the RDF structure to the changes found in mechanical loss as Ti doping increases was also carried out and with some interesting correlations being identified (see discussion around Figure 4.12). This includes changes to first and second major peak positions,

that indicate the most likely nearest neighbour distances between the metal-oxygen and metal-metal distance respectively, where it was shown that the 28.3% Ti coating, with the lowest measured mechanical loss, had the highest first and second peak distances and therefore the longest average metal-oxygen and metal-metal distances. The trend between the first peak FWHM, where a smaller value indicates a sharper peak which in turn relates to a decrease in the distribution of interatomic distances at that point, and the loss is also remarkably similar suggesting that a slight increase in the order of the coating as the Ti doping increases may be a factor in helping to reduce mechanical loss. The lowest mechanical loss, 28.3% Ti, coating was also shown to be the least oxygen deficient coating at around 3%, indicating that is the coating closest to a perfect stoichiometry, where for every Ta or Ti atom there were 2.5 or 2 oxygen atoms, respectively, in the atomic structure. This may also be an preliminary indication that the amount of oxygen in a coating plays an important role in its mechanical loss.

There is still further work to be carried out to fully identify and verify changes in atomic structure compared to mechanical loss. The modelling process will be carried out for the remaining coatings in order to generate a complete data set for all of the available Ti doping concentrations. Further development of the modelling procedure will also be carried out in order to generate a closer match from the DFT models to the final refined models produced. This will be discussed in more detail in Chapter 6.

Chapter 5

Investigations of the material properties of HfO$_2$ and SiO$_2$ coatings

5.1 Introduction

Ta$_2$O$_5$ is not the only coating material under consideration for future generations of gravitational wave detectors. A number of alternatives are being considered with the primary aim of gaining a further understanding of the mechanisms of mechanical loss, in an attempt to reduce its magnitude and effects.

HfO$_2$ coatings are one of the possible alternatives to Ta$_2$O$_5$ coatings that, as will become apparent, may provide similar levels of mechanical loss at room temperature and potentially lower loss at cryogenic temperatures. Further study of the SiO$_2$ layers that form the low refractive index parts of a multi-layer dielectric coating is also of interest, in particular to investigate the possibility that differences in the structure of the SiO$_2$ coating compared to that of bulk or substrate SiO$_2$ may be related to different levels of mechanical loss.

This chapter will include preliminary studies of the material properties of various HfO$_2$ coatings along with a preliminary study of their atomic structures. The investigation of a promising HfO$_2$ coating doped with SiO$_2$ will

be also be presented. Finally, results from atomic structure investigations of heat-treated SiO_2 coatings and substrates will be given.

5.2 Investigations of multi-layer coatings with a HfO_2 component

5.2.1 Investigations of a multi-layer coating of HfO_2 and SiO_2

5.2.1.1 Mechanical loss measurements

Mechanical loss measurements of a multi-layer $300\,^\circ$C HfO_2 coating manufactured by CSIRO [127] were carried out at room temperature, and the coating loss was extracted following the techniques described in Chapter 2. The values of the coating mechanical loss, measured for four resonant modes on the sample are shown in Figure 5.1.
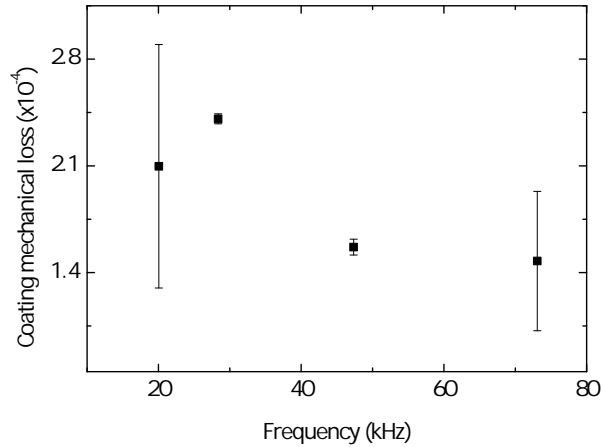
Figure 5.1: *Room temperature mechanical loss of a multi-layer HfO_2/SiO_2 coating, heat-treated at $300^\circ C$.*

As the coating consists of both SiO_2 and HfO_2 layers, the HfO_2 loss component, $\phi_{\mathrm{HfO_2}}$, of the coating mechanical loss was extracted [88]. No clear frequency dependence of the loss was observed thus the values obtained were averaged to get $\phi_{\mathrm{HfO_2}} = (2.2 \pm 0.6) \times 10^{-4}$. The coating parameters used in this calculation are listed in Appendix C.

5.2.1.2 Atomic structure investigations

Preliminary atomic structure investigations of the multi-layer HfO$_2$/SiO$_2$ coating suggest that, although all of the SiO$_2$ layer remain completely amorphous, the HfO$_2$ layers of the coating appear to be part-crystallised, as shown in Figure 5.2.
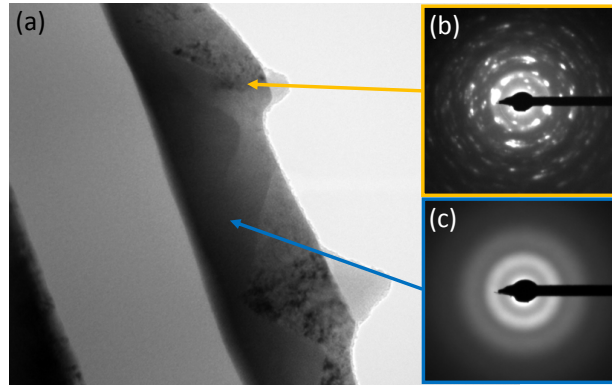
Figure 5.2: *(a) bright-field TEM image taken from the multi-layer heat-treated HfO$_2$/SiO$_2$ heat-treated at 300°C where the light areas are the SiO$_2$ and the dark areas are HfO$_2$. The part-amorphous part-crystalline nature of the HfO$_2$ layers is also highlighted by showing the diffraction patterns taken from an (b) crystalline and (c) amorphous area of a HfO$_2$ layer.*

From the diffraction pattern in Figure 5.2, it appears that the HfO$_2$ layer are part-polycrystalline, and part-amorphous. The crystallised areas appear to be located closer to the top of each layer, closest to the coating surface, and then become amorphous towards the bottom of the layer, closest to the coating substrate.

A more detailed study of the crystallisation in the HfO$_2$ coating material will be presented in Section 5.3 for the single layer HfO$_2$ coatings, where similar part-crystalised coatings are observed.

There was also no diffraction data taken from the sample suitable for computing RDFs, due to difficulty in collecting diffraction data from suitably thin amorphous areas, as required for good quality RDF measurements. This was

due to the thin nature of the HfO$_2$ layers (130 nm) together with the fact that the regions that remained amorphous were located in the inside, thicker areas, of the crystalline surface.

5.2.2 Investigations of a multi-layer coating of HfO$_2$ doped with SiO$_2$ and SiO$_2$

Amorphous SiO$_2$ has been shown to remain amorphous at high heat-treatment temperatures, up to $930\,^{\circ}$C [144]. It has also been shown that HfO$_2$ coatings crystallise at low heat-treatment temperatures even in the minimum coating deposition environment of $100\,^{\circ}$C (see Section 5.2.1). Therefore it is interesting to investigate the possibility of doping HfO$_2$ with SiO$_2$ in an attempt to retard the onset of crystallisation of coating and create a stable amorphous structure. Doping HfO$_2$ with SiO$_2$ is a technique which has proven to be successful in producing stable amorphous thin films that can increase the crystallisation temperature of the resultant doped coating by up to $300\,^{\circ}$C [145].

To investigate this, a HfO$_2$ coating was manufactured by CSIRO [127] that was doped with 30% (by cation) SiO$_2$ and heat-treated to $550\,^{\circ}$C for 24 hours.

5.2.3 Mechanical loss measurements

Room temperature loss measurements were carried out on the coating sample following the procedure outlined in Chapter 2. The values of the coating mechanical loss measured at four resonant frequencies are shown in Figure 5.3.

As before, when measuring the mechanical loss at room temperature of the $300\,^{\circ}$C coating a composite coating is assumed, in this case a composite of layers of SiO$_2$, and HfO$_2$ doped with SiO$_2$. The doped HfO$_2$ component, $\phi_{\text{doped HfO}_2}$, of the coating mechanical loss is extracted [88] and averaged over the four modes to get $\phi_{\text{doped HfO}_2} = (3.3 \pm 0.2) \times 10^{-4}$, which is slightly higher than the room the upper limit of the room temperature loss values of the measured pure HfO$_2$ coated disk and cantilevers. The coating parameters that were required for this calculation are listed in Appendix C.
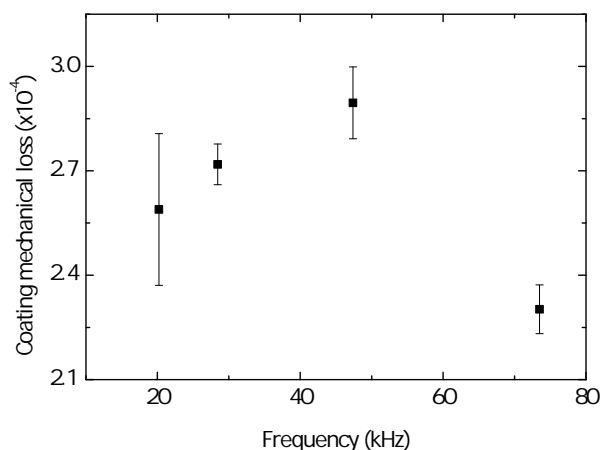
Figure 5.3: *Room temperature mechanical loss measurements for the multi-layer 550°C heat-treated HfO$_2$ coating doped with 30% SiO$_2$.*

There were no coated cantilevers produced for the HfO$_2$ doped with SiO$_2$ coatings and it was therefore not possible to study the mechanical loss at cryogenic temperatures with currently available experimental apparatus. This will be performed in future coating research.

5.2.4 Atomic structure investigations

For the HfO$_2$ doped with SiO$_2$ coating, investigation of this coating in the TEM revealed that even after undergoing heat-treatment at 550 °C the coating remained amorphous with no signs of any crystallisation.

RDF measurements from data collected from only the doped HfO$_2$ layers were carried for this coating and an experimental RDF is shown in Figure 5.4. Analysis of RDF shows the emergence of a peak at roughly 1.5 Å which is caused by Si-O distances from the SiO$_2$ doping in the coating, assumed from comparison with previously measured SiO$_2$ structures [146]. The remainder of the RDF is very similar to the pure HfO$_2$ coatings, indicating the Si-Si distances lie within the contributions involving Hf-O and Hf-Hf distances. This would suggest that the resulting HfO$_2$-SiO$_2$ alloy therefore contains more SiO$_2$-like regions, as well as more HfO$_2$-like regions, mixed at the atomic scale. Further insights into the details of the atomic structures of the HfO$_2$-SiO$_2$ alloys, could
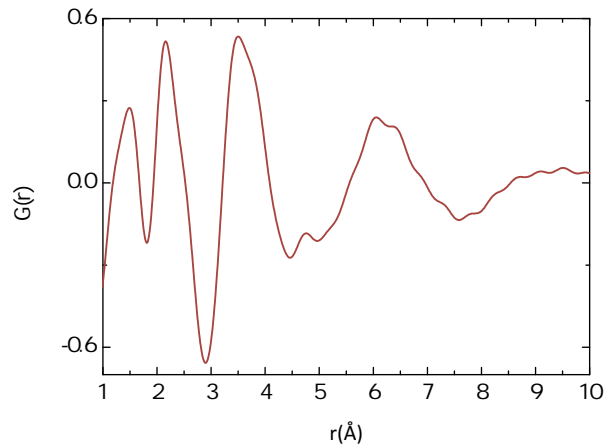
Figure 5.4: *Experimental RDF of the 550°C HfO₂ coating doped with 30% SiO₂.*

only be achieved by the kind of full atomic modelling applied in Chapters 3 and 4, and this may be attempted in future work.

The fact that this coating remains amorphous at relatively high heat-treatment temperature, together with loss results in the same region as pure HfO₂ coatings, makes it an excellent candidate for future study.

5.3 Investigations of single-layer HfO₂ coatings

5.3.1 Mechanical loss measurements

Four coatings of ion-beam sputtered HfO₂ applied to silicon cantilevers were manufactured by CSIRO [127]. These single layer coatings were 500 nm thick, and thicker than the HfO₂ layers multi-layer HfO₂ which were around 130 nm thick. One of the coatings was 'as-deposited' in a 100 °C coating environment, and the other three coatings were subsequently heat-treated post-deposition to 150, 200 and 400 °C respectively for 24 hours.

Figure 5.5 shows the results of mechanical loss measurements carried out at cryogenic temperatures for single layer HfO₂ coatings [147]. These results suggest that as the heat-treatment temperature increases the mechanical loss between 120 K and 250 K decreases. Interestingly there is no clear evidence
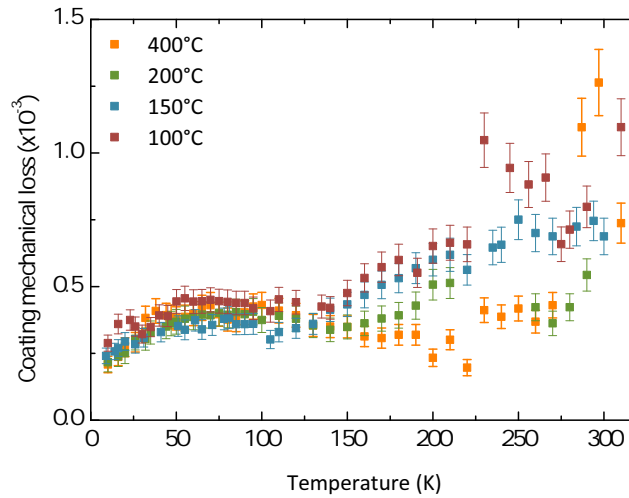
Figure 5.5: *Cryogenic mechanical loss of heat-treated HfO$_2$ coatings, at the frequency of the second bending mode (850 Hz) of the samples [147].*

of any significant low temperature loss peaks, in contrast to the loss behaviour observed for the heat-treated Ta$_2$O$_5$ coatings (see Chapter 3), making HfO$_2$ coatings an interesting candidate for use in the coatings for the mirrors of future detectors that may operate at cryogenic temperatures.

5.3.2 Atomic structure investigations

Investigations of the atomic structure of the single layer HfO$_2$ coatings were then carried out in the TEM and it was found that all of HfO$_2$ coatings had part-crystallised.

Figure 5.6 shows dark field TEM images where some crystallised areas of the coatings appear highlighted due to strong Bragg scattering (see Chapter 2) of suitably orientated crystallites. The coatings appear to have crystallised from the coating surface down into the bulk of the coating, but not fully as they all show amorphous regions before the coating reaches the substrate. From the dark field images there appears to be relatively small changes between the crystallisation from the 'as-deposited' 100 °C to the 400 °C coating, however there does appear to be a slight increase in the depth to which the crystallisation penetrates as the heat-treatment temperature is increased. The
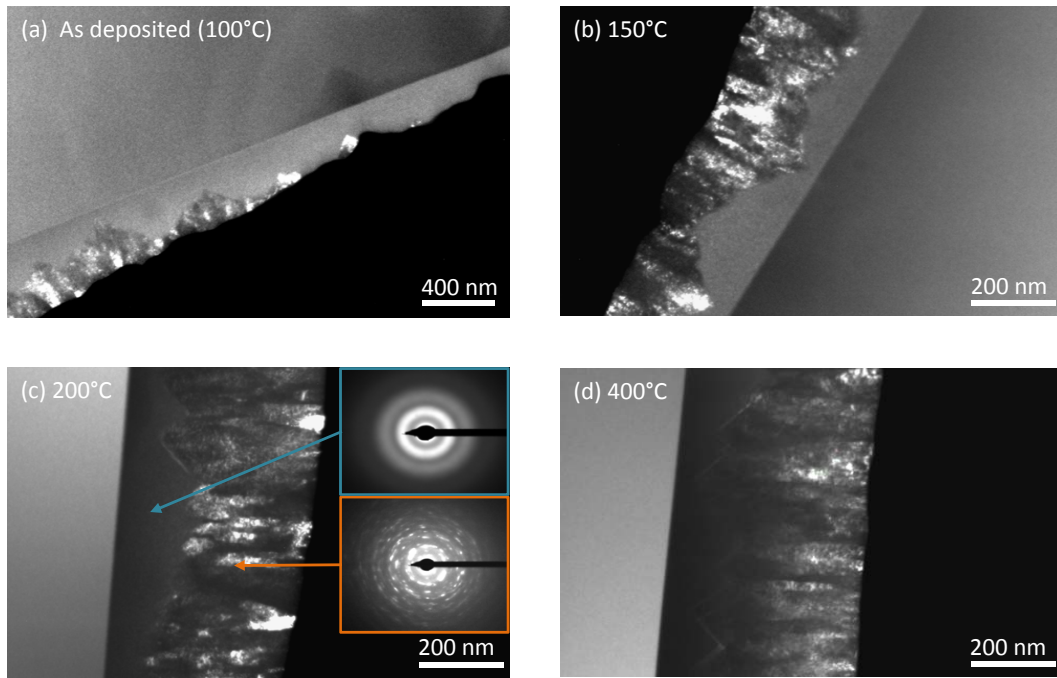
Figure 5.6: *Dark-field TEM images taken from the heat-treated HfO₂ coatings, showing the (a) as deposited (100° C), (b) 150° C, (c) 200° C and (d) 400° C heat-treated coatings. (c) also highlights the part amorphous part crystalline nature of the coatings by showing the diffraction patterns taken from an amorphous and crystalline areas of the coating.*

crystals appear to have grown in a columnar fashion, growing inwards from a nucleation point that is most likely the coating surface. Another feature worth noting is the 'saw-tooth' appearance of the interface between the amorphous and crystalised coating. The crystallised areas appear to become better defined with increasing heat-treatment, as does the interface to the lower amorphous area, and is most noticeable in the 400 °C coating (Figure 5.6 (d)). Figure 5.6 (c) highlights the part amorphous and part crystalline nature of the HfO₂ coatings, where the crystallised area of the coating appears poly-crystalline from a diffraction pattern collected in a region near the surface and then fully amorphous in regions closer to the substrate. This result is similar for each of the heat-treated coatings studied.

It was not possible to achieve a full RDF analysis over the full range of heat-
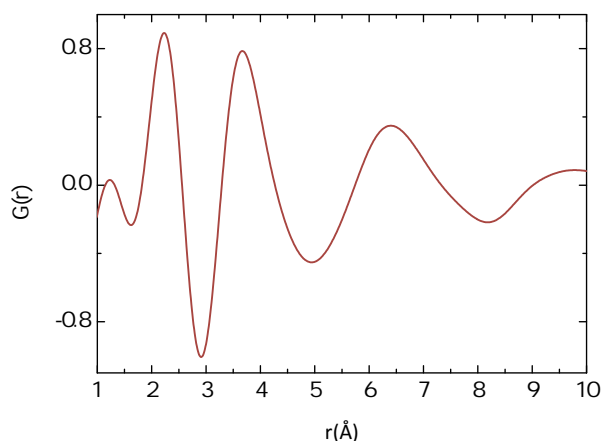
Figure 5.7: *Experimental RDF from the amorphous region of the HfO$_2$ heat-treated to 150°C.*

treatment temperatures due to difficulty in collecting amorphous diffraction data from suitably thin amorphous areas, for the same reasons as the part-crystallised multi-layer HfO$_2$ coating. There was a lack of thin amorphous areas because the amorphous region was always inside the crystalline surface, and this meant that there were not enough scattered electrons from the amorphous regions to create good quality diffraction patterns, which in turn produced poorly fitted RDFs.

However, a small number of good quality diffraction patterns were successfully obtained on which RDF analysis was performed. One of these RDFs is shown in Figure 5.7, where a perfect HfO$_2$ stoichiometry was assumed for the purposes of fitting the RDF scattering potentials. The first peak occurs at around 2.2 Å, and from comparison to previously studied crystalline structures [148, 149] this is likely to correspond tp Hf-O distances, most of which will probably be bonds. Also for comparison to crystalline data, the second major peak at 3.6 Å is likely to correspond to Hf-Hf distances. The subsequent peaks in the RDF are a result of longer range distances between Hf-Hf and Hf-O.

Modelling the atomic structure, as presented in previous chapters, would provide a fuller understanding of the amorphous structure. This presents an

interesting area for future study, where multiple well-fitting RDFs along with their atomic models should provide enough data to make accurate comparisons between the atomic structures between different heat-treatment temperatures of HfO_2.

5.4 Investigations of SiO_2 coatings and substrates

The amorphous SiO_2 used in the substrate and coatings for gravitational wave detectors has been shown to have a lower mechanical loss than the Ta_2O_5 coatings [150]. However, there is little known about the differences in the atomic structure and properties between the bulk SiO_2 used for the substrate, and the ion-beam sputtered SiO_2 coating used as the low refractive index layer in the multi-layer dielectric coatings.

In order to study the differences between the SiO_2 coating and substrates, single layer amorphous SiO_2 coatings deposited on amorphous SiO_2 substrates where manufactured by CSIRO [127] and heat-treated for 24 hours at 300, 600 and 800 °C. Atomic structure investigations were carried out on these coatings and will be described in the following sub-sections.

There are no mechanical loss measurements presented for the SiO_2 coatings as these are currently under investigation.

5.4.1 Atomic structure investigations

RDF measurements were made in order to study possible atomic structure changes between the coating and substrate, and also study possible changes in the atomic structure due to heat-treatment. This was done by collecting electron diffraction data from thin areas of the coating and substrates for each sample, and computing RDFs for each region.

Figure 5.8 shows an experimental RDF measurement from the 600 °C SiO_2 coating. The structure of this RDF is representative of what was seen across
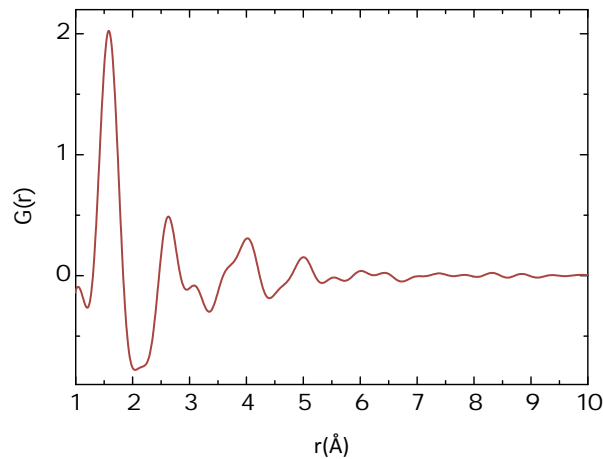
Figure 5.8: *Experimental RDF of the 600°C SiO$_2$ coating*

the entire range of SiO$_2$ coatings and substrates at the various heat-treatment temperatures, as there was no large or obvious changes between their RDFs. It shows the dominant first major peak at around 1.6 Å, which from study of previously measured atomic structures of amorphous SiO$_2$ [146] crystalline SiO$_2$ quartz [151], corresponds to Si-O distances which will predominantly be Si-O bonds. Also from the previously studied structures [146, 151] the second major peak in the RDF that occurs at around 2.6 Å is likely due to longer Si-O distances, but mostly Si-Si distances which will also predominantly consist of bonds. The smaller peaks that are seen at longer range are caused from long range Si-O and Si-Si distances which get smaller with increasing distance in the RDF, as expected due to the amorphous nature of the material giving the absence of any long range order.

In the same way as in previous chapters, the most important features of the first and second major peak peaks in the RDF are tracked across the entire heat-treatment range for both the coatings and substrates and shown in Figure 5.9. In general it appears that there are only subtle changes in the RDFs, and therefore the atomic structures, between the substrate and coating over the entire heat-treatment range. This illustrates that, for the samples studied, there are only subtle differences between the atomic structure of the coated
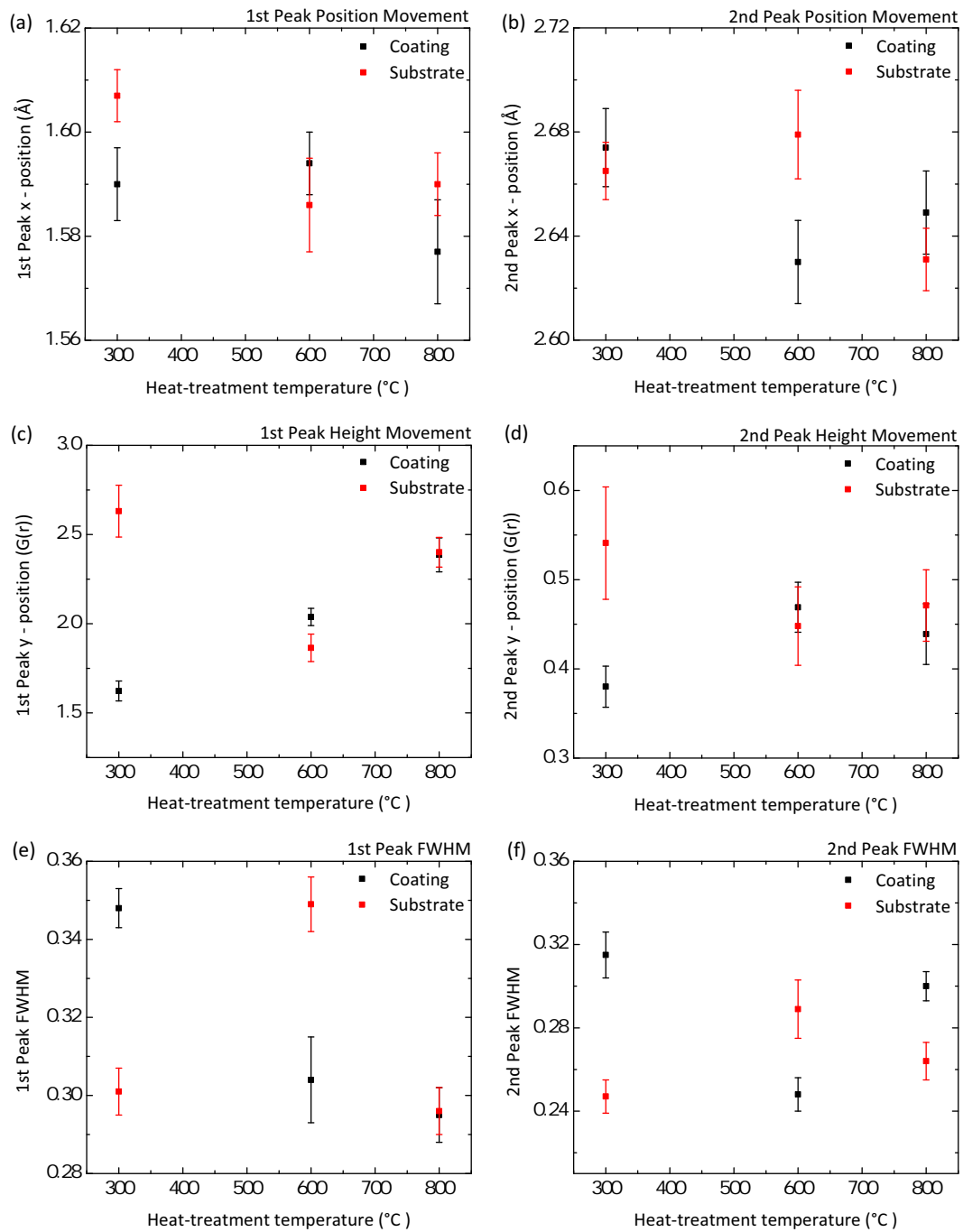
Figure 5.9: *RDF analysis of the SiO$_2$ coatings and their SiO$_2$ substrates, where the changes in the RDFs against heat-treatment temperature are presented. (a) and (b) show the changes to the 1st and 2nd major peak positions, (c) and (d) show changes in the 1st and 2nd peak height respectively, and (e) and (f) shows the changes in the 1st and 2nd peak full width half maxima respectively.*

SiO$_2$ versus the substrate SiO$_2$.

Figure 5.9 (a) and (b) show the position, or distance from the central atom, of the first and second major peaks in the RDF respectively and indicate that there are no major changes within error, suggesting that the Si-O and Si-Si interatomic distances are relatively constant and stable. Figure 5.9 (c) shows the height of the first peak steadily increasing with heat-treatment temperature for the coatings indicating that the Si-O distances are becoming more ordered, similar to trends seen with Ta-O distances for the Ta$_2$O$_5$ coatings (discussed in Chapter 3). This is further evident when considering the first peak full width at half maximum (FWHM), shown in Figure 5.9 (e), for the coating as it also decreases with increasing heat-treatment temperature, indicating a decrease in atomic distance distribution and therefore increase in order. The first peak height and FWHM for the substrate does not show a consistent pattern with increasing heat-treatment. Changes with the height of the second peak are within error and stay relatively constant for both the substrate and coating as shown in Figure 5.9 (d). It is also difficult to find any trends in the second-peak FWHM, shown in Figure 5.9 (f).

Comparing the RDF data over the heat-treatment range for the substrates may not be entirely relevant as it has not been possible to verify that these coatings were all deposited on identical SiO$_2$ substrates, i.e., manufactured at the same time and with similar specifications. However if we assume they are all identical substrates, when examining all of the tracked changes in the RDFs it appears that the biggest difference between the substrate and coatings is with the sample heat-treated to the lowest temperature at 300 °C, and the most similar coating and substrate appears to be the sample heat-treated to the highest temperature at 800 °C. This may indicate that a rising heat-treatment temperature has the effect of making the atomic structure of the coating and substrate more alike.

5.5   Conclusions

It has been identified that pure HfO_2 coatings produce loss results which are comparable to previously measured mechanical loss results for Ta_2O_5. Preliminary cryogenic loss results also show the absence of the low-temperature loss peaks observed in the Ta_2O_5 coatings [126]. However, all of the heat-treated coatings including the 'as-deposited' in a $100\,°C$ environment are part-crystallised. Further investigation, including atomic modelling, could be the subject of a possible future study of the amorphous regions of the pure HfO_2 coatings. This should allow a better understanding of their atomic structures, in order to understand their intrinsic structures, which will be of assistance in understanding the atomic structure of more crystallisation-resistant alloys of HfO_2 with other oxides such as SiO_2.

It appears that doping HfO_2 with SiO_2 can avoid the onset of crystallisation and produce a stable amorphous structure after heat-treating at $550\,°C$ with a mechanical loss that is only slightly higher at room temperature to the measured values of a pure multi-layer HfO_2 coating heat-treated to $300\,°C$. This makes it an interesting candidate for future study. Future coating runs that could enable studies of the cryogenic mechanical loss of doped HfO_2 could be very interesting, as it appears that the low temperature loss peak is absent with HfO_2 (Figure 5.5) seen in the Ta_2O_5 coatings (see Chapter 3). Further investigation into the atomic structure of the doped HfO_2 would also be very interesting in the future, including modelling the atomic structure to fully analyse the Hf-Si-O bonding structure in the coating, and the degree to which HfO_2-like and SiO_2-like bonding is intermixed in these mixed compositions.

SiO_2 coatings deposited on SiO_2 substrates show no major changes between the atomic structure of the coating and substrate. However, the preliminary results reveal some evidence that the coating and substrate structures become more alike with increasing heat-treatment. Atomic structure changes in the coating indicate an increase in ordering in the coating structure as the

heat-treatment temperature is increased (see discussion around Figure 5.9), similar to the observed changes in the heat-treated Ta_2O_5 coatings.

Chapter 6

General conclusions and future work

6.1 Introduction

It is greatly expected that the planned upgrades to the current long-baseline interferometric gravitational wave detectors will make the the first direct detection of gravitational waves, which will give rise to an entirely new window on the Universe. These second generation detectors will aim to improve sensitivity by a factor of around ten, allowing a much greater chance of detecting gravitational waves, particularly from sources such as coalescing compact binary systems. However, the sensitivity of these detectors will still be limited by noise sources, such as photon-shot, seismic and thermal noise, which could be further reduced by the creation of new technologies. Therefore there is currently an international network of scientists working on the design of the third generation of interferometric gravitational wave detectors which have the aim of further reducing the effect of these noise sources, and thus further increasing detector sensitivity.

As discussed in Chapter 2, thermal noise arising from the mirror coatings in the detector test-masses is a particularly important noise source, limiting the sensitivity of detectors between the frequency range from a few tens Hertz

to several hundred Hertz. The research that has been presented in this thesis focused on investigating the mechanical loss, which is directly related to the thermal noise, of these coatings. In particular this thesis presents the first attempts at correlating changes in atomic structure of the coatings to the mechanical loss where various properties, such as heat-treatment and doping, of the coatings have been systematically changed.

6.2 General conclusions

Studies of the effect of heat-treatment on Ta_2O_5 coatings

Heat-treatment of Ta_2O_5 coatings has been shown to cause changes in the mechanical loss observed at low temperature, with loss peaks arising in the region of 10s K which increase in magnitude and become more defined as the heat-treatment temperature rises. It appears that heat-treatment produces subtle changes to the averaged local atomic structures of the coatings. It was shown that as heat-treatment temperature increased the coatings became more ordered, moving towards crystallisation between heat-treatment at 300 - 600 °C coatings and crystallising at 800 °C. Atomic models based on experimental diffraction data of these coatings show stable structures, that show Ta_2O_2 ring fragments which were found to be features present in the crystalline phase of the material. In general as heat-treatment temperature was increased there was an increase in the presence of the Ta_2O_2 ring fragments and a decrease in the presence of Ta-Ta bonds in the atomic structures. It was also shown that changes in the manufacturing deposition methods for the studied Ta_2O_5 coatings created significant changes in the mechanical loss at low temperatures, where it was observed that a 'low water content' manufacturing processes changed the positions and shapes of the low temperature loss peaks. An initial investigation into the local atomic structure at different areas in the coating showed that increasing heat-treatment temperature causes

more ordered coating material closer to the substrate and less ordered (more amorphous) areas of coating closer to the surface of the coating.

Investigations into Ta_2O_5 coatings doped with TiO_2

Multi-layer SiO_2 and Ta_2O_5 doped with TiO_2 coatings show that changing the TiO_2 doping concentration can reduce the mechanical loss of the coating by up to 40%, and it was subsequently found that changing the TiO_2 doping concentration significantly changes the local atomic structure of the coating. Analysis of atomic models created for 20.4% and 53.8% Ti coatings indicated that the bond distances were very similar between the 20.4% and 53.8% Ti coatings, where Ti-O bonds were on average 0.2 Å shorter than Ta-O bonds. The distributions of bonds in the atomic structures of the coatings showed an increase in the occurrence of Ta-Ti and Ti-O as TiO_2 doping was increased. Analysis of the coating structure revealed considerable contributions from Ta_2O_2 ring fragments, as observed in the pure Ta_2O_5 coating, and there was also $TaTiO_2$ ring fragments observed that showed an increase in presence with the higher doping percentage.

Correlations between the atomic structure and mechanical loss of Ta_2O_5 doped with TiO_2 coatings were also identified. The comparisons revealed that an increase in the order of the coating as the Ti doping increases, followed the trend of the mechanical loss values, and it was observed that the multi-layer coating had the lowest measured mechanical loss was at the doped Ta_2O_5 was at its most ordered state. This may suggest that a slight increase in ordering in the atomic structures of the coating may be a factor in helping to reduce mechanical loss. The least oxygen deficient coating was also the coating with the lowest measured mechanical loss, indicating that the amount of oxygen in a coating plays an important role in its mechanical loss.

Investigations of the material properties of HfO$_2$ and SiO$_2$ coatings

Pure HfO$_2$ coatings as a possible alternative to Ta$_2$O$_5$ based coatings produce mechanical losses which are comparable to previously measured loss results for Ta$_2$O$_5$ without the low temperature loss peak observed in the Ta$_2$O$_5$ coatings. However, all of the heat-treated coatings including the 'as deposited' in a 100 °C environment are part crystallised. It was shown that a HfO$_2$ coating doped with 30% (cation) SiO$_2$ remains amorphous, even after heat-treatment at 600 °C and the mechanical loss measured at room temperature was comparable to pure HfO$_2$ coatings. This is a promising coating for future study, where various SiO$_2$ doping levels can be studied, in an attempt to find a high quality alternative to Ta$_2$O$_5$ based coatings. Preliminary atomic structure analysis of SiO$_2$ coatings deposited on SiO$_2$ substrates show the absence of any major changes between the atomic structure of the coating and substrate, although there may be evidence that the coating and substrate structures become more alike with increasing heat-treatment. Analysis of the changes in the atomic structure of these coatings indicate an increase in order of the structure as heat-treatment is increased, similar to the observed changes in the heat-treated Ta$_2$O$_5$ coatings.

6.3   Future work

Improving the data collection from the TEM

Further development of the atomic structure investigation methods is important to increase its accuracy, as well as to gain the ability to measure new properties from the atomic structures of the coating materials. This will allow a greater understanding of the atomic structure of the coatings and give more ways of investigating possible links of material properties of the coatings to their mechanical losses.

There may be ways to improve the way diffraction data from the amorphous materials is collected in the TEM. This will in turn improve the RDF data

quality, which will allow for a better fitting RDF with a reduction in the noise peak. This may be partly accomplished by finding a way of increasing the maximum obtainable q value or scattering angle, limited by the size of the diffraction pattern. Finding a way to extend the range of the diffraction patterns collected will, in turn, increase the range of scattering angles detected. This will result in a higher resolution RDF, which is limited by the maximum q value. This may be achieved by taking one CCD image of a centred diffraction pattern, then moving the centre of the diffraction pattern to the edge of the CCD and recording another with that will include the high q data required.

One other problem is with the diffraction patterns where a slight blooming around the pointer, which is used to block the central electron beam, occurs in the image taken from the CCD. This happens because, at the ideal preset CCD camera length in the TEM, the central beam overflows very slightly around the edges of the pointer. However choosing a preset camera length that completely blocks the central beam, also blocks valuable diffraction data from the coating that lies closest to the central beam. One possible way around this would be to program a new camera length, if this were possible, in between the unsuitable preset camera lengths, that will allow the central beam to be completely blocked by the RDF, without losing the diffraction data closest to the central beam. This would reduce the blooming as much as possible and therefore avoid any interference with the data from the diffracted electrons in the diffraction pattern. This will therefore result in a reduction of excess noise in the diffraction patterns and therefore create a better fitting RDF.

Developing new atomic modelling techniques

The modelling process requires very high levels of computing power and there are a number of improvements that aim to reduce the time spent to create a complete atomic model. At the time of creating the first atomic model for the 400 °C Ta_2O_5 coating (see Chapter 2), the modelling process took roughly

four months to complete. This was because relatively low-powered desktop computers were used for the RMC process. There was also limited access to high performance computer networks running CASTEP [119] for the molecular dynamics stage.

This is aiming to be improved in the future and rewriting the RMC software to allow for parallelisation on a suitable multi-core PC is in progress. The initial results from this new code are promising and show that parallelisation on an 8-core machine would result in a massive increase in the speed of RMC simulations, of the order of around five times. There are also plans to use powerful super-computers, such as HECToR [152], for the molecular dynamics stage, and initial testing has already commenced. These new developments will lead to complete atomic modelling times that are greatly reduced, to around the order of a week, greatly improving simulation throughput, when this is currently the bottleneck in our structure determination process.

There are measurable differences between the model that is the result of the DFT stage and the final refined model, as described in Chapters 3 and 4. It would be beneficial to have as close a match to experimental data as possible after the molecular dynamics simulations stage. One way of achieving this is through optimising features of the DFT simulation process, such as the pseudopotentials sets used for the atoms, the approximations used, the cutoff energy for the simulation, and the number of k-points used. Each of these properties can be tested and varied to find the optimal configuration, and is an important focus for future research to enhance the accuracy of the atomic models.

Analysis of the models can be extended to investigate other material properties of the coatings. Preliminary investigations are underway to extract the Young's modulus and possibly the phonon excitation spectra from the atomic models, which will provide further data to compare to mechanical loss measurements.

Other possible experimental techniques

X-ray diffraction Pair Distribution Functions (PDFs) is another well developed technique which generates results equivalent to that of the TEM RDFs, giving information on the short-range atomic structures of amorphous material. X-rays scatter at larger angles than electrons when they interact with matter [113], which results in the information of the atomic structure stored in the X-ray diffraction data being better defined, compared to the electron diffraction data with relatively small scattering angles. This would therefore mean that the resolution of the RDFs is increased, provided the diffraction data is taken over a large q range. The disadvantage of this approach is that scattering data is gathered over a much larger area of the coating surface 1 cm^2, which means that you would obtain an averaged local atomic structure compared to the nano-scale areas studied in the TEM. There is also the issue of finding appropriate diffraction geometries, with very low angles of incidence are required to ensure that only the thin coating area contributes to the diffraction pattern, avoiding any influence of the substrate. However, this would provide an interesting data set that would complement the electron diffraction RDFs, to be used as further constraints in the modelling process.

A further complementary method to the electron diffraction RDFs that could be used in the future is using X-rays to perform X-ray Absorption Fine Structure (XAFS) measurements where the X-ray absorption edge of an element is studied. This method involves studying the photoelectron that is emitted as a result of scanning the sample through the X-ray energies associated with the absorption edge of the element under investigation. The photoelectron wave backscatters off the surrounding local structures and modulates the absorption coefficient of the X-rays, giving information of the local structure surrounding that particular atom [113].

Alternative coatings and wider applications

HfO_2 has been studied as a possible alternative to Ta_2O_5 coatings, but there are several other coating also under preliminary investigations such as; amorphous-Si, Al_2O_3, Nb_2O_3 and ZrO_2. These coatings will provide a wealth of opportunity to further investigate the mechanical loss and atomic structures of these coatings, with the aim of identifying possible links between them.

The coating materials studied are not only relevant for future generations of gravitational wave detectors. Continuing to develop ways of understanding the local atomic structure of amorphous materials also has a wider research and commercial interest, including coatings for use in ring laser gyroscopes used in inertial guidance systems [153] and frequency stabilisation using ring lasers, relevant to frequency comb techniques which require high quality dielectric coating materials [154, 155]. There are also semiconductor devices which require an insulting thin film layer [156], and more recently amorphous thin films have been used as corrosion resistant coatings for biomedical implants [157].

6.4 Final remarks

The methods of studying the coatings presented in this thesis have demonstrated novel ways of probing the atomic structure of the coating materials. They have proven to be very useful as an initial insight into possible changes in the atomic structures of the coatings that can be related to the mechanical loss.

Finally, the effort to increase the understanding of the mechanical loss in the coating materials is crucial for developing new technologies which reduce its effect. The result will be an increase in sensitivity for future generations of gravitational wave detectors that will allow them to observe gravitational waves from more distant sources, which will undoubtedly add greatly to our understanding of the Universe.

Appendix A

Kirkland fitting parameters

Chapter 2, Section 2.4.7.2, refers to the Kirkland scattering factor, f_{Kirkland} [102],

$$f_{\text{Kirkland}} = \sum_{i=1}^{3} \frac{a_i}{q^2 + b_i} + \sum_{i=1}^{3} c_i \exp(-d_i q^2) \tag{A.1}$$

where a_i, b_i, c_i and d_i are the Kirkland fitting parameters. This results in the requirement for 12 fitting parameters $(a_1, a_2, a_3, \ b_1, b_2, b_3, \ c_1, c_2, c_3, \ d_1, d_2, d_3)$ which are given, for the elements in the coatings studied in this thesis (hafnium, silicon, tantalum, titanium and oxygen), in Table A.1. The units for a_i, b_i, c_i and d_i are Å^{-1}, Å^{-2}, Å and Å^2, respectively [102].

Element	Kirkland fitting parameters		
Hafnium	$a_1 = 3.15920241$	$a_2 = 0.613291586$	$a_3 = 3.03905654$
	$b_1 = 14.0083544$	$b_2 = 0.0884711068$	$b_3 = 0.709697422$
	$c_1 = 0.341530456$	$c_2 = 0.0246166752$	$c_3 = 1.43801570$
	$d_1 = 0.313687522$	$d_2 = 0.0369228699$	$d_3 = 15.0685398$
Silicon	$a_1 = 0.120120147$	$a_2 = 1.06498026$	$a_3 = 0.182256296$
	$b_1 = 70.06310153$	$b_2 = 1.04600373$	$b_3 = 0.0868866872$
	$c_1 = 0.0306076088$	$c_2 = 1.10867696$	$c_3 = 1.58258089$
	$d_1 = 0.214762808$	$d_2 = 3.69205948$	$d_3 = 9.93119843$
Tantalum	$a_1 = 0.747198223$	$a_2 = 3.22045387$	$a_3 = 2.93947802$
	$b_1 = 0.102352889$	$b_2 = 13.8766179$	$b_3 = 0.739861702$
	$c_1 = 0.0229176351$	$c_2 = 0.335663858$	$c_3 = 1.14728503$
	$d_1 = 0.035495002$	$d_2 = 0.205499378$	$d_3 = 0.135849981$
Titanium	$a_1 = 0.737291729$	$a_2 = 0.996300042$	$a_3 = 0.355417565$
	$b_1 = 8.32612403$	$b_2 = 0.496982599$	$b_3 = 0.0728595855$
	$c_1 = 0.0163350335$	$c_2 = 0.360199179$	$c_3 = 1.42171303$
	$d_1 = 0.0731735660$	$d_2 = 0.957232308$	$d_3 = 15.8512114$
Oxygen	$a_1 = 0.368590229$	$a_2 = 0.13289645$	$a_3 = 2.77101233$
	$b_1 = 0.367542561$	$b_2 = 19.395483$	$b_3 = 0.367539567$
	$c_1 = 0.083909305$	$c_2 = 0.181631127$	$c_3 = 0.00105289871$
	$d_1 = 0.758355003$	$d_2 = 2.04360334$	$d_3 = 0.031200946$

Table A.1: *Kirkland fitting parameters for hafnium, silicon, tantalum, titanium and oxygen [102].*

Appendix B

Density measurement for the $400\,^{\circ}\mathrm{C}$ heat-treated $\mathrm{Ta_2O_5}$ coating

The density of the $400\,^{\circ}\mathrm{C}$ heat-treated $\mathrm{Ta_2O_5}$ coating was measured. This was accomplished by firstly measuring the mass of a coated silicon cantilever (with the clamping block section of the cantilever removed), m_{coated}, using a Metler Toledo Ultra Microbalance [158] and then etching the cantilever in 40% unbuffered hydrofluoric acid for 1 hour to completely remove the coating and weighing again to get m_{uncoated}. The mass of the etched material, m_{etched}, was therefore,

$$m_{\mathrm{etched}} = m_{\mathrm{coated}} - m_{\mathrm{uncoated}}.$$

It should be noted that m_{etched} does not equal the mass of the $\mathrm{Ta_2O_5}$ coating, $m_{\mathrm{Ta_2O_5}}$, as there was also an $\mathrm{SiO_2}$ oxide layer of mass, $m_{\mathrm{SiO_2}}$, on the silicon cantilevers which must be taken into account. Therefore,

$$m_{\mathrm{etched}} = m_{\mathrm{SiO_2}} + m_{\mathrm{Ta_2O_5}}. \tag{B.1}$$

The density of the $\mathrm{Ta_2O_5}$ coating, $\rho_{\mathrm{Ta_2O_5}}$, was then calculated by,

$$\rho_{\mathrm{Ta_2O_5}} = \frac{m_{\mathrm{etched}} - V_{\mathrm{SiO_2}}\rho_{\mathrm{SiO_2}}}{V_{\mathrm{Ta_2O_5}}}, \tag{B.2}$$

where V_{SiO_2} and $V_{Ta_2O_5}$ are the volumes of the SiO_2 oxide layer and Ta_2O_5 coating, respectively. The volumes were calculated from measurements of the length and breadth breadth of the cantilever, $l_{cantilever}$ and $b_{cantilever}$, respectively, and thicknesses of the SiO_2 layer and Ta_2O_5 coating, t_{SiO_2} and $t_{Ta_2O_5}$, respectively, from ellipsometry measurements taken using a Sentech SE850 Spectroscopic Ellipsometer [159]. All of the measured values are shown in Table B.1.

The measured density of the Ta_2O_5 coating was $\rho_{Ta_2O_5} = (7.68\pm0.46)\text{g/cm}^3$.

Property	Value
m_{coated}	0.0382 ± 0.00001 g
$m_{uncoated}$	0.0369 ± 0.00001 g
m_{etched}	0.00130 ± 0.00001 g
$t_{Ta_2O_5}$	1.57 ± 0.5 nm
t_{SiO_2}	80 ± 0.5 nm
$l_{cantilever}$	1 ± 0.5 cm
$b_{cantilever}$	3.25 ± 0.5 cm
$V_{Ta_2O_5}$	$(1.07 \pm 0.07) \times 10^{-4}$ cm^3
V_{SiO_2}	$(4.06 \pm 0.07) \times 10^{-5}$ cm^3
ρ_{SiO_2}	(2.202 ± 0.2) g/cm^3 [137]

Table B.1: *Measured properties required for the Ta_2O_5 density measurement.*

Appendix C

Properties of the HfO$_2$ and HfO$_2$ doped with SiO$_2$ coatings

The material properties required for the calculation of the coating mechanical loss in Chapter 5 of the multi-layer coatings are given in the Tables C.1, C.2 and C.3, where Y is the Young's modulus, σ is the Poisson's ratio, n is the refractive index, ρ is the density, α is the thermal expansion coefficient Cv is the specific heat capacity and κ is the thermal conductivity. The material properties for the HfO$_2$ coating doped with SiO$_2$, given in Table C.3, have been averaged by the percentage SiO$_2$ and HfO$_2$ in the coating, which is 30% and 70%, respectively, and follows methods that have been previously detailed in the literature [88, 160].

Property	Value
$Y_{\mathrm{SiO_2}}$	72 GPa
$\sigma_{\mathrm{SiO_2}}$	0.17
$n_{\mathrm{SiO_2}}$	1.45
$\rho_{\mathrm{SiO_2}}$	2.02 g/cm^3
$\alpha_{\mathrm{SiO_2}}$	5.1×10^{-7} K^{-1}
$\mathrm{Cv_{SiO_2}}$	746 Jkg^{-1}K^{-1}
$\kappa_{\mathrm{SiO_2}}$	1.38 Wm^{-1}K^{-1}

Table C.1: *Properties of SiO$_2$ required for the multi-layer HfO$_2$ and doped HfO$_2$ coatings for the room temperature loss measurements [85].*

Property	Value
$Y_{\mathrm{HfO_2}}$	288 GPa [161]
$\sigma_{\mathrm{HfO_2}}$	0.298 [162]
$n_{\mathrm{HfO_2}}$	2.03 [1]
$\rho_{\mathrm{HfO_2}}$	9.68 g/cm^3 [163]
$\alpha_{\mathrm{HfO_2}}$	6.5×10^{-6} K^{-1} [137]
$\mathrm{Cv_{HfO_2}}$	293 Jkg^{-1}K^{-1} [137]
$\kappa_{\mathrm{HfO_2}}$	1.67 Wm^{-1}K^{-1} [137]

Table C.2: *Properties of HfO$_2$ required for the multi-layer HfO$_2$ and doped HfO$_2$ coatings for the room temperature loss measurements.*

---

[1]Data provided by the coating manufacturer [127].

Property	Value
$Y_{\text{doped HfO}_2}$	223 GPa
$\sigma_{\text{doped HfO}_2}$	0.253
$n_{\text{doped HfO}_2}$	1.87
$\rho_{\text{doped HfO}_2}$	7434 g/cm^3
$\alpha_{\text{doped HfO}_2}$	4.7×10^{-6} K^{-1}
$\text{Cv}_{\text{doped HfO}_2}$	428.9 Jkg^{-1}K^{-1}
$\kappa_{\text{doped HfO}_2}$	2.784 Wm^{-1}K^{-1}

Table C.3: *Properties of the effective HfO_2 doped with SiO_2 for the multi-layer HfO_2 doped with SiO_2/ SiO_2 coating for the room temperature loss measurements.*

Bibliography

[1] A. Einstein. *Die Grundlage der allgemeinen Relativitatstheorie. Annalen der Physik*, **49**:769, 1916.

[2] R. A. Hulse and J. H. Taylor. *Discovery of a pulsar in a binary system. The Astrophysical Journal*, **195**:L51–L53, 1975.

[3] J. H. Taylor, R. A. Hulse, L. A. Fowler, G. E. Gullahron, and J. M. Rankin. *Further observations of the binary pulsar PSR 1913 + 16. The Astrophysical Journal*, **206**:L53–L58, 1976.

[4] J. H. Taylor, L. A. Fowler, and P. M. McCulloch. *Measurements of general relativistic effects in the binary pulsar PSR 1913 + 16. Nature*, **277**:437–440, 1979.

[5] J. H. Taylor and J. M. Weisberg. *A new test of general relativity - Gravitational radiation and the binary pulsar PSR 1913+16. The Astrophysical Journal*, **253**:908–920, 1982.

[6] B. P. Abbott, R. Abbott, R. Adhikari, P. Ajith, B. Allen, G. Allen, et al. LIGO: The Laser Interferometer Gravitational-wave Observatory. *Reports on Progress in Physics*, **72**(7):076901, 2009.

[7] H. Grote and the LIGO Scientific Collaboration. *The GEO600 status. Classical and Quantum Gravity*, **27**(8):084003, 2010.

[8] T. Accadia, F. Acernese, F. Antonucci, S. Aoudia, K. G. Arun, et al. *Status and perspectives of the Virgo gravitational wave detector. Journal of Physics: Conference Series*, **203**(1):012074, 2010.

[9] K. Arai, R. Takahashi, D. Tatsumi, K. Izumi, et al. *Status of Japanese gravitational wave detectors. Classical and Quantum Gravity*, **26**(20):204020, 2009.

[10] M. Hewitson, G. Heinzel, J. R. Smith, K. A. Strain, and H. Ward. *Principles of calibrating the dual-recycled GEO600. Review of Scientific Instruments*, **75**(11):4702–4709, 2004.

[11] R. Adhikari. *Second Generation Gravitational Wave Detectors*. In *Laser Science*, page LMA3, 2007.

[12] V. B. Braginsky, M. L. Gorodetsky, and S. P. Vyatchanin. *Thermodynamical fluctuations and photo-thermal shot noise in gravitational wave antennae. Physics Letters A*, **264**:1–10, 1999.

[13] S. A. Hughes and K. S. Thorne. *Seismic gravity-gradient noise in interferometric gravitational-wave detectors. Physical Review D*, **58**:122002, 1998.

[14] S. Rowan, J. Hough, and D. R. M. Crooks. *Thermal noise and material issues for gravitational wave detectors. Physics Letters A*, **347**:25–32, 2005.

[15] P. R. Saulson. *Fundamentals of Interferometric Gravitational Wave Detectors*. World Scientific, *Singapore*, 1994.

[16] S. Rowan and J. Hough. *Gravitational wave detection by interferometry. Living Reviews in Relativity*, **3**:1, 2000.

[17] B. Schutz. *Determining the Hubble constant from gravitaitonal wave observations. Nature*, **323**:310–311, 1986.

[18] C. D. Ott. *The gravitational-wave signature of core-collapse supernovae. Classical and Quantum Gravity*, **26**(6):063001, 2009.

[19] K. Thorne. *Gravitational Waves. World Scientific, Singapore*, 1995.

[20] B. Knispel and B. Allen. *Blandford's argument: The strongest continuous gravitational wave signal. Physical Review D*, **78**(4):044031, 2008.

[21] J. Weber. *Detection and generation of gravitational waves. Physical Review*, **117**:306–313, 1960.

[22] J. Weber. *Observation of the thermal fluctuations of a gravitational-wave detector. Physical Review Letters*, **17**:1228–1230, 1966.

[23] J. Weber. *Gravitational-wave-detector events. Physical Review Letters*, **20**:1307–1308, 1968.

[24] J. Weber. *Evidence for discovery of gravitational radiation. Physical Review Letters*, **22**:1320–1324, 1969.

[25] J. L. Levine and R. L. Garwin. *Absence of gravity-wave signals in a bar at 1695 Hz. Physical Review Letters*, **31**:173–176, 1973.

[26] J. A. Tyson. *Null search for bursts of gravitational radiation. Physical Review Letters*, **31**:326–329, 1973.

[27] R. W. P. Drever, J. Hough, R. Bland, and G. W. Lessnoff. *Search for short bursts of gravitational radiation. Nature*, **246**:340–344, 1973.

[28] V. B. Braginsky, A. B. Manukin, E. I. Popov, V. N. Rudenko, et al. *Upper limit of the density of extraterrestrial gravitational radiation. Soviet Physics, JETP*, **39**:387, 1974.

[29] M. E. Gertsenshtein and V. I. Pustovoit. *On the detection of low frequency gravitational waves. Soviet Physics, JETP*, **16**:433, 1962.

[30] R. Weiss. *Electromagnetically coupled broadband gravitational antenna. Quarterly Progress Report 105, Electronics research laboratory, MIT*, 1972.

[31] P. R. Saulson. *Thermal noise in mechanical experiments. Physical Review D*, **42**:2437, 1990.

[32] R. L. Forward. *Wideband laser-interferometer graviational-radiation experiment. Physical Review D*, **17**:379–390, 1978.

[33] W. Winkler, K. Danzmann, A. Rüdiger, and R. Schilling. *Heating by optical absorption and the performance of interferometric gravitational-wave detectors. Physical Review A*, **44**:7022–7036, 1991.

[34] H. Grote, A. Freise, M. Malec, G. Heinzel, et al. *Dual recycling for GEO 600. Classical and Quantum Gravity*, **21**:S473–S480, 2004.

[35] R. Drever. *A Gravity-Wave Detector Using Optical Cavity Sensing. Proceedings of the 9th International Conference on General Relativity and Gravitation, Cambridge University Press*, page 265, 1983.

[36] P. Aufmuth and K. Danzmann. Gravitational wave detectors. *New Journal of Physics*, **7**(1):202, 2005.

[37] J. Hough, S. Rowan, and B. S. Sathyaprakash. The search for gravitational waves. *Journal of Physics B: Atomic, Molecular and Optical Physics*, **38**(9):S497, 2005.

[38] B. J. Meers. *Recycling in laser-interferometric gravitational-wave detectors. Physical Review D*, **38**:2317–2326, 1988.

[39] K. A. Strain and B. J. Meers. *Experimental demonstration of dual re-cycling for interferometric gravitational-wave detectors. Physical Review Letters*, **66**:1391–1394, 1991.

[40] J. Hough, H. Walther, B.F. Schutz, J. Ehlers, H. Welling, I.F. Corbett, and V. Kose. *Proposal for a Joint German-British Interferometric Grav-itational Wave Detector. Max-Planck-Institut fur Quantenoptik Report*, **147**, 1989.

[41] J. Harms, Y. Chen, S. Chelkowski, A. Franzen, et al. *Squeezed-input, optical-spring, signal-recycled gravitational-wave detectors. Phys. Rev. D*, **68**(4):042001, 2003.

[42] C. M. Caves. *Quantum-mechanical noise in an interferometer. Physical Review D*, **23**:1693–1708, 1981.

[43] W. G. Unruh. *Proceedings of the NATO Advanced Study Institute on Quantum Optics and Experimental General Relativity*. **B94**:647, 1983.

[44] A. Buonanno and Y. Chen. *Quantum noise in second generation, signal-recycled laser interferometric gravitational-wave detectors. Physical Re-view D*, **64**:042006, 2001.

[45] S. Braccini, C. Bradaschia, R. Del Fabbro, A. Di Virgilio, et al. *Seismic vibrations mechanical filters for the gravitational waves detector VIRGO. Review of Scientific Instruments*, **67**:2899–2902, 1996.

[46] M. V. Plissi, C. I. Torrie, M. E. Husman, N. A. Robertson, et al. *GEO 600 triple pendulum suspension system: Seismic isolation and control. Review of Scientific Instruments*, **71**:2539–2545, 2000.

[47] G. Losurdo, M. Bernardini, S. Braccini, C. Bradaschia, et al. An inverted pendulum preisolator stage for the virgo suspension system. *Review of Scientific Instruments*, **70**(5):2507–2515, 1999.

[48] N. A. Robertson, G. Cagnoli, D. R. M. Crooks, E. Elliffe, et al. *Quadruple suspension design for Advanced LIGO*. *Classical and Quantum Gravity*, **19**(15):4043, 2002.

[49] P. R. Saulson. *Terrestrial gravitational noise on a gravitational wave antenna*. *Physical Review D*, **30**:732–736, 1984.

[50] M. Punturo, M. Abernathy, F. Acernese, B. Allen, et al. *The third generation of gravitational wave observatories and their science reach*. *Classical and Quantum Gravity*, **27**(8):084007, 2010.

[51] K. Kuroda and the LCGT Collaboration. Status of LCGT. *Classical and Quantum Gravity*, **27**(8):084004, 2010.

[52] G. M. Harry, D. R. M. Crooks, G. Cagnoli, M. M. Fejer, et al. *Thermal noise from optical coatings in gravitational wave detectors*. *Applied Optics*, **45**:1569, 2006.

[53] M. Evans, S. Ballmer, M. Fejer, P. Fritschel, G. Harry, and G. Ogin. *Thermo-optic noise in coated mirrors for high-precision optical measurements*. *Physical Review D*, **78**(10):102003, 2008.

[54] K. Kawabe and the LIGO Collaboration. Status of LIGO. *Journal of Physics Conference Series*, **120**(3):032003, 2008.

[55] P. Amico, L. Bosi, L. Carbone, L. Gammaitoni, et al. *Fused silica suspension for the VIRGO optics: status and perspectives*. *Classical and Quantum Gravity*, **19**:1669–1674, 2002.

[56] Gravitational Wave Interferometer Noise Calculator, Caltech. http://lhocds.ligo-wa.caltech.edu:8000/advligo/GWINC.

[57] S. M. Tywford. *Developements towards low loss suspensions for laser*

interferometric gravitational wave detectors. PhD thesis, University of Glasgow, 1998.

[58] LIGO image courtesy of Advanced LIGO website. http://www.advancedligo.mit.edu/.

[59] VIRGO image courtesy of INFN. http://www.virgo.infn.it/.

[60] GEO600 image courtesy of GEO600 website. http://www.geo600.uni-hannover.de/.

[61] LIGO Sensitivity Curves. http://www.ligo.caltech.edu/.

[62] GEO600 Sensitivity Curves. http://www.geo600.uni-hannover.de/geocurves/.

[63] GEO Sensitivity Curves. https://wwwcascina.virgo.infn.it/senscurve/.

[64] D. E. McClelland, S. M. Scott, M. B. Gray, D. A. Shaddock, et al. *Second-generation laser interferometry for gravitational wave detection: ACIGA progress. Classical and Quantum Gravity,* **18**(19):4121, 2001.

[65] Advanced LIGO team. *Advanced LIGO reference design.* LIGO document LIGO M060056-08-M, 2007.

[66] P. Fritschel. *Second generation instruments for the Laser Interferometer Gravitational Wave Observatory (LIGO). Proceedings of SPIE,* SPIE-4856:282–291, 2003.

[67] The Virgo Collaboration. Advanced virgo basline design. *Virgo Technical Document System,* VIR027A09, 2009.

[68] J. Abadie, The LIGO Scientific Collaboration, and the Virgo Collaboration. *Predictions for the rates of compact binary coalescences observable by ground-based gravitational-wave detectors. Classical and Quantum Gravity,* **27**(17):173001, 2010.

[69] *Einstein Gravitational Wave Telescope, proposal to the European Commission, Framework Programme 7* (2007). http://www.ego-gw.it/ILIAS-GW/FP7-DS/fp7-DS.htm.

[70] K. Danzmann and A. Rudiger. *LISA technology - concept, status, prospects. Classical and Quantum Gravity*, **20**:S1–S9, 2003.

[71] S. Kawamura, M. Ando, T. Nakamura, K. Tsubono, et al. *The Japanese space gravitational wave antenna - DECIGO. Journal of Physics: Conference Series*, **122**(1):012006, 2008.

[72] H. Kudoh, A. Taruya, T. Hiramatsu, and Y. Himemoto. *Detecting a gravitational-wave background with next-generation space interferometers. Phys. Rev. D*, **73**(6):064006, 2006.

[73] C. Ungarelli and A. Vecchio. *Studying the anisotropy of the gravitational wave stochastic background with LISA. Phys. Rev. D*, **64**:121501, 2001.

[74] LISA image courtesy of JPL. http://lisa.jpl.nasa.gov/gallery/.

[75] G.M. Harry, A.M. Gretarsson, P.R. Saulson, S.E. Kittelberger, et al. *Thermal noise in interferometric gravitational wave detectors due to dielectric optical coatings. Classical and Quantum Gravity*, **19**:897–917, 2002.

[76] C. Chaneliere, J.L. Autran, R.A.B. Devine, and B. Balland. *Tantalum pentoxide (Ta_2O_5) thin films for advanced dielectric applications. Materials Science and Engineering: R: Reports*, **22**(6):269 – 322, 1998.

[77] S. D. Penn, P. H. Sneddon, H. Armandula, J. C. Betzwieser, et al. *Mechanical loss in tantala/silica dielectric mirror coatings. Classical and Quantum Gravity*, **20**:2917–2928, 2003.

[78] Herbert B. Callen and Theodore A. Welton. *Irreversibility and Generalized Noise. Physical Review*, **83**(1):34–40, 1951.

[79] Herbert B. Callen and Richard F. Greene. *On a theorem of irreversible thermodynamics. Physical Review*, **86**:702–710, 1952.

[80] Y. Levin. *Internal thermal noise in the LIGO test masses: A direct approach. Physical Review D*, **57**:659, 1998.

[81] F. Bondu, P. Hello, and Y.-Y. Vinet. *Mirror thermal noise in interferometric gravitational wave detectors. Physics Letters A*, **246**:227–236, 1998.

[82] Y. T. Liu and K. S. Thorne. *Thermoelastic noise and homogeneous thermal noise in finite sized gravitational-wave test masses. Physical Review D*, **62**:122002, 2000.

[83] N. Nakagawa, A. M. Gretarsson, E. K. Gustafson, and M. M. Fejer. *Thermal noise in half-infinite mirrors with nonuniform loss: A slab of excess loss in a half-infinite mirror. Physical Review D*, **65**:102001, 2002.

[84] V. B. Braginsky and S. P. Vyatchanin. *Thermodynamical fluctuations in optical mirror coatings. Physics Letters A*, **312**:244–255, 2003.

[85] M.M. Fejer, S. Rowan, G. Cagnoli, D.R.M. Crooks, et al. *Thermoelastic dissipation in inhomogeneous media: Loss measurements and displacement noise in coated test masses for interferometric gravitational wave detectors. Physical Review D*, **70**:082003, 2004.

[86] H. J. Pain. *The Physics of Vibrationas and Waves.* Wiley, 6th edition, 2006.

[87] D. R. M. Crooks, P. Sneddon, G. Cagnoli, J. Hough, et al. *Excess mechanical loss associated with dielectric mirror coatings on test masses*

in interferometric gravitational wave detectors. Classical and Quantum Gravity, **19**:883–896, 2002.

[88] D. R. M. Crooks. *Mechanical loss and its signficance in the test mass mirrors of gravitational wave detectors.* PhD thesis, University of Glasgow, 2003.

[89] ANSYS Academic Research, Release 12.0, ANSYS, Inc. http://www.ansys.com/.

[90] S. Reid. *Studies of materials for future ground-based and space-based interferometric gravitational wave detectors.* PhD thesis, University of Glasgow, 2006.

[91] D.R.M. Crooks, G. Cagnoli, M.M. Fejer, A. Gretarsson, et al. *Experimental measurements of coating mechanical loss factors. Classical and Quantum Gravity*, **21**:1059–1065, 2004.

[92] S. Reid, G. Cagnoli, D. R. M. Crooks, J. Hough, et al. *Mechanical dissipation in silicon flexures. Physics Letters A*, **351**:205, 2006.

[93] N. W. McLachlan. *Theory of Vibrations.* Dover, 1952.

[94] L. De Broglie. *Sur la fréquence propre de l' électron. Comptes Rendus de l'Académie des Sciences*, 180:498–500, 1925.

[95] C. Davisson and L. H. Germer. *Diffraction of Electrons by a Crystal of Nickel. Phys. Rev.*, **30**(6):705–740, 1927.

[96] G.P. Thomson and A. Reid. *Diffraction of Cathode Rays by a Thin Film. Nature*, **119**:890, 1927.

[97] M. Knoll and E. Ruska. *Beitrag zur geometrischen Elektronenoptik. I. Annalen der Physik*, **404**:607, 1932.

[98] D. B. Williams and C. B. Carter. *Tranmission Electron Microscopy, A Textbook for Materials Science.* Springer US, 2nd edition, 2009.

[99] P. A. Doyle and P. S. Turner. *Relativistic Hartree–Fock X-ray and electron scattering factors.* Acta Crystallographica Section A, **24**(3):390–397, 1968.

[100] J. H. Konnert and J. Karle. *The computation of radial distribution functions for glassy materials.* Acta Crystallographica Section A, **29**(6):702–710, 1973.

[101] L. M. Peng, G. Ren, S. L. Dudarev, and M. J. Whelan. *Robust Parameterization of Elastic and Absorptive Electron Atomic Scattering Factors.* Acta Crystallographica Section A, **52**(2):257–276, 1996.

[102] E. J. Kirkland. *Advanced Computing in Electron Microscopy.* Springer US, 1st edition, 1998.

[103] C. Kittel. *Introduction to Solid State Physics.* John Wiley and Sons, 8th edition, 1995.

[104] M. Loretto. *Electron Beam Analysis of Materials.* Springer US, 2nd edition, 1998.

[105] Olympus Soft Imaging Solutions (SIS) GmbH, Johann-Krane-Weg 3948149 Münster, Germany. http://www.olympus-sis.com/.

[106] Gatan Inc., 5794 W. Las Positas Blvd. Pleasanton, CA 94588. http://www.gatan.com/.

[107] J. Ayache, L. Beaunier, J. Boumendil, G. Ehret, and D. Laub. *Sample Preparation Handbook for Transmission Electron Microscopy.* Springer Verlag, 2010.

[108] C. C. Ahn. *Transmission Electron Energy Loss Spectrometry in Materials Science and the EELS Atlas.* Wiley-VCH, 2nd edition, 2004.

[109] M. J. Olszta. *Stoichiometry and valence measurements of niobium oxides using electron energy-loss spectroscopy.* Journal of Microscopy, **224**:1365–2818, 2006.

[110] F. Hofer and P. Warbichler. *Application of EELS to the microanalysis of materials.* Microchimica Acta, **91**:125–134, 1987.

[111] Roditi Interntional, London SW8 4UF. http://www.roditi.com/.

[112] D. J. H. Cockayne. *The Study of Nanovolumes of Amrohpous Materials Using Electron Scattering.* Annu. Rev. Mater. Res., **37**:159–187, 2007.

[113] B.E. Warren. *X-ray Diffraction.* Dover Publications, 1990.

[114] D. A. Keen. *A comparison of various commonly used correlation functions for describing total scattering.* Journal of Applied Crystallography, **34**(2):172–177, 2001.

[115] Y. Chen. *Electron Diffraction Analysis of Amorphous $Ge_2Sb_2Te_5$.* PhD thesis, University of Oxford, 2010.

[116] F. H. Allen. *The Cambridge Structural Database: a quarter of a million crystal structures and rising.* Acta Crystallographica Section B, **58**:380–388, 2002.

[117] K. B. Borisenko, Y Chen, S. A. Song, D Nguyen-Manh, and David J. H. Cockayne. *A concerted rational crystallization/amorphization mechanism of $Ge_2Sb_2Te_5$.* Journal of Non-Crystalline Solids, **355**(43–44):2122–2126, 2009.

[118] K. B. Borisenko, Y. Chen, S. A. Song, and D. J. H. Cockayne. *Nanoscale Phase Separation and Building Blocks of $Ge_2Sb_2Te_5N$ and $Ge_2Sb_2Te_5N_2$ Thin Films*. Chemistry of Materials, **21**(21):5244–5251, 2009.

[119] S. J. Clark, M. D. Segall, C. J. Pickard, P. J. Hasnip, et al. First principles methods using CASTEP. *Zeitschrift für Kristallographie*, **220**(5-6):567–570, 2005.

[120] J. P. Perdew, K. Burke, and M. Ernzerhof. *Generalized Gradient Approximation Made Simple*. Physical Review Letters, **77**(18):3865–3868, 1996.

[121] G. J. Martyna, M. L. Klein, and M. Tuckerman. *Nosé−Hoover chains: The canonical ensemble via continuous dynamics*. Journal of Chemical Physics, **97**(4):2635–2643, 1992.

[122] O. L. Anderson and H. E. Bommel. *Ultrasonic absorption in fused silica at low temperatures and high frequencies*. Journal of the American Ceramic Society, **38**:125–131, 1955.

[123] V. B. Braginsky, V. P. Mitrofanov, and V. I. Panov. *Systems with small dissipation*. University of Chicago Press, Chicago, 1985.

[124] D. H. McGuigan, C. C. Lam, R. Q. Gram, A. W. Hoffman, et al. *Measurements of the mechanical Q of single-crystal silicon at low temperatures*. Journal of Low Temperature Physics, **30**:621–629, 1978.

[125] I. W. Martin, E. Chalkley, R. Nawrodt, H. Armandula, R. Bassiri, et al. *Comparison of the temperature dependence of the mechanical dissipation in thin films of Ta_2O_5 and Ta_2O_5 doped with TiO_2*. Classical and Quantum Gravity, **26**(15):155012, 2009.

[126] I. W. Martin, R. Bassiri, R. Nawrodt, M. M. Fejer, et al. *Effect of heat treatment on mechanical dissipation in Ta_2O_5 coatings. Classical and Quantum Gravity*, **27**(22).

[127] The Commonwealth Scienctific and Instrustrial Research Organisation (CSIRO), Materials Science and Engineering Division, Bradfield Road, West Lindfield, Sydney, NSW, 2070, Australia. http://www.csiro.au/.

[128] L. A. Aleshina and S. V. Loginova. *Rietveld analysis of X-ray diffraction pattern from β-Ta_2O_5 oxide. Crystallography Reports*, **47**(3):415–419, 2002.

[129] B. Cordero, V. Gomez, A. E. Platero-Prats, M. Reves, et al. *Covalent radii revisited. Dalton Transactions*, **21**:2832–2838, 2008.

[130] D. Cremer and D. Christen. *On the r_0 and r_e Structures of H_2O_2. Journal of Molecular Spectroscopy*, **74**:1002–1008, 1979.

[131] R. Bassiri, K. B. Borisenko, D. J. H. Cockayne, J. Hough, I. MacLaren, and S. Rowan. *Probing the atomic structure of amorphous Ta_2O_5 coatings. Applied Physics Letters*, **98**(3):031904, 2011.

[132] A.S. Nowick and B.S. Berry. *Anelastic Relaxation in Crystalline Solids.* Academic Press, New York, 1972.

[133] Advanced Thin Film, Inc. (ATF), 12110E Slauson Avenue, Unit 12 Santa Fe Springs, CA 90670. http://www.atfilminc.com/.

[134] S. Arrhenius. *On the reaction velocity of the inversion of cane sugar by acids. Zeitschrift für physikalische Chemie*, **4**:226, 1889.

[135] Laboratoire des Matériaux Avancés, LMA, CNRS-IN2P3, France. http://lma.in2p3.fr.

[136] MLD Technologies, 2672 Bayshore Parkwaysuite 701, Mountain View, CA 94043. http://www.mldtech.com/.

[137] Y. S. Touloukian and E. H. Buyco. *Thermo-physical Properties of Matter.* Plenum, New York, 1970.

[138] G. M. Harry, M. R. Abernathy, A. E. Becerra-Toledo, H. Armandula, et al. *Titania-doped tantala/silica coatings for gravitational-wave detection. Classical and Quantum Gravity*, **24**:405–415, 2007.

[139] K. Evans. Private communication. 2010.

[140] N. Morgado, R. Flamino, J. Franc, C. Michel, et al. *Study of coating mechanical losses for gravitational wave detectors.* LIGO DCC: G0900651, 2009.

[141] R Z Zhang, C L Wang, J C Li, J L Zhang, K Yang, and C Zhang. *Applied Physics Letters*, **91**:092909, 2007.

[142] H. Kawaguchi and T. Matsuo. *Complexes of tantalum with triaryloxides: Ligand and solvent effects on formation of hydride derivatives. Journal Organometallic Chemistry*, **690**(23):5333–5345, 2005.

[143] B. Castellano, E. Solari, C. Floriani, N. Re, et al. *Tantalum-Carbon Functionalities Bonded to a Calix[4]arene-Oxo Matrix The Chemistry of Mono-, Dialkyl, and Butadiene Derivatives of Tantalum (V). Chemistry - A European Journal*, **5**(2):722–737, 1999.

[144] R. K. Iler. *The Chemistry of Silica.* John Wiley and Sons, 1979.

[145] S. V. Ushakov, A. Navrotsky, Y. Yang, S. Stemmer, et al. *Crystallization in hafnia and zirconia-based systems. Physica Atatus Solidi (B)*, **241**(10):2268–2278, 2004.

[146] J.R. Martinez, S. Palomares-Sánchez, G. Ortega-Zarzosa, Facundo Ruiz, and Yurii Chumakov. *Rietveld refinement of amorphous SiO$_2$ prepared via sol-gel method*. *Materials Letters*, **60**(29-30):3526 – 3529, 2006.

[147] M. Abernathy et al. *Cryogenic Mechanical Loss Measurements of Heat-treated Hafnium Dioxide.* In preparation.

[148] J. Tang, M. Kai, Y. Kobayashi, S. Endo, O. Shimomura, et al. *A high-pressure high-temperature X-ray study of phase relations and polymorphism of HfO$_2$*. *Geophysical Monograph*, **101**:401–407, 1998.

[149] R. Ruh and P. W. R. Corfield. Crystal structure of monoclinic hafnia and comparison with monoclinic zirconia. *Journal of the American Ceramic Society*, **53**(3):126–129, 1970.

[150] I. W. Martin. *Studies of materials for use in interferometric gravitational wave detectors.* PhD thesis, University of Glasgow, 2009.

[151] T. Proffen, K. L. Page, S. E. McLain, B. Clausen, and *et.al.* *Atomic pair distribution function analysis of materials containing crystalline and amorphous phases*. *Zeitschrift für Kristallographie*, **220**(12):1002–1008, 2005.

[152] High-End Computing Terascale Resource HECToR, The University of Edinburgh, Edinburgh, EH9 3JZ. http://www.hector.ac.uk/.

[153] D. A. Andrews, S Roden, and T. A. King. *A model for lock-in growth in ring laser gyroscopes*. *IEEE Journal of Quantum Electronics*, **31**(9):1709–1715, 1995.

[154] K. Numata, A. Kemery, and J. Camp. *Thermal-noise limit in the frequency stabilization of lasers with rigid cavities*. *Physical Review Letters*, **93**:250602, 2004.

[155] R. J. Rafac, B. C. Young, J. A. Beall, W. M. Itano, et al. *Sub-dekahertz ultraviolet spectroscopy of* $^{199}Hg^+$. *Physical Review Letters*, **85**:2462–2465, 2000.

[156] H. Shinriki, T. Kisu, S.-I. Kimura, Y. Nishioka, et al. *Promising Storage Capacitor Structures with Thin* Ta_2O_5 *Film for Low-Power High−Density DRAMs. IEEE Transactions on Electron Devices*, **37**(9):1939 –1947, 1990.

[157] Y. L. Zhou, M. Niinomi, T. Akahori, H. Fukui, and H. Toda. *Corrosion resistance and biocompatibility of Ti-Ta alloys for biomedical applications. Materials Science and Engineering A*, **398**(1-2):28–36, 2005.

[158] Metler Toledo Ltd, 64 Boston Road, Beaumont Leys Leicester, LE4 1AW. http://www.mt.com/.

[159] SENTECH Instruments GmbH, Schwarzschildstraße 2, 12489 Berlin, Germany. http://www.sentech.de/.

[160] P. Murray. *Measurement of the mechanical loss of test mass materials for advanced gravitational wave detectors.* PhD thesis, University of Glasgow, 2008.

[161] R. Thielsch, A. Gatto, and N. Kaiser. *Mechanical Stress and Thermal-Elastic Properties of Oxide Coatings for Use in the Deep-Ultraviolet Spectral Region. Appl. Opt.*, **41**(16):3211–3217, 2002.

[162] E. Chalkley. *Investigations of the Properties of Materials for the Optics and Suspensions of Future Gravitational Wave Detectors.* PhD thesis, University of Glasgow, 2010.

[163] Hafnium Dioxide, WebElements. http://www.webelements.com/.